Measurement of the Inclusive B-Lifetime Using J/ψ's at the CDF– Experiment

Der Mathematisch–Naturwissenschaftlichen Fakultät
– Fachbereich 1 –
der Rheinisch–Westfälischen Technischen Hochschule Aachen
vorgelegte Dissertation zur Erlangung des akademischen Grades
eines Doktors der Naturwissenschaften

von
Diplom–Physiker

Hans–Joachim Wenzel

aus Oberhausen

Referent : Universitätsprofessor Dr. G. Flügge
Korreferent: Universitätsprofessor Dr. A. Böhm

Tag der mündlichen Prüfung: 4. November 1993

Abstract

This dissertation describes the measurement of the average B hadron lifetime using a high statistics sample of $B \to J/\psi X$ decays produced in $p\overline{p}$ collisions at a center of mass energy of $\sqrt{s} = 1.8$ TeV at the Fermilab Tevatron. The integrated luminosity of the sample is 10.1 pb^{-1} recorded with the Collider Detector at Fermilab (CDF). In this analysis the decay vertex of the decay $J/\psi \to \mu^+\mu^-$ as reconstructed by a silicon vertex detector is used to extract the lifetime from the data. This measurement is the average over all b-hadrons produced weighted by the product of their branching ratios into J/ψ and their production cross sections. We find the following value for the average b hadron lifetime:

$$\tau_B = 1.46 \pm 0.06\ (stat.)\ \pm 0.06\ (syst.)\ ps$$

This is the first measurement of the b-hadron lifetime at a hadron collider. It demonstrates that it is possible to access the large b-quark production cross section in $p\overline{p}$ collisions and to achieve high statistics even in modes which have small product branching ratios as in this case:
$BR(B \to J/\psi X) \cdot BR(J/\psi \to \mu^+\mu^-) = 7.7 \times 10^{-4}$.

Acknowledgments

First of all I want to say that I enjoyed the last three years very much and I would like to thank all my friends who made this years so unforgettable.

I never regretted my decision to join the CDF-group in Pisa. I am indebted to Prof. Giorgio Bellettini who invited me to be part of his group at the INFN Pisa.

Special thanks also to Franco Bedeschi who supervised me in the last three years. I have learned a lot from him.

I like to thank Prof. G. Flügge and Prof. A. Böhm for investing the time to review this thesis and for agreeing to act as Referent and Korreferent of this dissertation.

Without a working SVX-detector this thesis wouldn't have been possible. So I want to thank all members of the CDF-SVX group who worked very hard to make the SVX such a fine detector and to keep it alive in the unfriendly environment of a hadron collider. I think this thesis is a proof for the quality of the data taken by this device. The coming months will bring a lot of physics results which will benefit from the SVX detector.

I would like to thank Henry Frisch, Bob Kephart and Paul Tipton who were the "Godfathers" of the inclusive lifetime analysis.

Thanks to Marjorie Shapiro for her support, her suggestions helped me to find some 'bugs' in the early stage of this analysis. She also provided the study of "fake J/ψ's".

Thanks also to Dave Smith for reading the thesis, for the evenings sharing pasta and Chianti at his balcony in Marina di Pisa and for some sailing lessons.

Manfred Paulini found some 'typos' and helped to make this dissertation more readable.

Finally I am most grateful to my parents and brothers for their love and support. This thesis is dedicated to them.

Contents

1 Theoretical Introduction

This section gives a brief theoretical introduction emphasizing the topics relevant for the measurement described in this dissertation. The topic of this thesis is the determination of the average lifetime of b-hadrons produced in $p\bar{p}$-collisions at $\sqrt{s} = 1.8$ TeV using inclusive J/ψ. So the different sources of J/ψ produced in $p\bar{p}$-collisions will be listed, the b-cross section will be given as well as an estimate of the branching ratio for the decay $B \to \mathrm{J}/\psi\mathrm{X}$. Finally the b-lifetime formula will be derived which in section 8 will be used to give an estimate for the element $|V_{cb}|$ of the Cabibbo-Kobayashi-Maskawa matrix.

1.1 The Standard Model

The so-called Standard Model of particle interactions consists of two major parts: Quantum Chromo Dynamics (QCD) [1] based on the SU(3) group describing the strong interaction and the Glashow - Salam - Weinberg (GSW) model [2] for the electromagnetic and weak interactions. The latter is generally referred to as the Standard Model of electroweak interactions, and is based on the group SU(2) $\times$ U(1). In the electroweak model there are three types of elementary particles:

- Fundamental fermions: leptons and quarks are regarded as pointlike particles which couple to the gauge bosons of SU(2) through their weak charge and to the photon of U(1) through their electric charge.
- Four gauge bosons: Z^0, $W^{\pm}$, γ , corresponding to the mediators of the electroweak interaction. The massive Z^0 and $W^{\pm}$ are the mediators of the short range weak interaction. The massless photon or γ is the mediator of the long range electromagnetic interaction.
- The Higgs boson: The Higgs field is responsible for the masses of all the particles through the spontaneous symmetry breaking process.

The left-handed fermions are assumed to transform as doublets under the weak isospin group (weak isospin $I_3 = 1/2$), and the right-handed ones as singlets (weak isospin $I_3 = 0$). So far there is no evidence for the existence of right-handed neutrinos. There are three fermion generations now known

Generation:	1	2	3	I_3	Y	Q
Leptons	$\begin{pmatrix} \nu_e \\ e \end{pmatrix}_L$	$\begin{pmatrix} \nu_\mu \\ \mu \end{pmatrix}_L$	$\begin{pmatrix} \nu_\tau? \\ \tau \end{pmatrix}_L$	$1/2$ $-1/2$	-1 -1	0 -1
Quarks	$\begin{pmatrix} u \\ d \end{pmatrix}_L$	$\begin{pmatrix} c \\ s \end{pmatrix}_L$	$\begin{pmatrix} t? \\ b \end{pmatrix}_L$	$1/2$ $-1/2$	$1/3$ $1/3$	$2/3$ $-1/3$
Higgs	$\Phi? = \begin{pmatrix} \phi^+ \\ \phi^0 \end{pmatrix}$			$1/2$ $-1/2$	1 1	1 0

Table 1: *Particles and fields in the GSW model. The quantum numbers of the third component I_3 of weak isospin, weak-hypercharge Y and the charge Q are given. They are related by $Q = I_3 + \frac{1}{2}Y$.*

and the experiments at the LEP accelerator at CERN located in Geneva Switzerland have shown that the shape of the e^+e^--annihilation cross section around the invariant mass of the Z^0 is in good agreement with the prediction of the standard model for 3 species of light neutrinos [3]. Table 1 lists the properties of the fundamental particles. The scheme is not complete yet, the top quark, the τ-neutrino and the Higgs particle haven't been found yet and only indirect evidence exists for their existence. One of the most important goals of modern elementary particle physics is to fill the 'holes' in that scheme. The highest priority for the two experiments CDF and D0 at the TEVATRON (see below) is the discovery of the top quark.

The three massive vector bosons Z^0 and $W^\pm$ mediate the weak interaction. The nine massless vector bosons the photon and eight gluons are respectively responsible for the electromagnetic and strong interactions. Table 2 lists the properties of all gauge bosons.

	Spin	Charge	Color	Mass (GeV/c^2)
γ	1	0	no	0
Z^0	1	0	no	91.187 ± 0.007 [3]
$W^{\pm}$	1	± 1	no	80.22 ± 0.26 [3]
g_i $(i = 1, ..., 8)$	1	0	yes	0

Table 2: *Properties of the gauge bosons. The eight gluons correspond to the octet associated with the three colors of the QCD* SU(3) *group.*

1.2 Theory of the Electroweak Interaction

The interactions of the SU(2) $\times$ U(1) gauge field are specified by the electroweak theory with the coupling constants determined by the electric charge e, and the weak mixing angle $\sin^2\theta_W$ through the following relationships:

$$\begin{aligned} \textit{electromagnetic coupling}: \quad e &= \frac{g_1 g_2}{\sqrt{g_1^2 + g_2^2}} \\ \textit{weak coupling}: \quad g_Z &= \frac{e}{\sin\theta_W \cos\theta_W} \end{aligned} \tag{1}$$

where g_1 and g_2 are the coupling constants of the U(1) and SU(2) groups, respectively.

The fields resulting from the basic SU(2) and U(1) groups are propagated by the photon and the Z^0 and $W^{\pm}$ bosons. While the photon is massless, the masses of the Z^0 and $W^{\pm}$ bosons are related to the weak mixing angle θ_W in the following way:

$$\sin^2\theta_W = 1 - \frac{M_W^2}{M_Z^2}. \tag{2}$$

The electromagnetic interaction proceeds through a pure vector type coupling, while the $W^{\pm}$ leads to a charged weak coupling through the vector minus axial vector (V-A) factor. The Z^0 neutral current weak interaction contains V and A couplings. These couplings are summarized in the following figures:

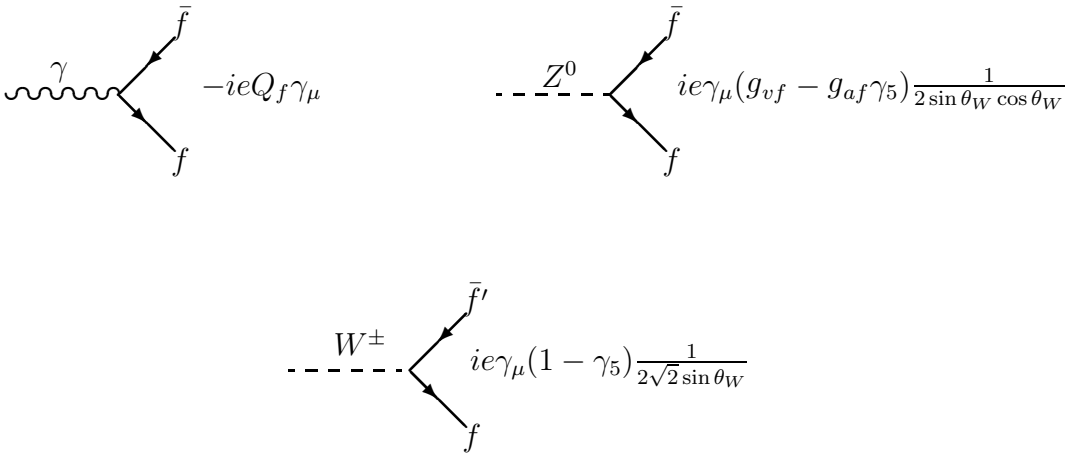

Figure 1: *Feynman diagrams for charged and neutral-current couplings.*

The parameters g_{vf} and g_{af} are the fermion vector and axial vector coupling constants.

$$g_{af} = I_{3f} \qquad\qquad g_{vf} = I_{3f} - 2Q_f \sin^2\theta_W \tag{3}$$

where f refers to the particular fermion, Q_f is the fermion charge, and I_{3f} is the third component of the weak isospin.

1.3 The CKM Matrix

In the Standard Model with $\mathrm{SU}(2)\times\mathrm{U}(1)$ as the gauge group, the left-handed quarks are arranged in doublets:

$$\begin{pmatrix} u \\ d' \end{pmatrix} \quad \begin{pmatrix} c \\ s' \end{pmatrix} \quad \begin{pmatrix} t \\ b' \end{pmatrix} \tag{4}$$

where the d', s', and b' quarks are the mass eigenstates that are not the same as the weak quark flavor eigenstates d, s, and b. The u, c and t quarks are by convention unmixed. The matrix which relates this two bases is the so-called Cabibbo-Kobayashi-Maskawa (CKM) matrix [4], which is the extension of the four-quark case where the mixing was expressed in form of a single angle the so called Cabibbo-angle [5].

$$\begin{pmatrix} d' \\ s' \\ b' \end{pmatrix} = \begin{pmatrix} V_{ud} & V_{us} & V_{ub} \\ V_{cd} & V_{cs} & V_{cb} \\ V_{td} & V_{ts} & V_{tb} \end{pmatrix} \begin{pmatrix} d \\ s \\ b \end{pmatrix} \tag{5}$$

Historically the Cabbibo theory was introduced at a time when only three quarks (u, d, s) were known. To explain the fact that strangeness changing weak transitions appeared to have only one fourth of the strength of $u \to d$ transitions Cabbibo proposed:

$$J_\mu^{Hadronic} = J_\mu^{(\Delta S=0)} \cos\theta_C + J_\mu^{(\Delta S=1)} \sin\theta_C \tag{6}$$

where θ_C is the Cabibbo angle. This way he could fit several rates for the beta decays of strange particles. Experimentally $\sin\theta_C$ was found to be $\approx 1/4$.

Each of the nine complex elements V_{ij} of the unitary CKM matrix represents the coupling of a charge 2/3 quark to a charge -1/3 quark. If there are more than three generations of quarks, the CKM model would have to be extended to a larger matrix. Studying B decay properties and $B^0\bar{B}^0$-mixing can give information on the CKM matrix elements which involve the b quark.

The Wolfenstein parameterization [6] emphasizes the relative size of the CKM matrix elements by expressing them in powers of the Cabibbo angle λ. In this parameterization the CKM matrix is approximated in terms of three real variables λ, A and ρ, and a phase η:

$$V \sim \begin{pmatrix} 1-\lambda^2/2 & \lambda & A\lambda^3(\rho - i\eta) \\ -\lambda & 1-\lambda^2/2 & A\lambda^2 \\ A\lambda^3(1-\rho-i\eta) & -A\lambda^2 & 1 \end{pmatrix} \tag{7}$$

where λ=0.22 [6], $A = 0.90 \pm 0.12$ [7], and the experimental limit on charmless semileptonic B-decay gives $\sqrt{\rho^2+\eta^2} = 0.39 \pm 0.07$ [7]. Note that this parameterization is only correct to order λ^3 in the matrix elements. A more detailed discussion about the properties of the CKM-matrix and how the magnitudes of its elements are determined experimentally can be found in references [8] or [3].

1.4 Inclusive J/ψ-Production at High Transverse Momentum at the TEVATRON

As pointed out in [10] the decay $J/\psi \to \mu^+\mu^-$ provides a clean b-enriched signal at a hadron collider. This sample is a good starting point to do b-spectroscopy, to search for new B-hadrons [11], and to study the properties of b-production and direct J/ψ and χ-production.

Since the topic of this dissertation is the measurement of the b-lifetime we want to keep this section short and emphasize only the facts which are relevant in the context of this analysis. This are:

1. the decay $J/\psi \to \mu^+\mu^-$ provides a simple trigger to obtain a clean b-enriched sample at a hadron collider.

2. the b-production cross section at the TEVATRON is large so that it is possible to obtain a high statistics sample of b's although the product branching ratio for the chosen decay mode is very small:
   $BR(B \to J/\psi X) \cdot BR(J/\psi \to \mu^+\mu^-) = 7.7 \times 10^{-4}$ [9].

3. Not all J/ψ's come from b-decays. The larger fraction comes from prompt sources. That means we have to distinguish this two components in order to be able to extract the b-lifetime from our sample. How this is done technically will be described in section 3

At the TEVATRON there are two possible sources of J/ψ production at large P_t (see e.g. [10]).

1. from direct charmonium production:
   $gg,\ q\overline{q} \to \chi\ g$ and $qg \to \chi g$ with $\chi \to \psi\gamma$

2. from production and decay of b-hadrons:
   $gg,\ q\overline{q} \to b\overline{b}$ with $b \to B \to \psi X$
   $gg,\ q\overline{q} \to b\overline{b}g$ and $qg \to b\overline{b}q$ with $b \to B \to \psi X$

Estimates of the differential cross section of all these different sources are calculated in [10]. The cross section for b-quark production in $p\bar{p}$-collisions at $\sqrt{s} = 1.8$ TeV is in the order of 10 μbarn when requiring the transverse momentum of the b-quark to be greater than 8 GeV/c and the rapidity to be $|Y| < 1.0$. Figure 2 shows the result of the various CDF b-quark cross section measurements using the data collected in the 1988/89 collider run ([9] [12], [13], [14] and [15]) and preliminary 1992/93 data. The data is compared to a next to leading order QCD calculation (see [16], [17]) using the recent MRSD0 parameterization of the parton distribution function [18]. The data lies above the theoretical predictions (solid line). It also looks like the measured shape of the differential cross section doesn't agree with the theoretical prediction. The data seems to fall steeper than the theoretical prediction. For a more detailed discussion of this discrepancies and attempts to bring theory and experiments in better agreement with each other see e.g. [19] and [20].

Note that the $\psi(2s)$ point in Figure 2 was obtained assuming that all $\psi(2s)$ come from b-decay. Now with the SVX-detector it is possible to distinguish between prompt $\psi(2s)$ and $\psi(2s)$ produced in b-decays. A preliminary analysis of the new data shows that the larger fraction is prompt in contradiction to the expectation. That means that the b-cross section obtained by using the $\psi(2s)$ will have to be corrected towards smaller values.

With the SVX it is also possible to estimate the exact fraction of J/ψ from b-decay in the sample. This allows to measure the total and differential b-cross section using inclusive J/ψ without depending on theoretical assumptions.

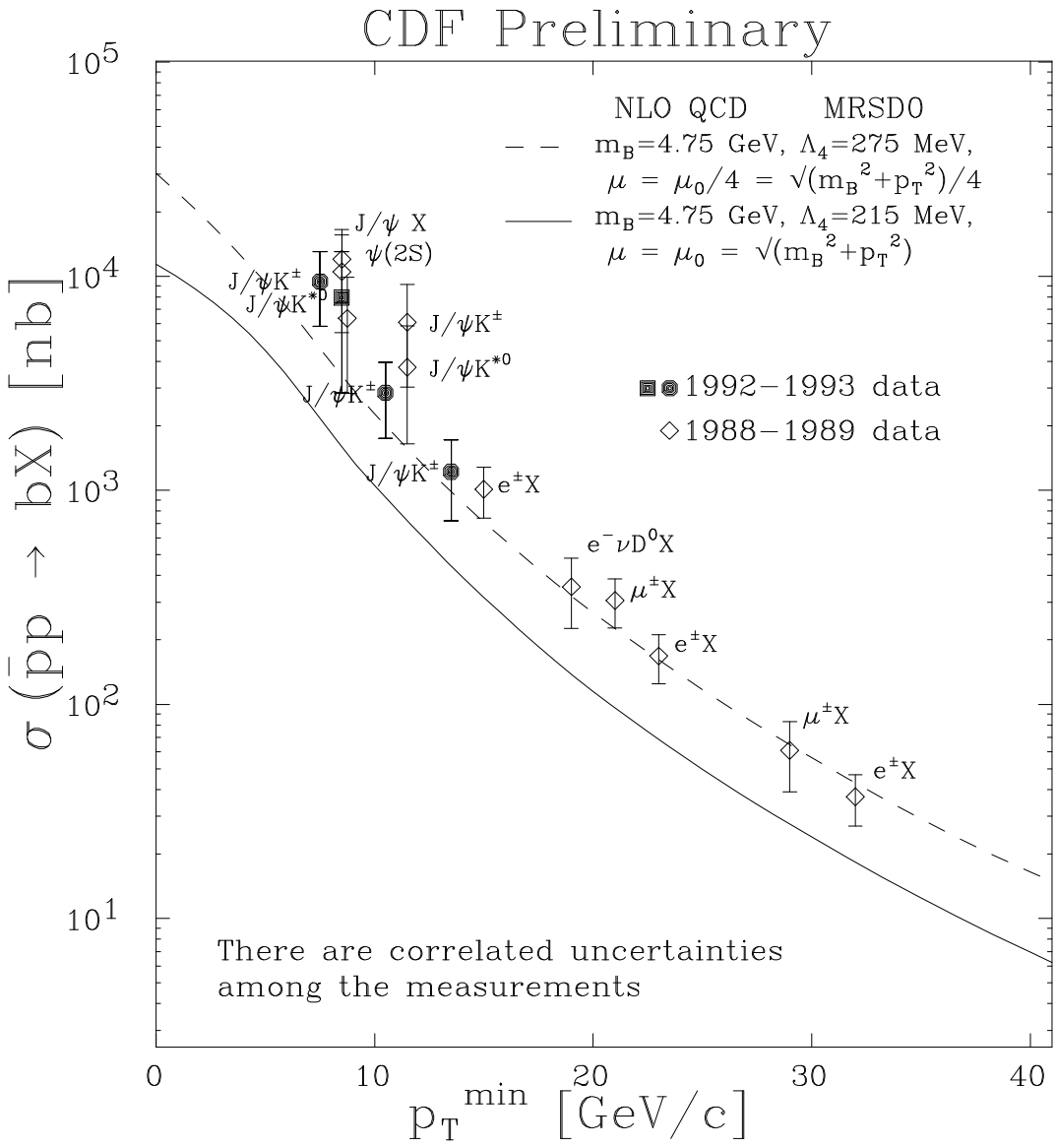

Figure 2: *Summary of CDF b-quark cross-section measurements.*

1.5 B-fragmentation

B-hadrons are produced during the fragmentation process of the b-quark. The lowest mass states include the $B^+(\bar{b}u)$, $B_d^0(\bar{b}d)$, $B_s^0(\bar{b}s)$, $\Lambda_b^0(udb)$...hadrons and their anti-particles. The probability to fragment into the various possible b-flavored mesons and baryons is expected to be:

$$B_u : B_d : B_s : B_{baryon} = 0.375 : 0.375 : 0.15 : 0.10$$

The fragmentation process is highly non pertubative and up to now is only described by phenomenological models. One of these models is the Peterson et al. model ([21], [22]) which describes the fragmentation of heavy quarks (b,c). The Peterson fragmentation function has the following form:

$$D_b(z) = \frac{N}{z[1 - (1/z) - \epsilon_b/(1-z)]^2} \tag{8}$$

where the definition of the scaling variable z is:

$$z = \frac{(E_H + P_H^{\parallel})}{(E_b + P_b)}$$

with:

E_H	:	energy of the b-hadron
$P_H^{\parallel}$	:	b-hadron momentum component parallel to the b-quark momentum
E_b, P_b	:	energy and momentum of b-quark

The fragmentation parameter ϵ_b was measured to have the following value [3]:

$$\epsilon_b = 0.006 \pm 0.002$$

Figure 3 shows the Peterson fragmentation function for $\epsilon_b = 0.006$. One observes that the hadrons produced in the fragmentation process carry most of the momentum of the b-quark.

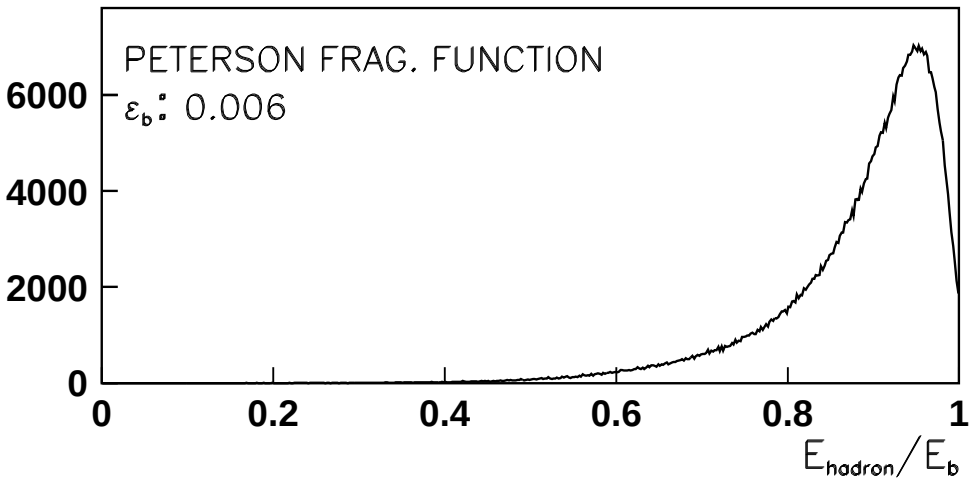

Figure 3: *Peterson Fragmentation function.*

1.6 The Decay $B \to \mathrm{J}/\psi\mathrm{X}$.

The decay $\mathrm{B}^{\pm} \to \mathrm{J}/\psi\,\mathrm{X}$ is expected to proceed dominantly through the 'color suppressed' spectator diagram shown in Figure 4. In this diagram color matching is required between the c quark from the $(b \to c)$ transition and the $\bar{c}$ from the $W \to \bar{c}s$ decay to form a color neutral J/ψ.

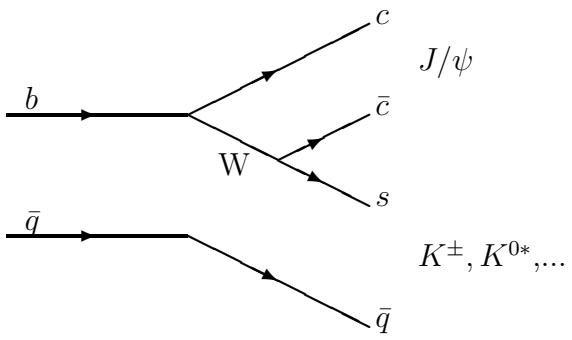

Figure 4: *Feynman diagram for the decay* $b \to \mathrm{J}/\psi$ X.

The branching ratio for the decay $b \to \mathrm{J}/\psi\mathrm{X}$ can be estimated in the following way: First the branching ratio $b \to ccs$ is assumed to be about 20 % (see e.g. [23], [24]). Secondly the $c\overline{c}$ pairs have to be in a color singlet state to form charmonium. This is the case for one out of three produced $c\overline{c}$ pairs which results in a suppression of charmonium production by a factor of 1/9. Thirdly one has to know the probability that a charmonium state is produced out of a $c\overline{c}$ singlet. This value is predicted to be about 60% [25]. Altogether this results in an estimate for the inclusive branching ratio of $\mathrm{BR}(b \to \mathrm{J}/\psi\ \mathrm{X}) \approx$ 1.3 % if the mechanism of color suppression is at work.

The presence of soft gluons in the weak decay which can transport color at no cost could overcome the color suppression [25] and in this case the branching ratio could be as large as 10 %. The presence of hard gluons on the other hand would lead the branching ratio to be much smaller than 1.3 %. Measurements of the branching ratio $\mathrm{BR}(b \to \mathrm{J}/\psi\ \mathrm{X})$ have been performed by the ARGUS, CLEO [26] and ALEPH [27] experiments with comparable

results. The world average [3] is $1.12 \pm 0.16\%$, which is very close to the theoretical estimate above including color suppression. In this dissertation the decay $B \to J/\psi\, X \to \mu^+\, \mu^-\, X$ which has a very small product branching ratio of $BR(B \to J/\psi X) \cdot BR(J/\psi \to \mu^+\mu^-) = 7.7 \times 10^{-4}$ [9] is used to measure the lifetime thus demonstrating that it is possible to explore the large cross section at a hadron collider.

1.7 Lifetime of b-Hadrons

In 1983 the MAC and MARKII collaborations at PEP measured the lifetime of b-hadrons produced in e^+e^- annihilations to be in the order of 1 ps [28]. Later on this result was confirmed by experiments at PETRA [29] and more recently at LEP [30]. This result was unexpected. If the strength of the mixing between the third and second generation were the same as for the mixing between the second and first, the b-lifetime would be about 0.1 ps. The long b-lifetime was the first hint that the third generation of quarks is much more decoupled from the second generation than the second from the first. In the following a formula for the b-lifetime is derived and it is shown how the lifetime is related to the elements V_{cb} and V_{ub} of the CKM matrix. This derivation can be found in [31].

In the Standard model the b-quark can decay into a u or a c quark coupling to a virtual W. The W then decays into a leptonic ($e\overline{\nu_e}, \mu\overline{\nu_\mu}, \tau\overline{\nu_\tau}$) or a quark doublet ($\overline{u}$d,$\overline{c}$s). In the spectator model the other quark(s) forming the hadron have no effect on the decay, they are just spectators. This leads to the expectation that all hadrons containing a b-quark have approximately the same lifetime. QCD radiation effects are believed to be only on the order of 10% (see below). It would be a big surprise if measurements showed that there is a difference of more than 10% for the different B-hadrons. This is also the justification for averaging the lifetime over an unknown mixture of different b-hadrons, like it is done in this measurement.

In the case of the charm mesons: $D^\pm$ and D^0 the lifetimes are $1.066 \pm 0.023\ ps$ and $0.420 \pm 0.008\ ps$ [3] respectively. But the beauty is heavier than charm quark (4.95 compared to 1.65 GeV/c^2) so that the spectator model should be a better description than in case of charm mesons. Measurements of the lifetime of charged and neutral B-mesons using reconstructed exclusive b-decays are now becoming available at LEP and the Tevatron (see e.g. [32] and [33]). Indirect measurements performed by ARGUS and CLEO relating

the lifetime ratio $\frac{\tau_{B^\pm}}{\tau_{B^0}}$ to the ratio of the semileptonic branching ratios of the $B^\pm$ and B^0 mesons, indicate that within the errors the ratio is 1. [34]. Figure 6 summarizes all available lifetime ratio measurements as of July 1993 (from [35]). Unfortunately the measurements are not yet sensitive enough to confirm or rule out differences at the 5 to 10% level.

The best way to derive a formula for the b-lifetime is to derive it explicitly for the semileptonic decay mode. The semileptonic decays have the smallest uncertainties in the extraction of standard model parameters (see e.g. [36]) and in addition the semileptonic branching ratios are well measured experimentally [3]. So using the semileptonic mode to derive the lifetime formula introduces the smallest uncertainties. Figure 5 shows the Feynman diagram for the semileptonic decay of the $\bar{B}^0$-meson.

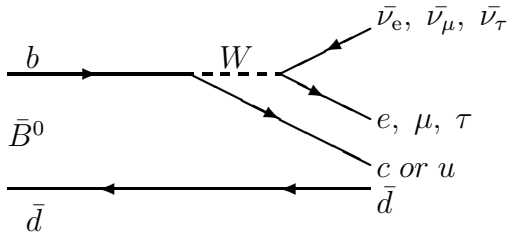

Figure 5: *Feynman diagram for the semileptonic $\bar{B}^0$-meson decay in the spectator model.*

The lifetime is simply the reciprocal of the total width and is related to the width of a specific channel in terms of its branching ratio:

$$\tau_b = \frac{1}{\Gamma_{TOT}(b)} = \frac{Br_{sl}}{\Gamma_{sl}} \tag{9}$$

The matrix element for a b quark decaying into a lighter quark and a virtual W followed by the decay of the W into a lepton and a neutrino is the product of a hadronic and a leptonic electroweak current:

$$M_{sl}(b \to q) = \frac{G_F}{\sqrt{2}} V_{qb} \left\{\overline{q}\gamma^\mu(1-\gamma_5)b\right\} \left\{\overline{l}\gamma^\mu(1-\gamma_5)\nu_l\right\} \tag{10}$$

where $G_F = 1.16639 \cdot 10^{-5} GeV^{-2}$ is the Fermi coupling constant which was obtained from the muon lifetime formula. V_{qb} is the element of the CKM matrix for the $b \to q$ transition.

By squaring $M_{sl}(b \to q)$ and integrating over phase space one obtains the decay rate (width):

$$\Gamma_{sl}(b \to q) = \frac{G_F^2 m_b^5}{192\pi^3} \cdot |V_{qb}|^2 \cdot F(\epsilon) \tag{11}$$

where m_b is the mass of the b-quark. $F(\epsilon)$ can be written as the product of two terms:

$$F(\epsilon) = \phi_{PS}(\epsilon) \times \phi_{QCD}(\epsilon) \tag{12}$$

ϕ_{QCD} is a QCD correction factor which is expected to be 1.0 if there are no gluons and non-spectator effects involved. ϕ_{PS} is the phase space factor which is calculated to be [39]:

$$\phi_{PS}(\epsilon) = 1 - 8\epsilon^2 + 8\epsilon^6 - \epsilon^8 - 24\epsilon^4 ln\epsilon \tag{13}$$

with $\epsilon = m_q/m_b$.
Within the standard model the b-quark can only decay into a u or c-quark. By measuring the lifetime τ_b one measures a combination of V_{ub} and V_{cb}. Within the spectator model we get the following expression for the b-lifetime:

$$\tau_b = \frac{Br_{sl}}{\Gamma_{sl}} = \frac{Br_{sl}}{\frac{G_F^2 m_b^5}{192\pi^3} \cdot [F(\epsilon_u)|V_{ub}|^2 + F(\epsilon_c)|V_{cb}|^2]} \tag{14}$$

Since $|V_{ub}|^2 << |V_{cb}|^2$, τ_b is mainly a measurement of $|V_{cb}|$. The fact that $|V_{ub}|^2 << |V_{cb}|^2$, was derived from a fit to the high P_t end of the lepton spectrum of B meson decays [37]. For the transition $b \to u$ one expects an enhancement at the high P_t end of the lepton spectrum since for this decay more phase space is available than for $b \to c$.

From formula (14) it is obvious that the extraction of the CKM matrix elements depends on how well the masses of the different quarks involved (ucb) are known. Measurements of the so called 'effective' quark mass have been preformed by ARGUS: $m_b = 4.95 \pm 0.07\ GeV/c^2$ and CLEO: $m_b = 4.95 \pm 0.04\ GeV/c^2$ [38]. Both experiments obtain the result by doing a fit to the prompt lepton spectrum from B-decay within the context of the ACM model [40]. For the QCD correction factor one can derive the following functional form [39]:

$$\phi_{QCD} = 1 - (\alpha_s/3\pi)g(\epsilon) \tag{15}$$

where $\alpha_s(m_b^2)$ is the strong coupling constant. For numerical purposes ϕ_{QCD} may be approximated to within 0.2% by the following expression [39]:

$$\phi_{QCD} = 1 - (\alpha_s/3\pi)\left[(\pi^2 - \frac{31}{4})(1-\epsilon)^2 + \frac{3}{2}\right] \tag{16}$$

With the choice of $m_b = 4.95\ GeV/c^2$, $m_c = 1.65\ GeV/c^2$, $m_u = 0.2\ GeV/c^2$ and $\alpha_s(m_b^2) = 0.20$, the QCD radiation correction reduces the $b \to c$ and $b \to u$ transitions by 10.4 and 14.6 % respectively. Finally we get the following numerical value for Γ_{sl}:

$$\Gamma_{sl} = 2.67 \cdot 10^{-11}\left[|V_{cb}|^2 + 2.15|V_{ub}|^2\right]\ (GeV) \tag{17}$$

In section 8 we will use formula (14) to get an estimate for $|V_{cb}|$.

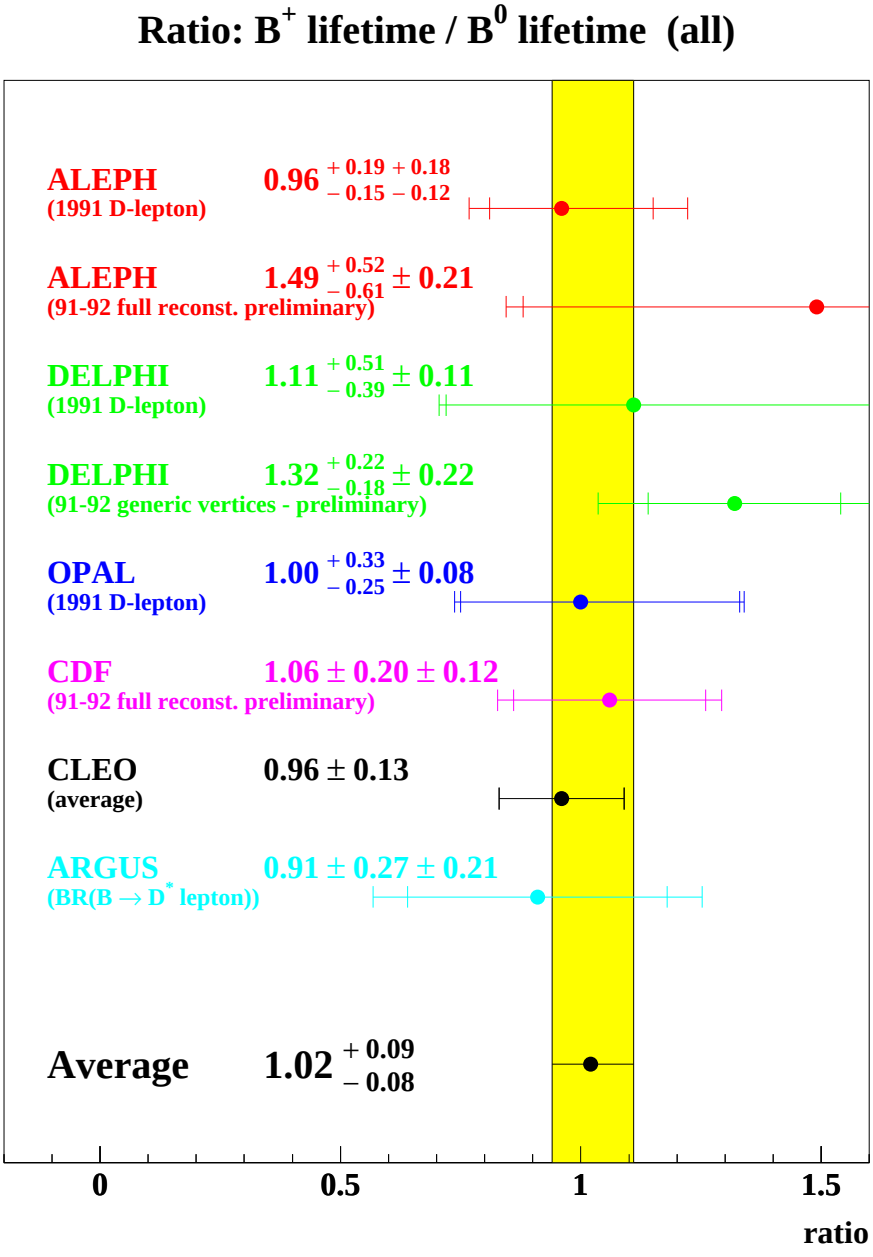

Figure 6: *Summary of B^+/B^0 lifetime ratio measurements.*

2 The Experimental Apparatus

2.1 The Tevatron

The Fermilab Tevatron located in Batavia, Illinois, is currently the accelerator providing the highest particle energy in the world. The Tevatron is a $\overline{p}p$ 'collider' where counter-rotating beams of protons and antiprotons are brought to collision with a center of mass energy of $\sqrt{s} = 1.8$ TeV.

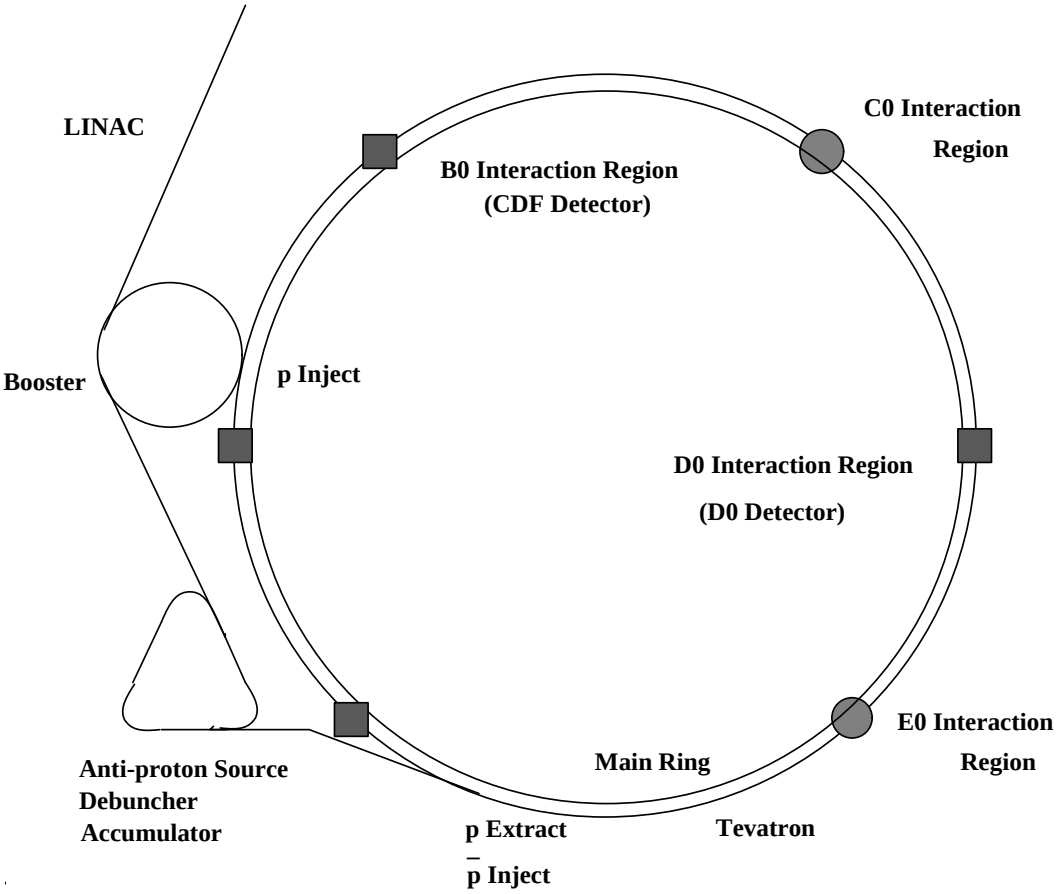

Figure 7: *Layout of the Fermilab Tevatron.*

Figure 7 shows the layout of the Tevatron. The steps necessary to achieve colliding beams of protons and antiprotons are described in the following. At the beginning hydrogen gas is extracted from a gas bottle. The hydrogen is

then ionized to form H^-. The ions are then accelerated in two steps: first up to 750 KeV by a Cockcroft-Walton accelerator and then a linear accelerator (LINAC) brings them to a final energy of 200 MeV. After that the ions are focused on a thin carbon foil to strip off the two electrons. The bare protons are then transferred to a circular accelerator called the booster which brings them to an energy of 8 GeV. The protons are then grouped together into bunches which are fed into the main ring. The main ring shares the tunnel with the Tevatron and has the same circumference of 6300 m, but keeps the particles in orbit with conventional magnets, while at the Tevatron superconducting magnets provide more bending power and so allow higher energies. The main ring accelerates the proton bunches to 150 GeV before they are transferred into the Tevatron, where they are accelerated jointly with the antiprotons to 900 GeV. For the 1992-93 collider run the Tevatron has been operated in a 6 bunch mode which means 6 bunches of protons were kept in the Tevatron at the same time, each bunch containing approximately 12×10^{10} protons.

The first steps to obtain antiprotons are the same as for protons only that for antiproton production the protons are only accelerated to 120 GeV in the Main Ring before they are extracted and focussed onto a copper target. Here they react where one of the reaction products are antiprotons which are collected and then sent to the so-called debuncher were they are 'cooled'. That means the momentum spread of the antiprotons is reduced. The antiprotons are then stored or 'stacked' in the accumulator. When the stack reaches approximately 60×10^{10} $\overline{p}$'s, 6 bunches of approximately 4×10^{10} $\overline{p}$'s each are transferred to the Main Ring, and then to the Tevatron where they move in the same ring as the protons but in opposite directions. Protons and antiprotons are then brought to collision at two interaction regions called B0 and D0, where CDF and the D0-detector are located.

The most important parameter of an accelerator, besides the center of mass energy that it can reach, is the Luminosity $\mathcal{L}$. The Luminosity is defined by the relation

$$N = \mathcal{L}\sigma$$

where N is the observed interaction rate for a given process (in sec^{-1}) and σ is the corresponding cross section (in cm^2). At the Tevatron the luminosity is determined by the following parameters:

$$\mathcal{L} = \frac{N_p N_{\bar{p}} B f_0}{4\pi\sigma_b^2}$$

where N_p and $N_{\bar{p}}$ are the number of protons and antiprotons per bunch, B is the number of bunches, f_0 ($\approx 50\ kHz$) is the revolution frequency, and σ_b is the cross sectional area of the bunches.

For 6 bunch operation, the time between collisions is $\sim 3.5\mu sec$. During the 1992-93 run, which lasted from the 12th of May 1992 to the first of June 1993, the average luminosity was approximately $3 \times 10^{30}\text{cm}^{-2}\text{sec}^{-1}$. The highest instantaneous luminosity achieved was about $9 \times 10^{30}\text{cm}^{-2}\text{sec}^{-1}$. The total luminosity delivered by the accelerator during that period was estimated to be 30.2 pb^{-1}. CDF managed to record 21.4 pb^{-1} on tape corresponding to 15.5 million events. This means the detector efficiency was approximately 71%.

2.2 The CDF Detector

The Collider Detector at Fermilab (CDF) is a multi-purpose detector to measure the energy, the momentum and the type of particles produced at the Tevatron collider. A description of all detector components as of 1989 can be found in reference [41].

For the analysis described in this thesis only data recorded with the central part of the CDF detector have been used. The detector components most important for this analysis are the Central Tracking Chamber (CTC), the Central MUon chambers (CMU) and in particular the Silicon VerteX detector (SVX) which was installed for the 1992-93 run. These crucial detector components will be described in more detail in the following subsections. Here just a short overview about the central detector components of CDF is presented.

Figure 8 shows the cross section of the CDF detector. The detector component closest to the interaction point is the silicon vertex detector which will be described later. The SVX is embedded in the VTX which is a vertex time projection chamber. The VTX has good reconstruction capabilities in the r-z plane and is used to reconstruct the z-position of the interaction vertex (or the vertices in case of multiple interactions) with an accuracy of approximately 1 mm.

The VTX is surrounded by the Central Tracking Chamber (CTC) which is a large cylindrical drift chamber with an inner radius of 0.3 m, an outer radius of 1.3 m, and a length of 3.2 m. The CTC will be described in more detail later.

Outside the CTC a superconducting solenoidal coil of 5 m length is located at a radius of approximately 1.5 m. The coil produces a magnetic field of about 1.4 Tesla which allows the measurement of the transverse momenta of charged tracks in the CTC.

The central calorimeter is located outside the coil. The calorimeter doesn't play an important role in this analysis but muons have to penetrate it (4.9 absorption lengths) undergoing multiple scattering. The calorimeter is divided into forward and backward parts (called the two 'arches'), each divided in 24 wedges each covering 15^0 in ϕ. Every wedge is composed of 10 projective towers pointing to the nominal interaction point. The segmentation in ϕ and η is $\Delta\eta \times \Delta\phi = 0.09 \times 15^\circ$. Where η is the so called pseudo rapidity which is defined as $\eta = -ln\ tan\theta/2$. θ is the polar angle with the

z-axis defined by the beam. Each tower consists of an inner electromagnetic part (CEM) and a hadronic part (CHA) at larger radius. The calorimeter is a sampling calorimeter where several layers of passive material (lead for the CEM, steel for the CHA) are interspersed with plastic scintillators to measure the shower energy. The energy resolution is $\sigma(E)/E = 0.13/\sqrt{E}$ for the electromagnetic and $\sigma(E)/E = 0.70/\sqrt{E}$ for the hadronic calorimeter.

The Central MUon chambers (CMU) are placed at the outer radius of the hadronic calorimeter and will be described in more detail later. For the 92-93 run 2 major upgrades have extended the muon detection capability of CDF. First there are the Central Muon eXtension chambers (CMX) which increase the acceptance of the central muon trigger from $|\eta| < 0.65$ to $|\eta| < 1$. Muons reconstructed in the CMX haven't been used in this analysis since it is a new device and is not as well understood as the CMU chambers. The second upgrade to the central muon system are the CMP-chambers which cover roughly the same range in detector rapidity as the CMU chambers but they are positioned at larger radius behind additional steel shielding which doubles the number of interaction lengths and so decreases the probability of hadron punchthrough.

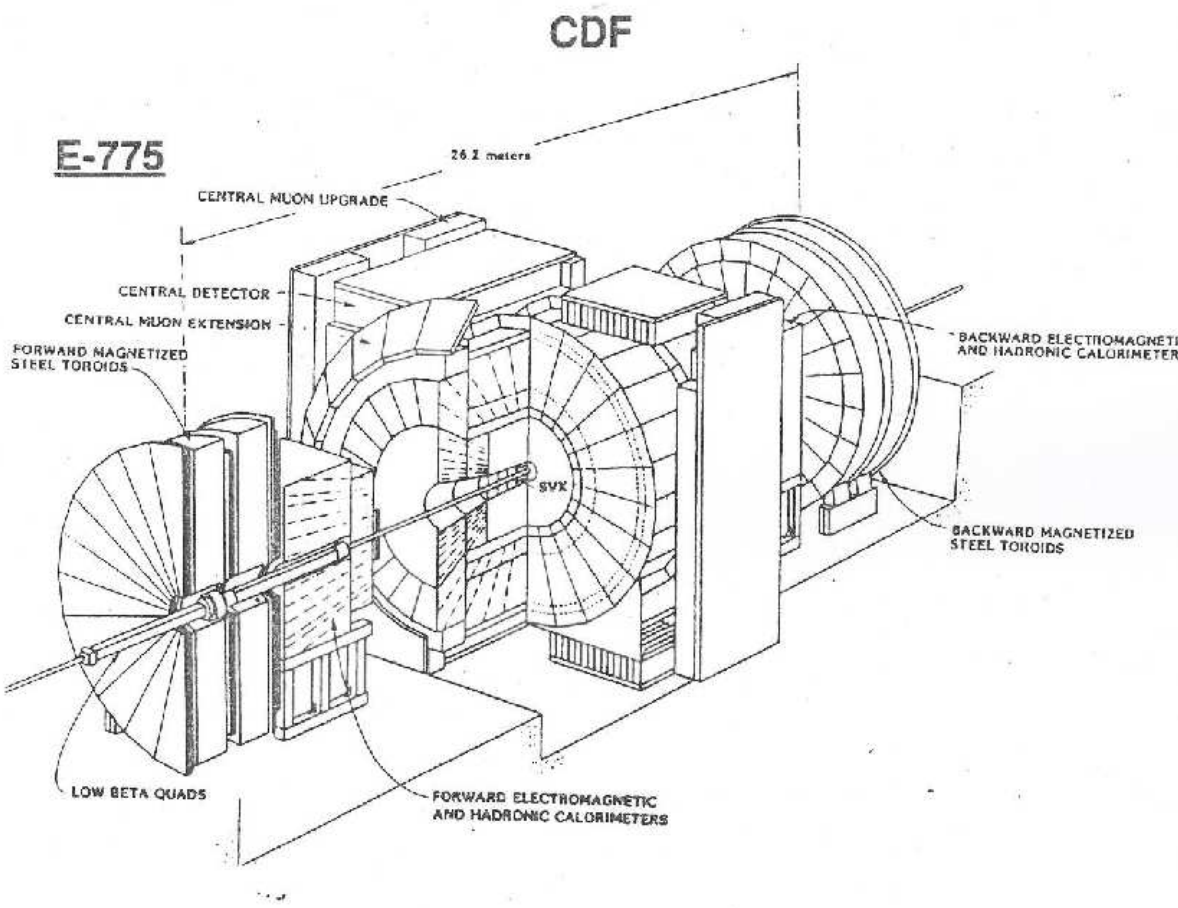

Figure 8: *Cross section of the CDF detector.*

2.3 The Central Tracking Chamber (CTC)

The central tracking chamber is a large cylindrical wire drift chamber. It covers the rapidity region $|\eta| < 1.2$ [42]. The 84 layers of sense wires are arranged into 9 superlayers. 5 of the layers containing 12 layers of sense wires parallel to the beam provide only R-ϕ information. Between the five axial layers we find four stereo layers which consist of 6 sense wire layers each. The angle of the stereo wires with respect to the beamline alternates between $+3^0$ and -3^0. The stereo layers add z information to the tracks.

Within the superlayers, the wires are grouped into cells to reduce the maximum drift time ($v_{drift} \approx 50\mu m/nsec$) to less than 800 nsec. Within each cell the wires lie in a plane rotated 45^0 from the radial direction to compensate for the Lorentz angle. This arrangement also has the advantage that each radial high momentum track ($P_t > 2.5\ GeV/c$) passes very close to at least one wire in each superlayer and so produces a prompt hit. This is used by the Central Fast Tracker (CFT) which reconstructs high momentum tracks at trigger level (see below). The design resolution on each wire is 200 μm resulting in a momentum resolution of $\frac{\sigma_{P_t}}{P_t} \approx 0.002 \times P_t$.

Figure 9 shows an event display showing the hits in the CTC with the tracks reconstructed offline superimposed. The left insert is a magnification which very nicely shows the cell geometry. The crosses indicate the position of the sense wires. Table 3 summarizes some of the mechanical and electrostatic parameters of the CTC.

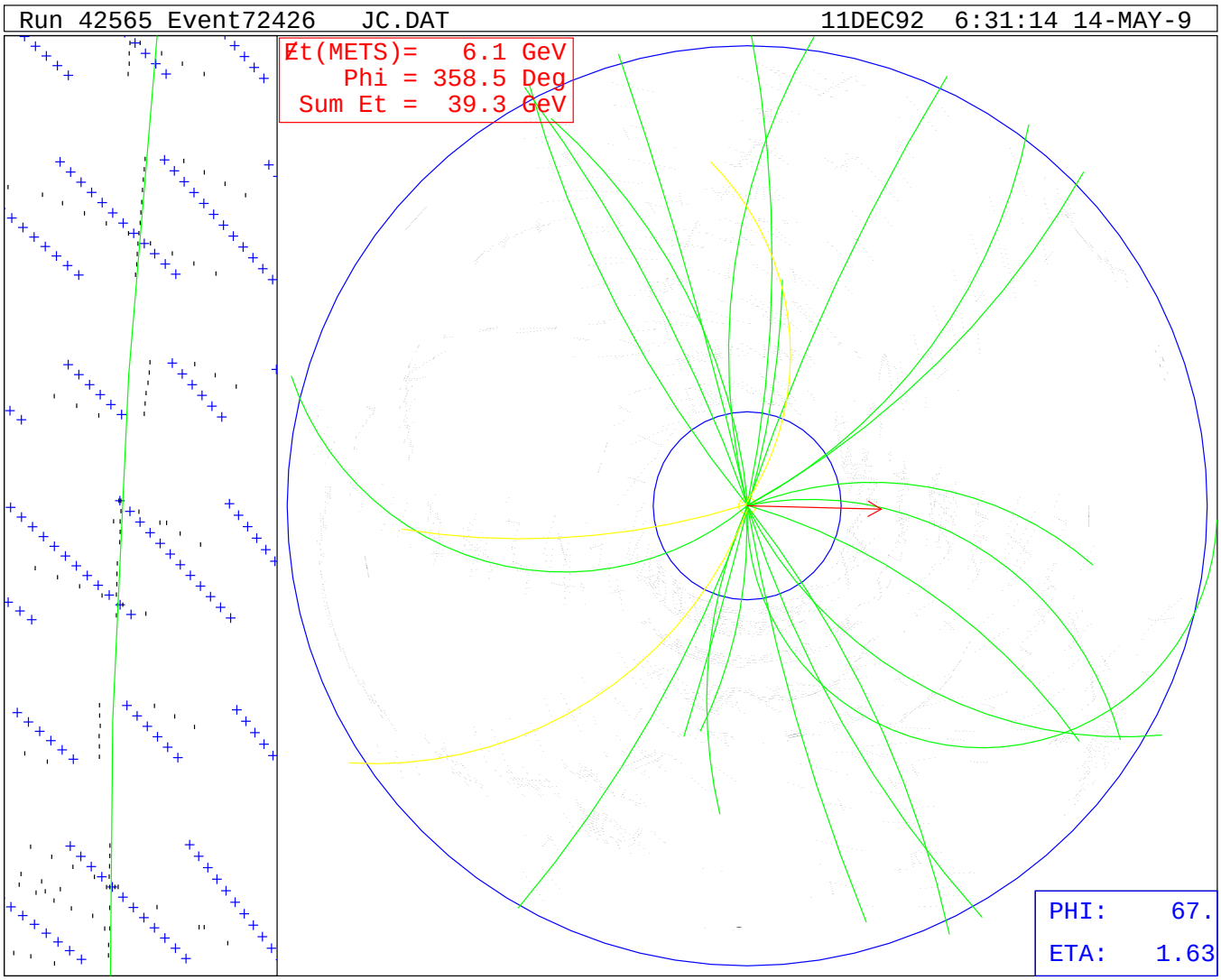

Figure 9: *An event display showing the r-ϕ projection of the CTC wire hits with reconstructed tracks superimposed. At left is a close up which shows the cell geometry of the outer superlayers 4 to 8. The crosses indicate the position of the sense wires.*

Mechanical parameters	
Number of layers	84
Number of superlayers	9
Stereo angle	0^0 $+3^0$ 0^0 -3^0 0^0 $+3^0$ 0^0 $+3^0$ 0^0
Number of super cells/layer	30, 42, 48, 60, 72, 84, 96, 108, 120
Number of sense wires/cell	12, 6, 12, 6, 12, 6, 12, 6, 12
Sense wire spacing	10 mm in plane of wires
Tilt angle	45^0
Radius of innermost sense wire	309 mm
Radius of outermost sense wire	1320 mm
Wire length	3214 mm
Sense wire diameter/tension	40 μm gold plated tungsten/135g
Gas	argon-ethane-alcohol (49.6%:49.6%:0.8%)
Drift field E_0	1350 V/cm
Drift field uniformity	dE_0/E_0 1.5%(rms)

Table 3: *Mechanical and electrostatic parameters of the Central Tracking Chamber.*

2.4 The Central Fast Tracker (CFT)

A detailed description of the hardware and performance of the CFT can be found in [43]. The CFT is a hardware track-finder for the Central Tracking Chamber. The CFT allows the measurement of high momentum ($P_t > 2.5\ GeV/c$) tracks in the CTC and provides this information within 2.5 μs at Level 2 of the CDF trigger. The momentum resolution is $\frac{\sigma_{P_t}}{P_t^2} \approx 3\%$.

The CFT uses only the $R\phi$ information of the 5 axial CTC-superlayers. Since the sense wires lie in a plane rotated by 45^0 from the radial direction any high P_t track will cross very near to one wire in each superlayer and give a prompt hit which means a hit with a very short drift time. To detect the prompt hits the CFT opens a coincidence latch with a width of 80 nsec after the beam-crossing to the 'digital stream fast out data' of each of the 4392 axial sense wires, which are read out by LeCroy 1879 TDC's. This prompt hits are then used to find track candidates.

In addition, a delayed gate following 500 to 650 nsec after the beam crossing corresponding to 2/3 of the cell size is applied to record delayed hits at a larger drift distance. The width of the gate is chosen to ensure at least two delayed hits in each cell. The delayed hits are used in a second pass on the data to verify any high P_t track found by processing prompt hits. The efficiency of finding a track in the CFT rises from 50% at p_T =2.6 GeV/c to 94% for $p_T > 3.1$ GeV/c. The measured efficiency as a function of P_t is discussed in section 3.2.

2.5 The Central Muon System (CMU)

The central muon detector (CMU) consists of 48 modules placed at the outer radius of each hadron calorimeter wedge [44]. Each module covers approximately 12.6^0 in ϕ with a 1.2^0 gap on both sides of the wedge. The layout and dimensions of one module are shown in Figure 10.

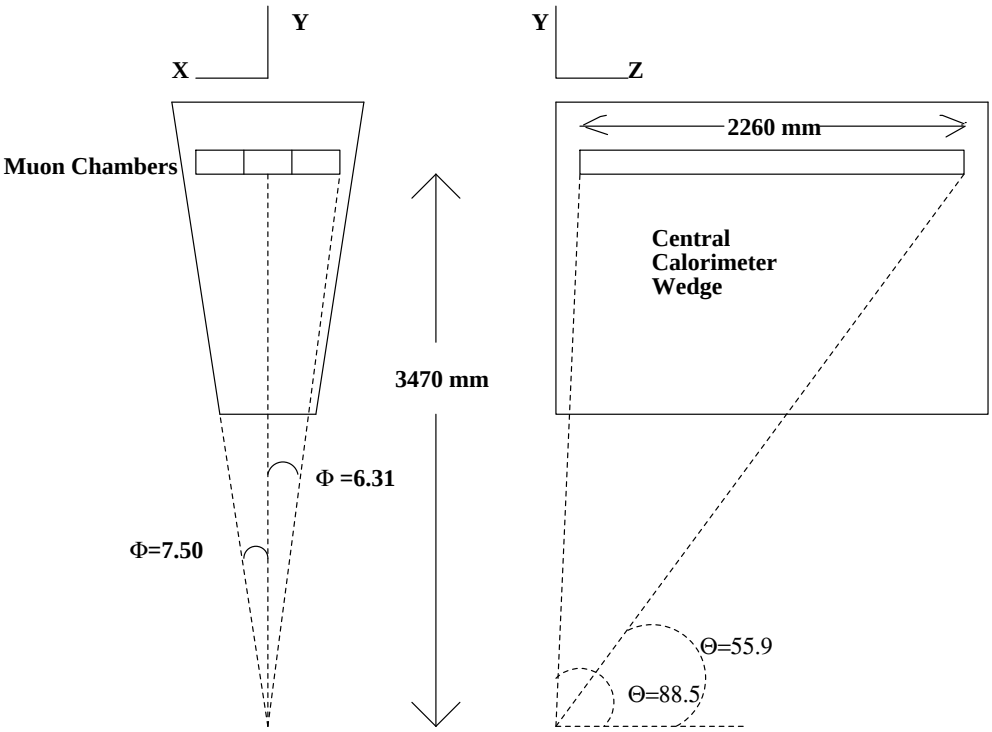

Figure 10: *Geometry of the central muon chambers (CMU).*

The muon chambers are proportional drift chambers which measure the tracks of charged particles penetrating the central calorimeters (4.9 absorption lengths).

Each module consist of 4 layers which are segmented in ϕ to form three towers of 4.2^0 each. Figure 11 shows the geometry of one of these towers consisting of 16 rectangular drift cells. Sense wires from alternating cells are connected at $\theta = 90^0$ so that there are 8 effective anode wires per muon tower. The sense wires are read out at both ends which allows to measure the z-position along the wires with a precision of 1.2 mm using the charge

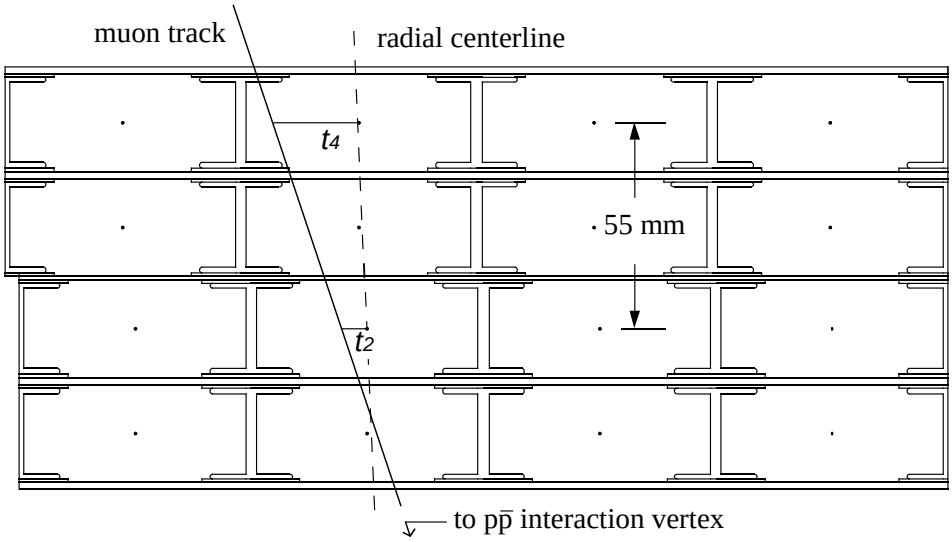

Figure 11: *Cross section of a single muon tower showing drift times t_i and the track angle.*

division method. This is also necessary to resolve the ambiguity which of the connected chambers has been hit by the particle. The chambers measure 4 points on a particle trajectory with a precision of 250 μm using the drift-time information.

In total the CMU system covers 84% of the angular region between $56^0 < \theta < 124^0$. (that means in pseudorapidity $|\eta| < 0.65$). The loss of 16% in acceptance is due to the 2.4^0 gap between each wedge and to the gap between the two calorimeter arches at $\theta = 90^0$.

The efficiency to detect a muon within the CMU acceptance has a plateau of approximately 93 % for muons with a transverse momentum of more than 3 GeV/c (see also section 3.2).

2.6 The Central Dimuon Trigger

At the TEVATRON the interaction rate is ≈ 130 kHz at an average luminosity $\mathcal{L}$ of $3 \times 10^{30} \mathrm{cm}^{-2}\mathrm{sec}^{-1}$, while events can be written to tape only at a rate of a few Hz. Therefore the trigger has to reject a large fraction of events and to select only events of particular interest. At CDF this is accomplished by a

three level trigger system which is described in [45]. The first two levels are hardware triggers while level 3 is a software trigger consisting of FORTRAN reconstruction and filtering code.

The trigger selecting the events in this analysis was labeled: TWO_CMU_ONE_CFT. It required that two short muon track segments (so called 'stubs') are found by the level 1 electronics as described in [46]. At level 2 one of the two muon stubs has to match to a track in the CTC as found by the CFT. Figure 12 shows how the angle α as measured in the muon chambers is related to the transverse momentum of the track. The relation between the deflection angle β and the transverse momentum is:

$$sin\frac{\beta}{2} = \frac{eLB}{2P_t} \tag{18}$$

where e is the charge of the track, L = 1.44 m is the radius of the solenoidal magnetic field, and B is the value of the magnetic field. The relation between the angle β and the angle α is:

$$Dsin\alpha = Lsin\frac{\beta}{2} \tag{19}$$

where D = 3.470 m is the radius of the muon chambers. In the small angle approximation for α, one finds:

$$\alpha \approx \frac{e\ L^2\ B}{2\ D\ P_t}. \tag{20}$$

This approximate definition of α was used by the level 2 hardware to check a match between tracks found in the CFT and muon stubs. Note that multiple scattering leads to a gaussian smearing of α. So the measurement of the slope α in the muon chambers can only approximately measure the actual P_t of the muon.

Level 3 required the muon candidates to be oppositely charged and the invariant mass of the dimuon system to be between 2.8 and 3.4 GeV/c^2. More about the trigger can be found in sections 3.2 and 6.3.

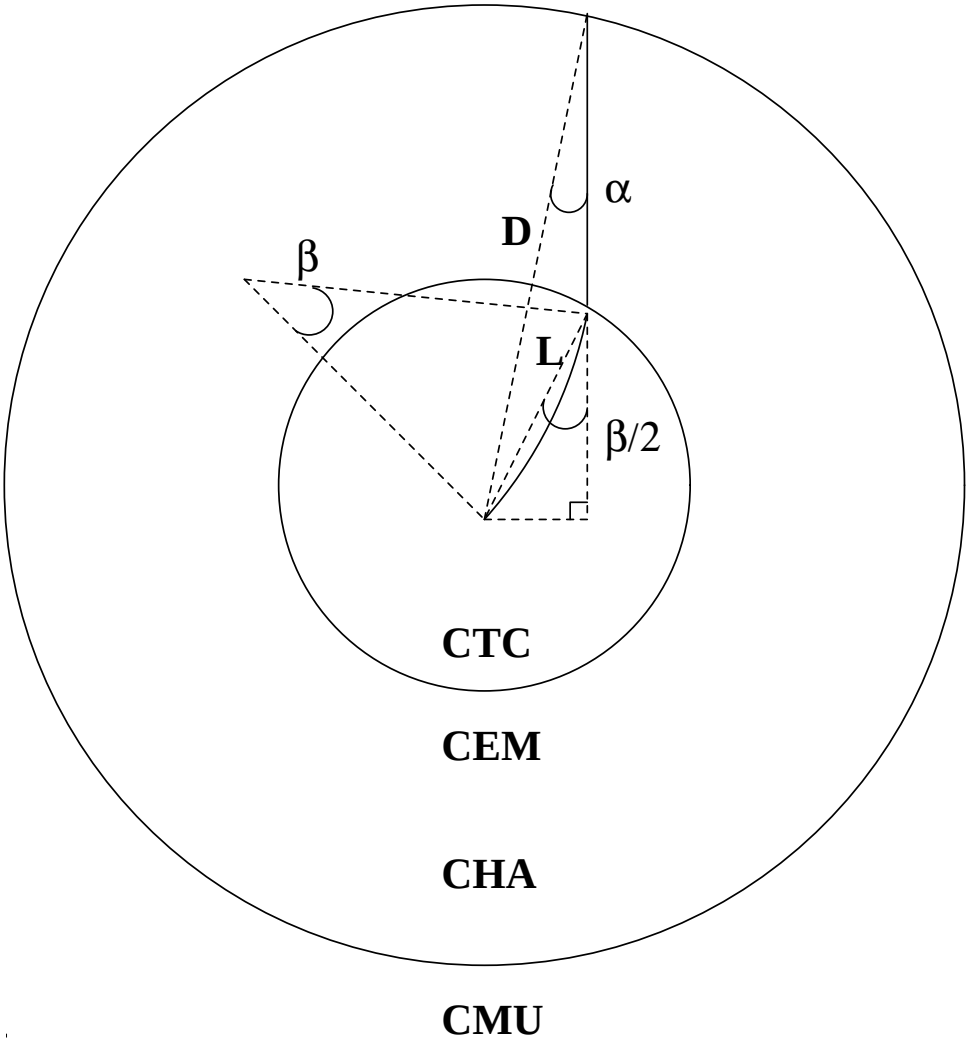

Figure 12: *Relation between the angle α as measured in the CMU and the deflection angle β as measured in the CTC.*

2.7 The Silicon VerteX Detector (SVX)

The SVX is an upgrade of the original CDF tracking system and was installed for the 1992-93 run [47]. At the Tevatron Collider, the $\bar{p}p$ interaction vertex is distributed along the beamline as a gaussian with a σ of approximately 30 cm. Consequently a long vertex detector is required to have good acceptance. The SVX is 51 cm long and consists of two independent cylindrical modules (barrels), left and right (forward/backward) of the nominal beam-beam interaction point. One of the two barrels is shown in Figure 13. The acceptance is ≈ 60 % of the $\bar{p}p$ collision vertices.

The amount of material in the SVX has been minimized, because the creation of secondary particles and conversion pairs in the SVX is a source of background for all CDF detector components and triggers. In addition multiple scattering is the limiting factor in measuring the impact parameter of low momentum tracks. For the same reason the beampipe is made of beryllium to reduce the amount of multiple scattering before the first measuring plane of the SVX.

The SVX consists of 4 radial layers of silicon strip detectors with the strips parallel to the beam. Thus providing only Rϕ information. The pitch between readout strips is 60 μm for the first three layers (numbered 0 to 2) and 55 μm for the fourth one (numbered 3) resulting in a spatial resolution of approximately 13 μm in each layer. The 13 μm are obtained because charge information is also available. Calculating the center of gravity of charge clusters of hits affecting more than one strip improves the resolution. For a 1 strip cluster and a pitch of 60 μm one expects a resolution of $60/\sqrt{12} = 17.3$ μm. The inner and outer layers are at radii of approximately 3 and 8 cm. The detectors are arranged in a 12-sided geometry. A 30^0 section in ϕ is called a 'wedge'. To obtain a length of 25.5 cm along the beam direction, three silicon detectors of 8.5 cm each were electrically bonded together. These bonds are made with $25\mu m$ aluminum wires which are ultrasonically fused to pads on the detector surface. These are read out electronically at the two outside ends. The source capacitance of each 25.5 cm long strip is about 30 pF. Table 4 summarizes some dimensions of the SVX detector.

A group of three connected detectors is called a 'ladder', and is the basic subdivision of the device. One ladder for the third layer is shown in Figure 14. The ladders are fabricated of Rohacell, a light weight foam reinforced with carbon fiber strips. Each ladder is individually assembled before

being mounted. There are four sizes of ladders corresponding to the four radial layers. Ladders are supported at the ends by beryllium bulkheads. The total number of ladders is 12 sides x 4 layers x 2 modules = 96, with 24 of each of the four radial types. In its position on the face of the barrels, each ladder is tilted by 3 degrees about its length to allow some overlap between adjacent faces. However, on the innermost layer no such overlap exists.

At the outside end of each ladder sits a small circuit board. This circuit is the readout hybrid for the ladder. It contains the readout chips for that ladder as well as auxiliary components and bus connections needed for the operation of the chips.

Layer	Face	Radius [cm]	Tot. Width [cm]	Act. Width [cm]	Pitch [μm]	Nr. of Strips	Nr. of Chips
0	IN	2.9899	1.6040	1.536	60	256	2
1	OUT	4.2710	2.3720	2.304	60	384	3
2	OUT	5.7022	3.1400	3.072	60	512	4
3	IN	7.8508	4.2925	4.224	55	768	6

Table 4: *Positions and dimensions of silicon detectors*

The total number of readout channels is 46080. The SVX readout chip has digital and analog parts. The analog part has 128 channels of charge integrating amplifiers followed by sample and hold and threshold storage stages. The digital part contains logic for sparsification and serial readout. The SVX chip has the ability to sparsify and read out only channels above the threshold. Sparsification is needed to reduce the readout time and the amount of data to be read out to an acceptable level. An average occupancy of 10% corresponds to a scan time of 0.77 msec compared to an allowed budget of
2 msec. Part of the front end electronics are the so called port cards which are mounted to the bulkheads. The port cards use an analog differential driver circuit to drive the pulse height information from the microstrips via a serial analog bus to the digitizers which are located in a fast bus crate outside the CDF detector.

To remove excess heat from the electronic the SVX is equipped with a cooling system which keeps the temperature at 20^0 C. This is achieved by pumping chilled water through cooling pipes which are in thermal contact

with the beryllium bulkheads at the readout end.

Figure 15 shows an event display of the SVX detector and Figure 16 shows the magnification of the reconstructed tracks. The drawn circle in Figure 16 corresponds to a distance of 0.5 cm from the primary interaction vertex. Each of the straight lines represents a track. The length of the lines is proportional to the transverse momentum of the track. This event is very interesting since we can clearly distinguish two displaced secondary vertices. One of them which is closer to the primary vertex at a distance of approximately 750 μm is a candidate for the exclusive b-decay:

$$\mathrm{B}^0 \to \mathrm{J}/\psi\,\mathrm{K}^{*0} \to \mu^+\mu^-\mathrm{K}^+\pi^-.$$

The SVX-detector has already demonstrated its power to reduce combinatorial background when doing b-spectroscopy. Requiring the vertex to be displaced improves the signal-to-background ratio significantly [11]. The second displaced vertex in the event is very likely due to the decay of the second b in the event.

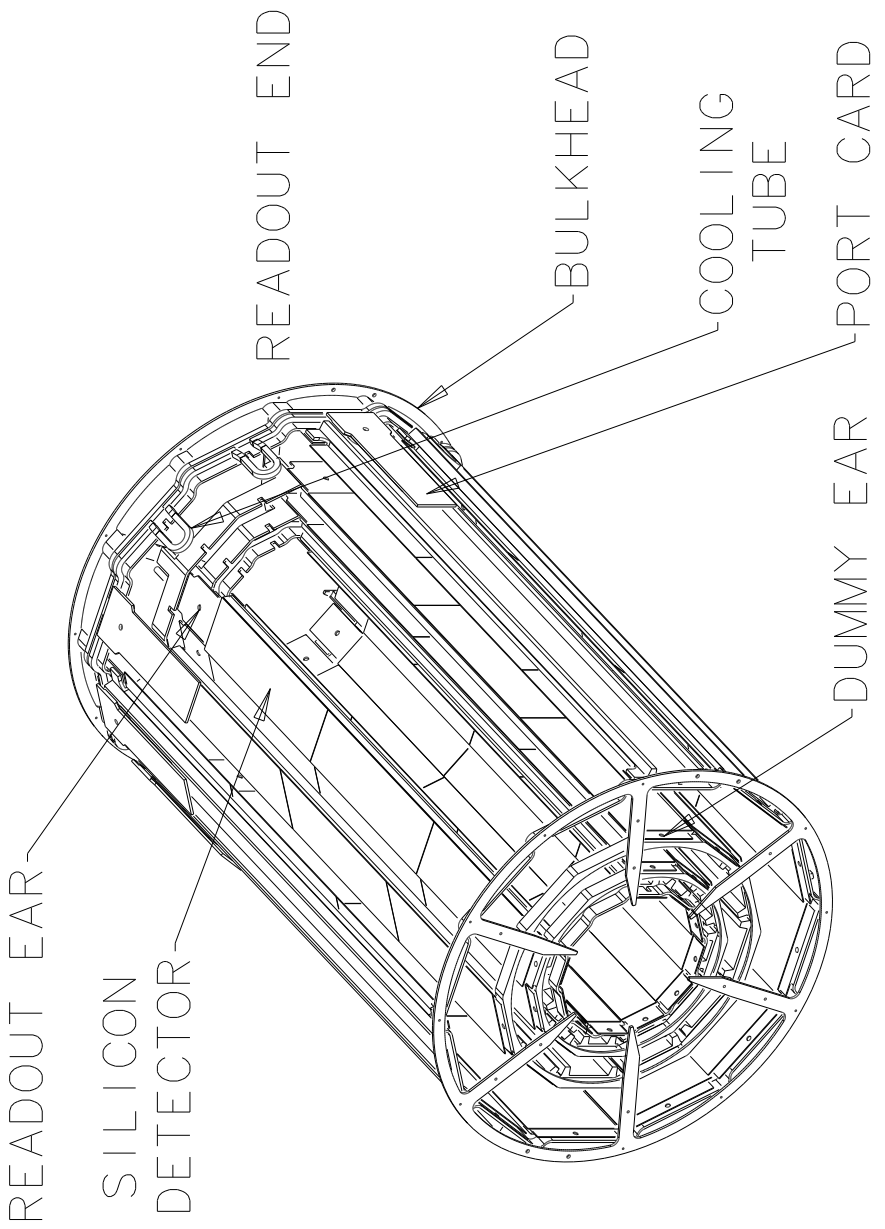

Figure 13: *Schematic view of one of the two SVX barrels.*

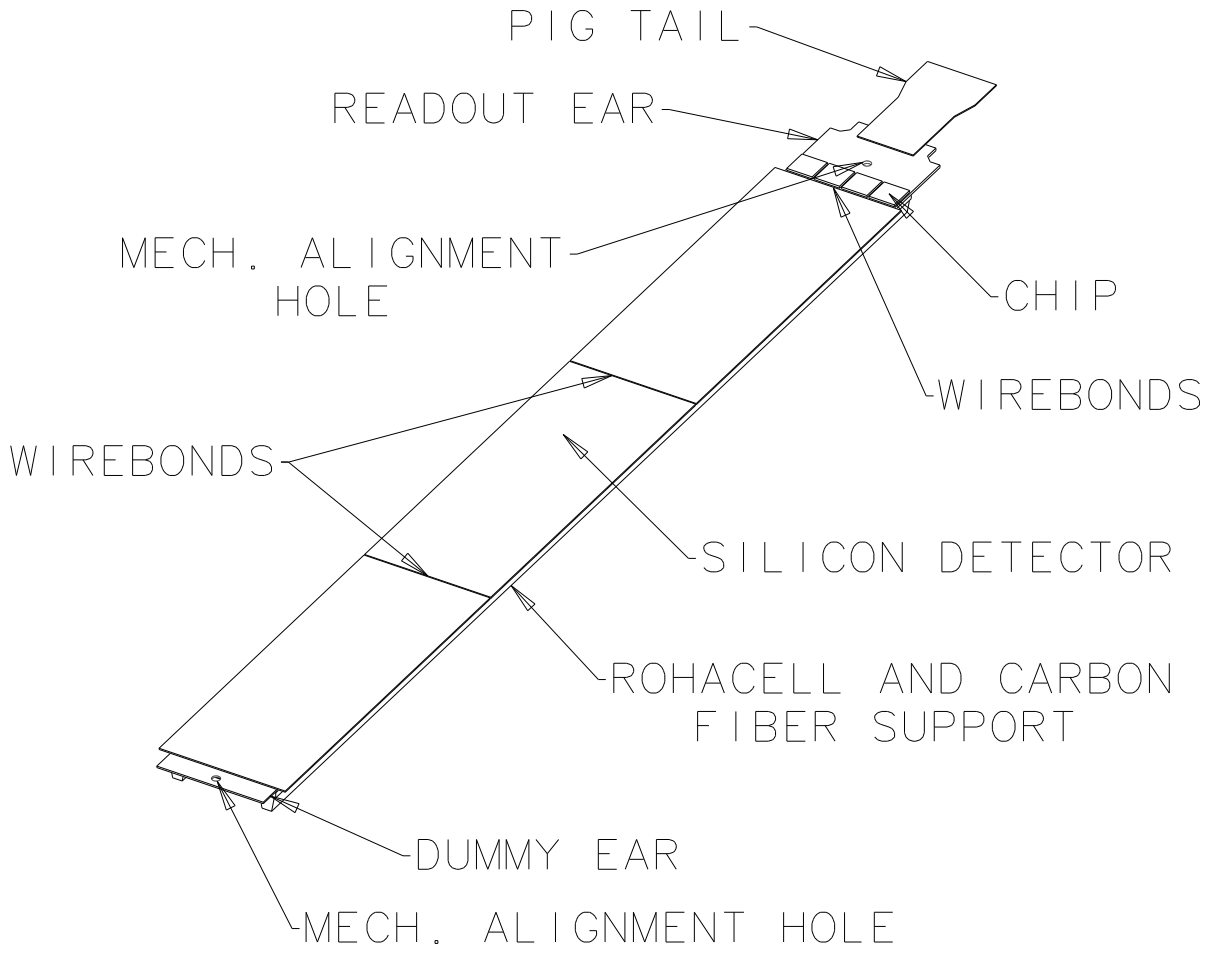

Figure 14: *Schematic view of one SVX ladder.*

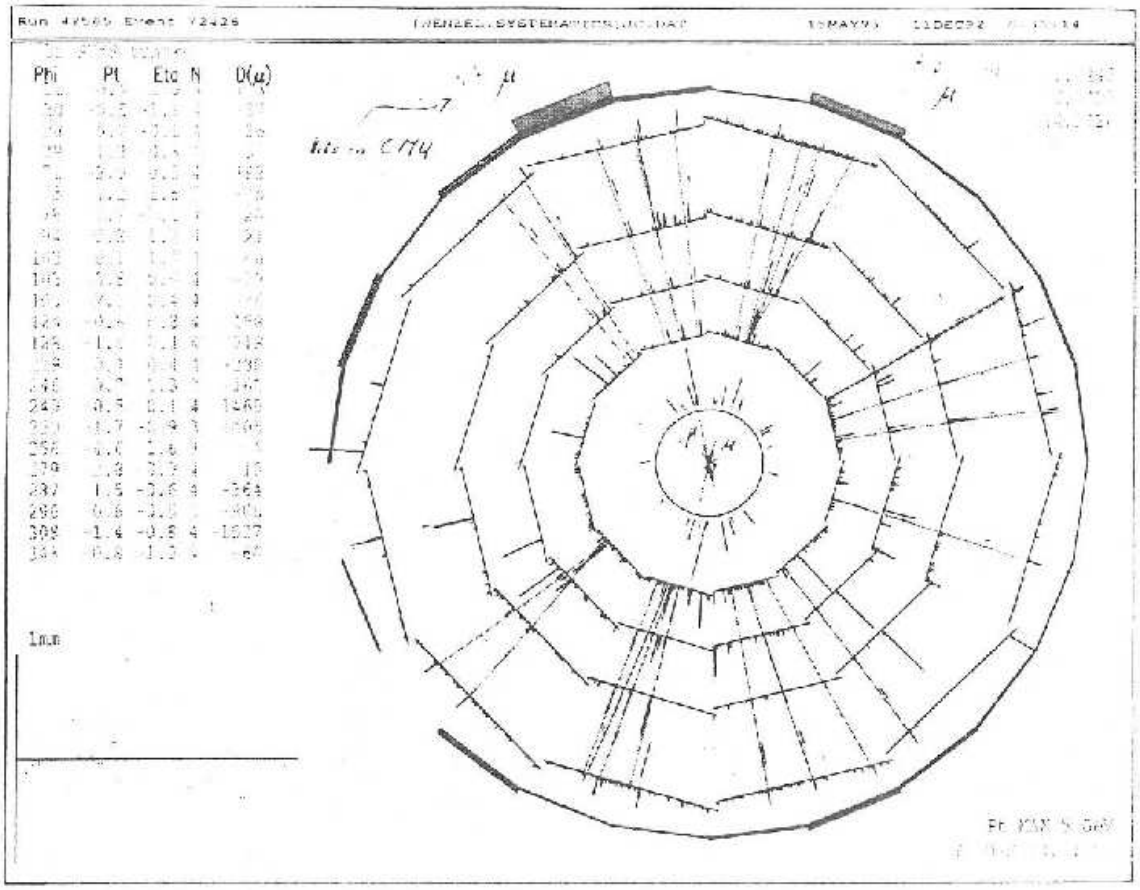

Figure 15: *Event display showing one barrel of the SVX.*

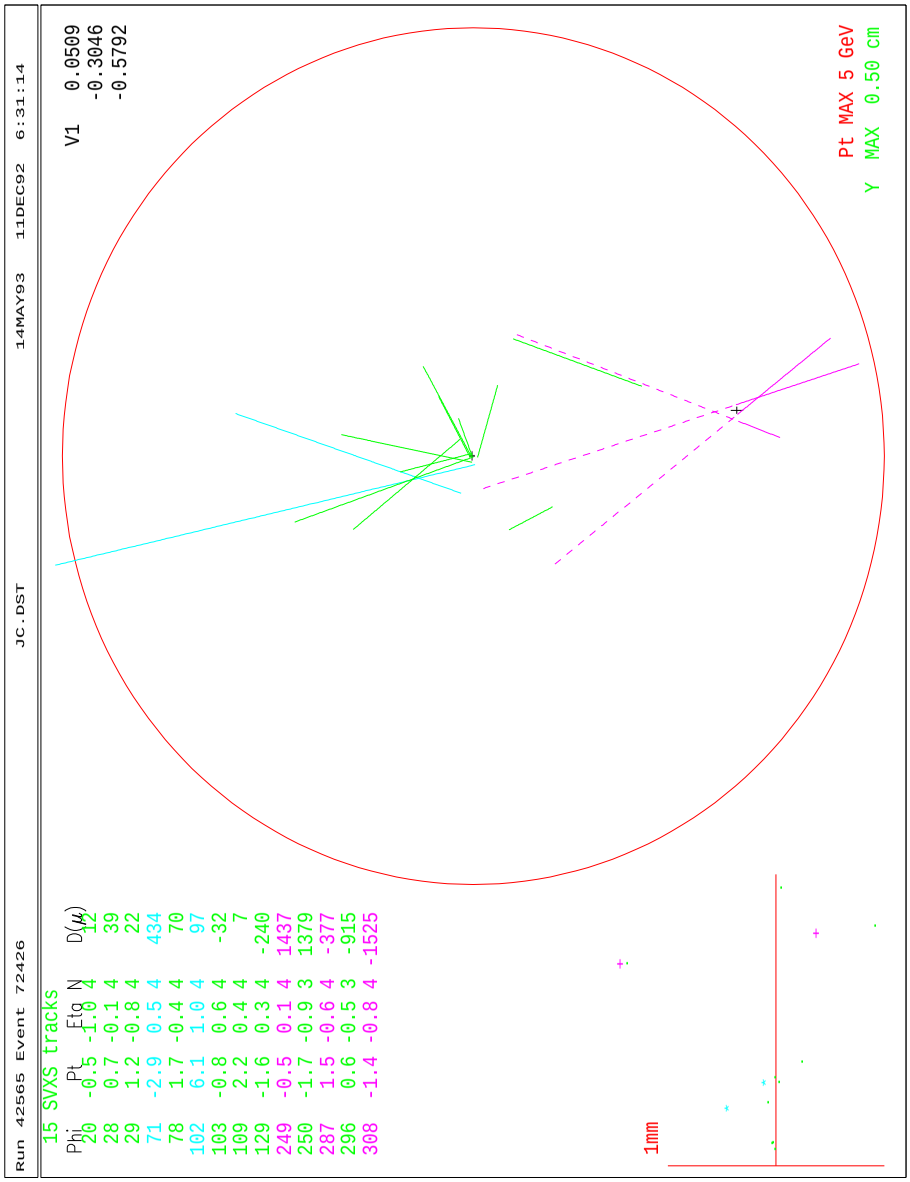

Figure 16: *Magnification of the event display shown in the previous figure. The radius of the drawn circle is 0.5 cm*

2.8 Tracking in the SVX

2.8.1 Track Parameterization

In a homogenous magnetic field tracks of charged particles travel on a helix with the axis of the helix parallel to the magnetic field (see Figure 17). At CDF the following 5 parameters are used to describe the helix of a charged track:

$$\vec{\alpha} = (\cot\theta, C, z_0, D, \varphi_0)$$

where:

$\cot\theta$	:	cotangent of the polar angle at minimum approach.
C	:	half curvature (same sign as the charge of the particle).
z_0	:	z position at point of minimum approach to origin.
D	:	signed impact parameter which is the distance between helix and origin, at minimum approach in the transverse plane.
φ_0	:	φ-direction of track at point of minimum approach.

At CDF the direction of the magnetic field is in the negative z direction. The z direction is defined as the direction of the protons, which are pointing east at the B0 interaction point. The curvature by definition has the same sign as the charge Q of the particle. If (x_0, y_0) is the center of the circle then the impact parameter which is a signed variable is calculated in the following way: $D = Q \cdot (\sqrt{x_0^2 + y_0^2} - \rho)$ where $\rho = \frac{1}{|2C|} = \frac{1}{2QC}$ is the radius of the circle.

In the CDF parameterization the following track equations can be derived (see [49]) to describe the trajectory of a track as a function of the distance R from the origin of the coordinate system.

$$\varphi(R, \vec{\alpha}) = \varphi_0 + \sin^{-1}\left(\frac{CR + (1 + CD)D/R}{1 + 2CD}\right) \tag{21}$$

$$Z(R, \vec{\alpha}) = z_0 + \frac{\cot\theta}{C}\sin^{-1}\left(C\sqrt{\frac{R^2 - D^2}{1 + 2CD}}\right) \tag{22}$$

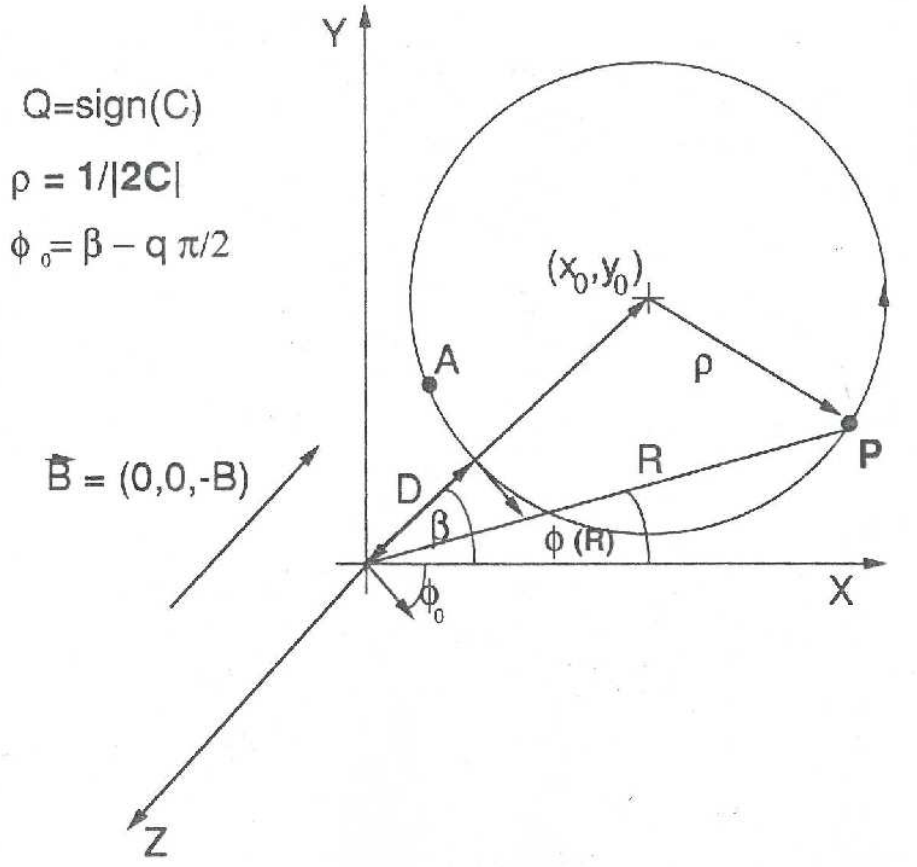

Figure 17: *Track of particle with positive charge.*

2.8.2 The SVX Track Algorithm (SVXREC)

The derivation of the tracking algorithm that is used at CDF as well as a comparison with other algorithms can be found in [48]. I will recall here the main idea. A more detailed description can be found in [49], where the formulas as they appear in the CDF parameterization are also explained in detail.

The algorithm we use is called the 'Progressive method' since it starts with the result of a fit downstream (that means the CTC fit) and then updates the fit whenever there is a new hit found in the detector closer to the interaction point (SVX). This algorithm has several advantages:

- The method is fast and stable. At each update of the fit only matrices of dimension 5×5 have to be inverted. It makes optimal use of the fit in the outer detector (CTC).
- We follow real tracks into the SVX and thus combine pattern recognition and track fitting. In case there is more than one candidate track the χ^2 as defined below is used to choose the best candidate.
- multiple scattering is treated correctly.

When a new measuring point is added the new parameters are calculated using the following formula:

$$\vec{\alpha}' = \vec{\alpha}_0 + [(V_0^*)^{-1} + A]^{-1} \cdot \frac{\partial x}{\partial \vec{\alpha}} \cdot \frac{x' - x(\vec{\alpha}_0)}{\sigma_x^2} \tag{23}$$

where:

$\vec{\alpha}$	:	$(cot\theta, C, z_0, D, \varphi_0)$
α_0	:	result before updating the fit
x'	:	measured point in the Rφ-plane
$x(\vec{\alpha}_0)$	:	predicted Rφ position of previous fit
σ_x	:	sigma of Rφ measurement (detector resolution)
$\frac{\partial x}{\partial \vec{\alpha}}$	:	derivatives of the track equation w.r.t. track parameters (see [49])

The matrices A and V_0^* are defined in the following way:

$$A_{ij} = \frac{1}{\sigma_x^2} \cdot \frac{\partial x}{\partial \alpha_i} \frac{\partial x}{\partial \alpha_j} \tag{24}$$

and

$$V_0^* = V_0 + V_{MS} \tag{25}$$

where V_0 is the covariance matrix after the last update of the fit and V_{MS} is the multiple scattering contribution (see e.g. [49] and references therein). The new covariance matrix is calculated using the following formula:

$$V' = [(V_0^*)^{-1} + A]^{-1}. \tag{26}$$

Finally the χ^2 is updated:

$$\chi^2 = \chi_0^2 + (\Delta\vec{\alpha})^t \, (V_0^*)^{-1} \, \Delta\vec{\alpha} + \frac{(x(\vec{\alpha}_0) - x')^2}{\sigma_x^2} \tag{27}$$

where:

$\Delta\vec{\alpha} = \vec{\alpha}' - \vec{\alpha}_0$: difference between parameters from previous fit and updated fit.

χ_0^2 : χ^2 before update.

The χ^2 is by definition a mixed quantity. The first term expresses the error to extrapolate the track from the previous fit to the new measuring plane using the covariance matrix (including multiple scattering to get from the last update to the next measuring plane) to give it the proper weight. At the first update this is the contribution to extrapolate the track from the CTC into the SVX which means that the SVX-χ^2 is not completely decoupled from the CTC fit. The second term reflects the detector resolution.

Multiple scattering produced by the material between the different detectors or measuring planes causes loss of information. This has to be taken into account in the covariance matrix by adding a multiple scattering matrix to the covariance matrix of the track parameters: $V_0^* = V_0 + V_{MS}$.

The effect of multiple scattering is calculated in the small-angle approximation. The r.m.s. of the multiple scattering angle is given by the empirical formula:

$$\theta_{MS} = \frac{0.0136}{\beta c P} z \sqrt{s^*/X_0} \, (1 + 0.038 \ln(s^*/X_0)) \tag{28}$$

taken from [3], where X_0 is the radiation length of the traversed material, s^* is the actual thickness of material traversed and z is the charge number of the incident particle. This approximation is proved to be good on the 10-20 % level.

One can measure the actual impact parameter resolution $\sigma_D(P_t)$. As described in section 3.4 the transverse profile of the beam can be described with a circular gaussian with a sigma in the order of 36 to 38 μm which is small compared to the impact parameter resolution of low P_t tracks. We assume that most of the tracks are prompt tracks coming from the primary interaction point. To ensure well measured tracks we require them to be three dimensional, to have 4 Hits in the SVX, the SVX χ^2 to be less then 20 and the z coordinate to be well measured. Figure 18 shows how the impact parameter calculated with respect to the beam position scatters as a function of P_t. One observes that the distribution becomes wider for low momentum tracks while for high P_t-tracks the sigma of the beamprofile is the dominant contribution. The next step is to make 100 MeV/c wide slices in P_t of the two dimensional distribution shown in Figure 18. The sigma of this distributions is calculated by fitting a gaussian to these one dimensional distributions. The fitted sigma is related to the width of the beam σ_{beam} and the impact parameter resolution $\sigma_D(P_t)$ in the following way:

$$\sigma^2 = \sigma_D(P_t)^2 + \sigma_{beam}^2.$$

Thus one obtains for $\sigma_D(P_t)$:

$$\sigma_D(P_t) = \sqrt{\sigma^2 - \sigma_{beam}^2}.$$

Figure 19 shows the impact parameter resolution as a function of the transverse momentum obtained in this way. One can see that multiple scattering is the dominating contribution to the impact parameter resolution for low momentum tracks. The asymptotic resolution for high P_t tracks, where the intrinsic detector resolution dominates, is in the order of 10 μm. A fit to the data of the following form:

$$\sigma_D(P_t) = A + B\frac{1}{P_t} \tag{29}$$

results in $A \approx 10\mu m$ and $B \approx 41\mu m$ GeV/c. A is the asymptotic resolution ($P_t \to \infty$) depending on the distance of the first measuring plane from the

interaction vertex and the internal resolution of the silicon detector. The slope B is a function of the amount of material causing multiple scattering. It is remarkable how well this measurement agrees with calculations obtained from a full detector simulation. Fitting over the same range one obtains: $A \approx 10\mu m$ and $B \approx 39\mu m$ GeV/c. Figure 20 shows the impact parameter resolution obtained from a full detector simulation in the P_t-range from 0.4 to 15 GeV/c.

In addition the SVX extends the lever arm of the tracking by about 30 cm and adds 4 precise points to the CTC Track fit. This improves the precision of the momentum measurement significantly. Figure 21 shows the calculated error σ_{P_t}/P_t as a function of P_t. A linear fit gives [1]:

$$\frac{\sigma_{(P_t)}}{P_t} = 0.0011 + 0.0014 \times P_t \quad (CTC)$$

and

$$\frac{\sigma_{(P_t)}}{P_t} = 0.0024 + 0.00044 \times P_t \quad (CTC + SVX)$$

[1]Before rescaling the CTC covariance matrix by a factor 2.5 (see section 4).

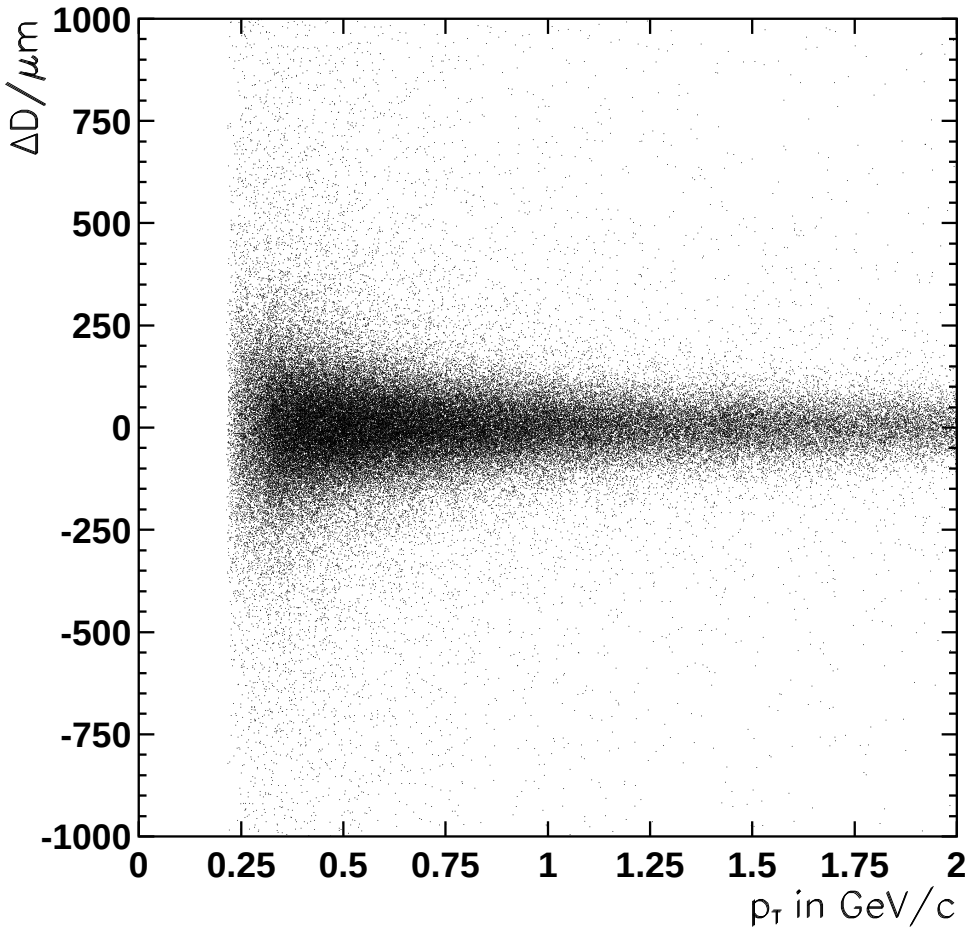

Figure 18: *Impact parameter distribution of tracks measured in the SVX with respect to the beamposition as a function of P_t.*

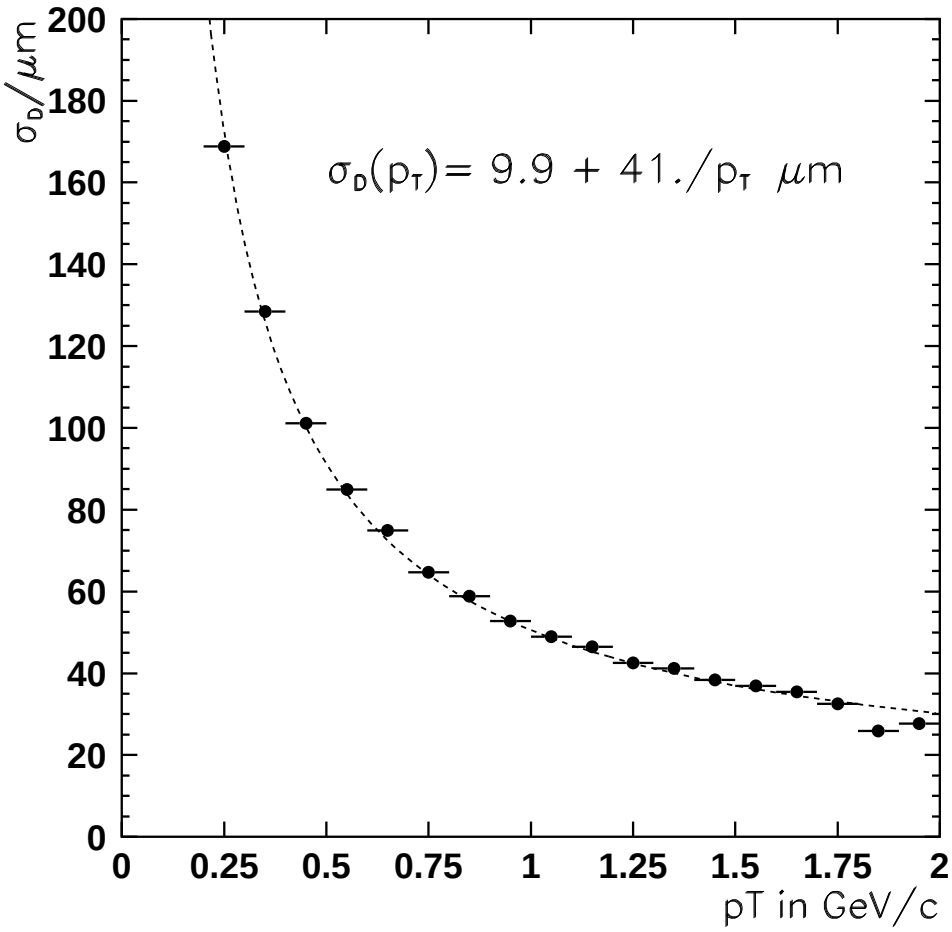

Figure 19: *Impact parameter resolution as a function of P_t obtained from data.*

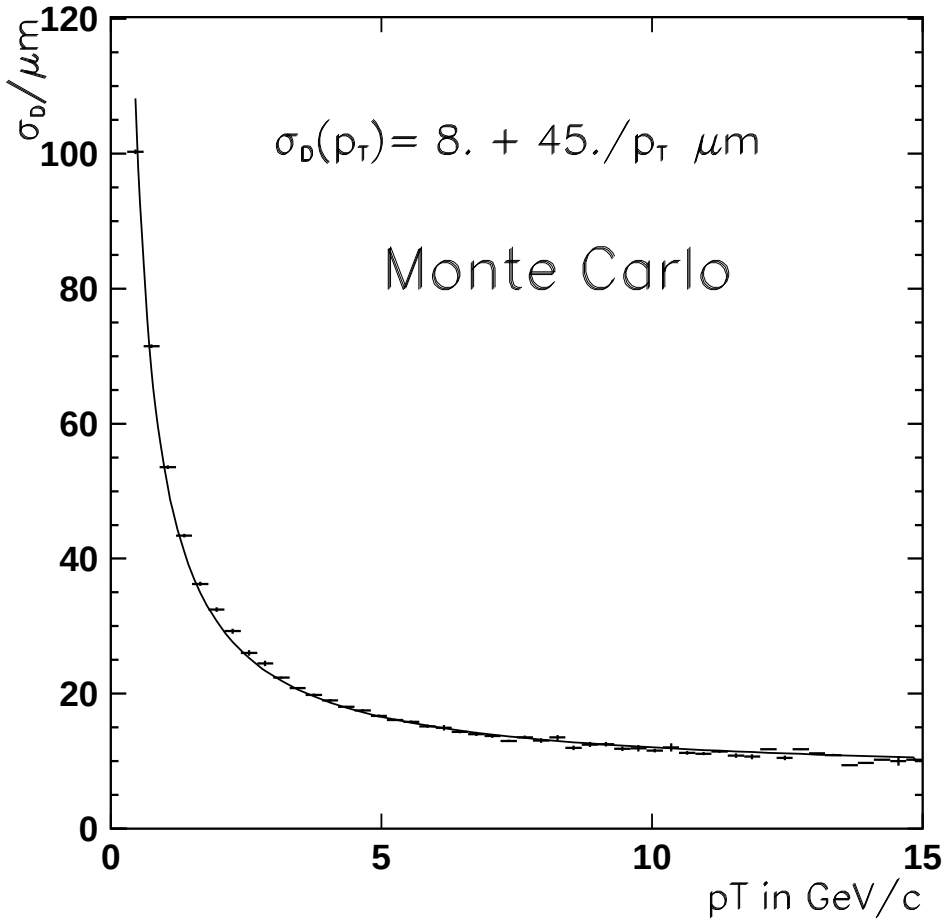

Figure 20: *Impact parameter resolution as a function of track P_t obtained by a full detector simulation (MC).*

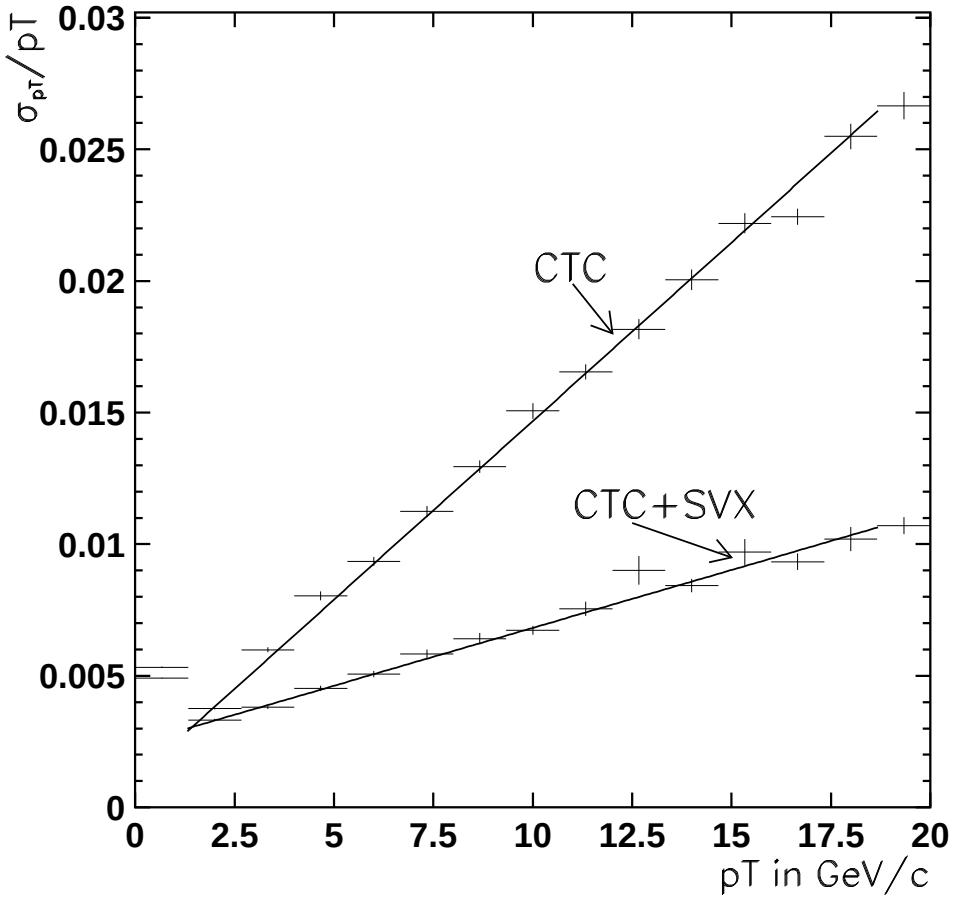

Figure 21: *Momentum resolution as a function of* P_t.

3 Extracting the B Lifetime from the Data

The steps involved in measuring the B lifetime from the inclusive J/ψ sample are:

- Measure the 2 dimensional decay length L_{xy} for a sample of J/ψ's.
- Correct the measured L_{xy} of the J/ψ's for the difference between the $\beta\gamma$ of the J/ψ's and the $\beta\gamma$ of the B hadron. The distribution of this corrected decay distance, which closely approximates the $c\tau$ distribution of the B's, is called the 'pseudo $c\tau$' distribution.
- Measure the 'pseudo $c\tau$' distribution of the background under the J/ψ by studying the J/ψ sidebands.
- Fit the background-subtracted 'pseudo $c\tau$' distribution to the sum of direct (zero-lifetime) and B decay (non-zero lifetime) contributions and extract the lifetime.

We describe each of these steps in more detail below.

3.1 The Transverse Decay Length L_{xy} and the Definition of the 'Pseudo $c\tau$' λ_{corr}

Figure 22 shows the decay of a b-hadron into J/ψ X. Shown are the momentum vectors of the two muons, the J/ψ and the B-hadron.

The vector $\vec{X}$ is the vector pointing from the primary vertex to the secondary vertex in the transverse plane:

$$\vec{X} = \vec{x}_{\psi} - \vec{x}_{prim} \tag{30}$$

L_{xy} is then defined as the projection of this vector onto the momentum of the J/ψ:

$$L_{xy} = \frac{\vec{X} \cdot \vec{P_t^{\psi}}}{|\vec{P_t^{\psi}}|} = (x_{\psi} - x_{prim}) \cdot \frac{P_x^{\psi}}{P_t^{\psi}} + (y_{\psi} - y_{prim}) \cdot \frac{P_y^{\psi}}{P_t^{\psi}} \tag{31}$$

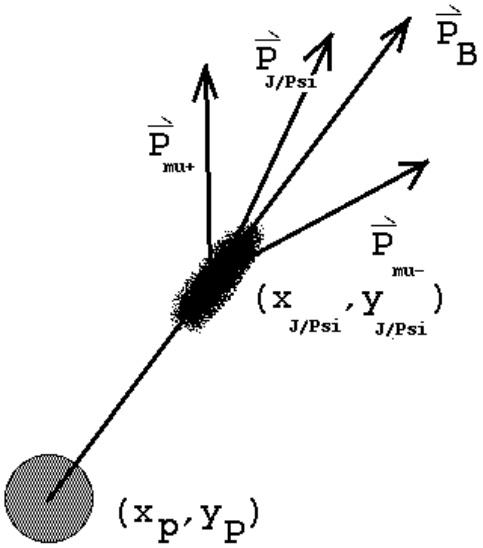

Figure 22: *B-decay projected on the plane transverse to the beam.*

Using error propagation and assuming that the only relevant contributions come from the error on the J/ψ and the primary vertex coordinates, one gets the following expression for the experimental error in L_{xy}:

$$\sigma^2_{L_{xy}} = \frac{1}{\left(P_t^{\psi}\right)^2} \cdot \left[(\sigma_{xv} P_{x\psi})^2 + 2\sigma_{xyv} P_{x\psi} P_{y\psi} + (\sigma_{yv} P_{y\psi})^2 + (\sigma_{xp} P_{x\psi})^2 + (\sigma_{yp} P_{y\psi})^2 \right]$$

where:

σ^2_{xv}, σ^2_{xv}, σ^2_{xyv}	:	covariance matrix elements from the fit to the secondary vertex
σ_{xp}, σ_{yp}	:	sigma of the primary vertex (beamspot) in x and y
P_t^{ψ}	:	transverse momentum of J/ψ
$P_{x\psi}$, $P_{y\psi}$	:	x, y components of J/ψ momentum

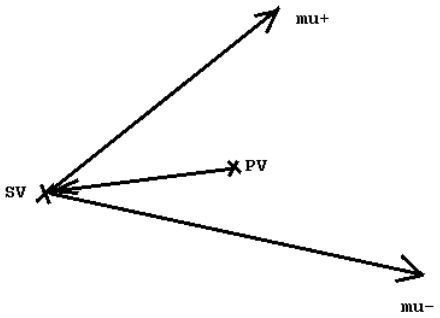

Figure 23: *'Unlikely' decay configuration (sv: secondary vertex, pv: primary vertex).*

L_{xy} is a 'signed' variable. It is negative for the 'unlikely' configuration shown in Fig. 23 where it seems that the particle decays before the point where it was produced. For a 0-Lifetime sample one expects a gaussian distribution peaked at $L_{xy} = 0$. Experimental tests of this expectation will be presented in section 4.2

In this analysis we will attempt to measure the $c\tau$ of the original B-hadron:

$$\lambda_B = \frac{\vec{X} \cdot \vec{p}_t^B}{p_t^B} \cdot \frac{1}{(\beta\gamma)_t^B} = \frac{M_B \vec{X} \cdot \vec{p}_t^B}{(p_t^B)^2} \tag{32}$$

Since the J/ψ's selected by our trigger have basically the same direction as the parent B-hadrons (see Fig. 24) and carry most of the B-momentum, one can use the relativistic quantity $(\beta\gamma)_t^\psi$ of the J/ψ as a first approximation to λ_B,

$$\lambda = L_{xy} \cdot \frac{M_\psi}{p_t^\psi} \tag{33}$$

One then applies a correction factor (derived from Monte Carlo) to connect λ and λ_B,

$$F_{corr}(p_t^\psi) = \frac{\lambda}{\lambda_B}. \tag{34}$$

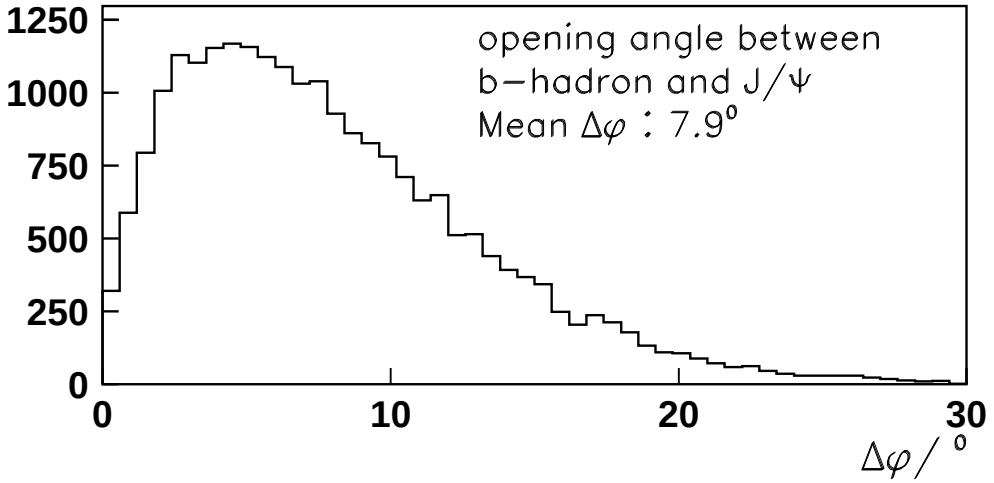

Figure 24: *Opening angle between b-hadron and* J/ψ.

The method for obtaining this correction factor is described in section 3.2. With this definition of F_{corr}, the variable 'pseudo $c\tau$' (λ_{corr}) is defined as follows:

$$\lambda_{corr} = \frac{\lambda}{F_{corr}(P_t^{\psi})} = L_{xy} \cdot \frac{M_{\psi}}{P_t^{\psi} F_{corr}(P_t^{\psi})} \tag{35}$$

3.2 Monte Carlo Determination of F_{corr}

To obtain the correction factor F_{corr} and to study the systematics involved when doing this correction a simple 'Toy' Monte Carlo: BGENJMU was used. This simple Monte Carlo is very fast compared to a full MC generator and detector simulation. In addition it is much easier to modify and to separate the contributions from each effect. It is therefore easy to include systematic effects such as trigger bias as a function of the impact parameter. The basic steps of BGENJMU are shown in Figure 25.

At the beginning b-quarks are produced using a given P_t distribution. We use by default the b-quark P_t-spectrum as calculated by Nason, Dawson and Ellis (NDE). The b-quark P_t-spectrum obtained from this calculation is shown in Figure 26. Note to obtain the correction factor only the shape of the P_t spectrum matters not the overall normalization (cross section).

In order to study the systematic uncertainties associated with the modeling of the b P_t spectrum, we have also studied a simple power law model.

$$\frac{d\sigma}{dp_t^2} = \frac{A}{(p_t^2 + m_b^2)^n} \tag{36}$$

The exponent n was varied in the Monte Carlo and the resulting P_t spectrum of the J/ψ's was compared to the spectrum measured in the data for J/ψ's with decay length greater than 200 microns (the assumption being that all such J/ψ's result from B decay). An exponent of 2.9 gives the best agreement with the data.

The second step is to fragment the b-quark to hadrons using the Peterson fragmentation function as described in section 1.5. The fragmentation parameter ϵ_b was varied within the following range:

$$\epsilon_b = 0.006 \pm 0.002$$

The B hadrons then are decayed into J/ψ + X. The J/ψ momentum in the B rest frame is selected from a distribution that follows the experimental curves measured by ARGUS and CLEO [50] [51]. Figure 27 shows the spectrum as measured by ARGUS which was used as the default spectrum in our calculation of F_{corr}

The polarization of the J/ψ is modeled using the recent ARGUS and CLEO results [52] as a constraint:

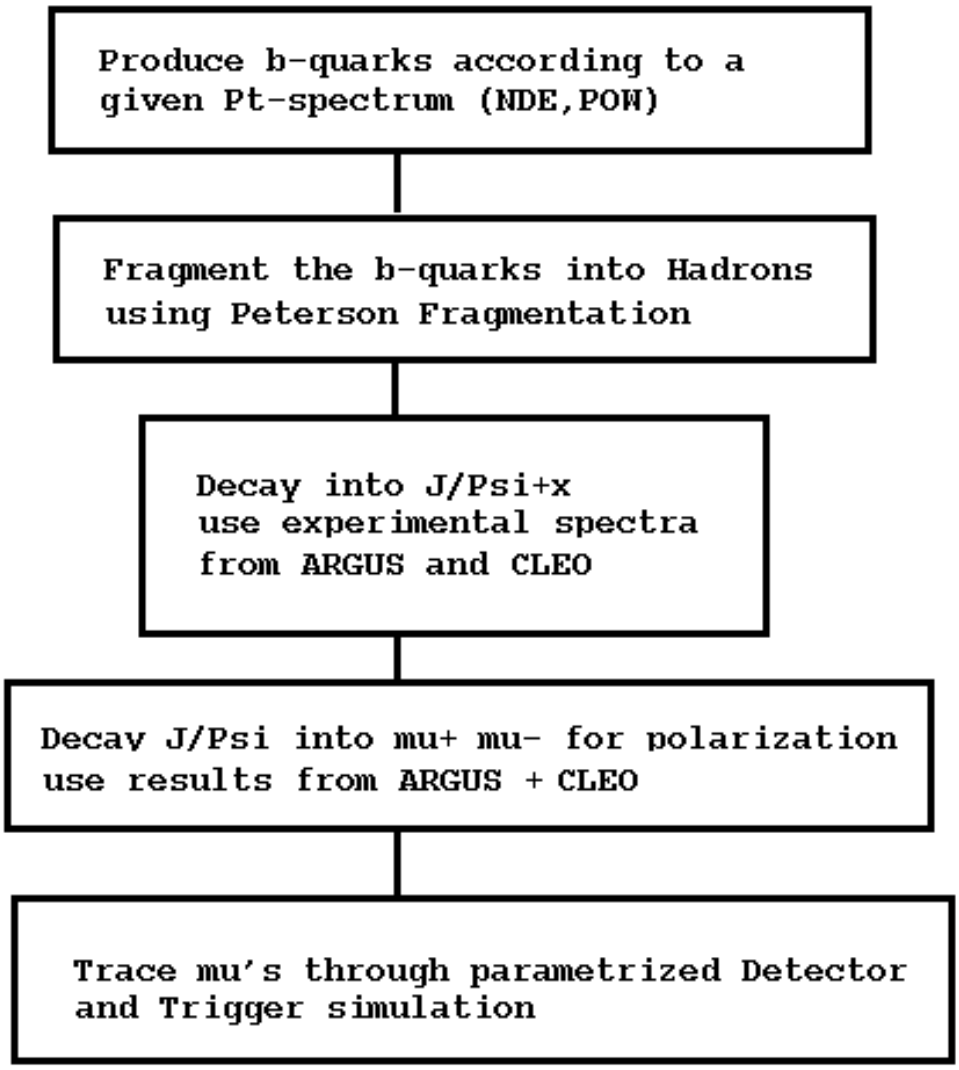

Figure 25: *Flow diagram of BGENJMU.*

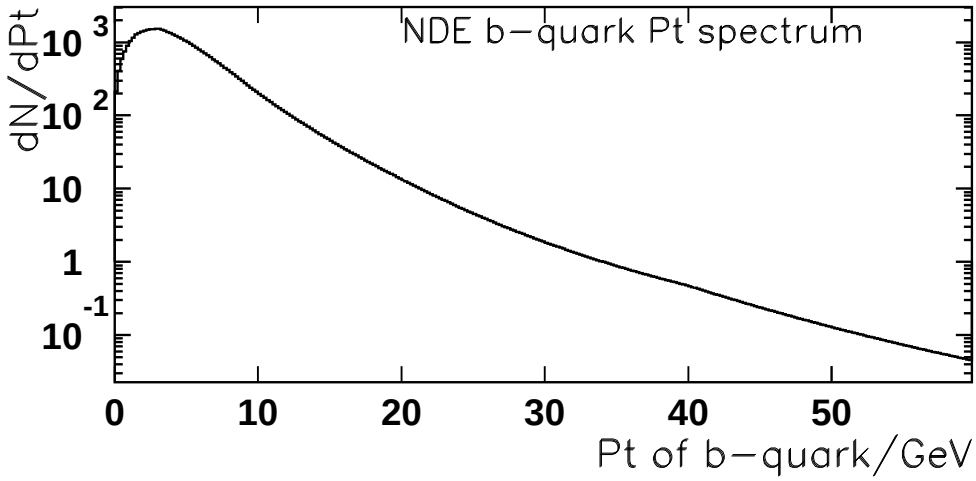

Figure 26: *b-quark momentum spectrum as calculated by NDE.*

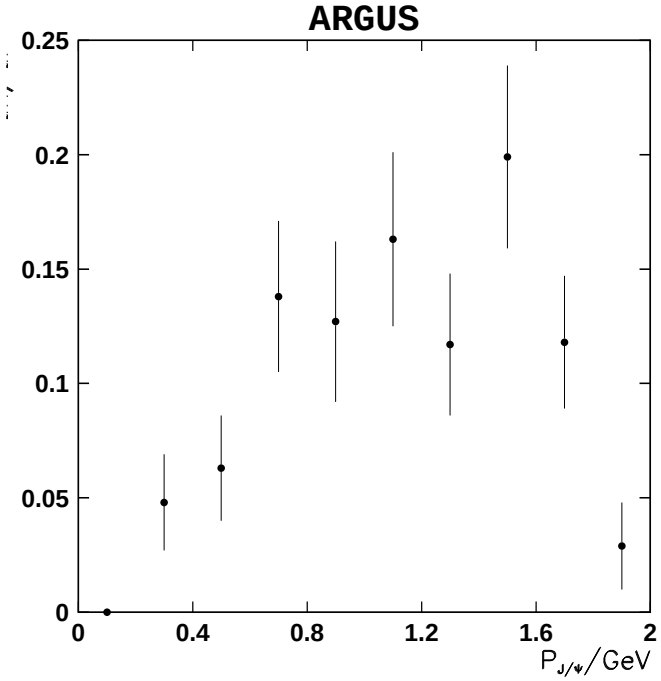

Figure 27: J/ψ*-momentum spectrum (uncorrected) in B-restframe as measured by ARGUS.*

$$\frac{\Gamma_L}{\Gamma_L + \Gamma_T} = 0.56 \pm 0.05\ (stat)\ \pm 0.05\ (syst)$$

for inclusive J/ψ production and

$$\frac{\Gamma_L}{\Gamma_L + \Gamma_T} = 0.78 \pm 0.09\ (stat)\ \pm 0.05\ (syst)$$

for inclusive J/ψ with $P_t > 1.4\ GeV/c$. Their result for the exclusive $J/\psi K^*$ sample gives the same result as the above, but with larger errors. We have decided to add one statistical σ and one systematic σ to their higher value and subtract one statistical σ and one systematic σ to their lower value to determine our range. Thus we will quote systematic uncertainties assuming:

$$0.46 \leq \frac{\Gamma_L}{\Gamma_L + \Gamma_T} \leq 0.92$$

The J/ψ's are then decayed into muons which are traced through a parameterized trigger and detector simulation. This simulation describes the turn-on and efficiency behavior of the central dimuon trigger and the geometrical acceptance of the central muon system and the SVX. It also includes the separation requirement in η and φ of the trigger. Level 1 of the central dimuon trigger requires 2 muon stubs in the central muon chambers which cover $|\eta| < 0.6$ in detector rapidity. Level 2 of this trigger then requires that at least one of the two muon legs is matched to a track in the CTC found by the CFT processor.

Figure 28 shows the result of a fit through the measured level 1 trigger efficiency as a function of P_t. Figure 29 shows the trigger efficiency for the level 2 CFT trigger. The measurement and parameterization of the trigger efficiencies are described in [53].

To check if this Monte Carlo is a good description of the data we compared the J/ψ P_t-spectrum from data with the spectra from different Monte Carlo models. Figure 30 shows the J/ψ P_t -spectrum we obtain after applying all the cuts described in section 4. A cut in pseudo c$\tau > 200$ μ m was applied to make sure that the majority of the J/ψ candidates are coming from b-decay. The shaded area shows the background as estimated by normalizing the sideband distribution to the same invariant mass area as the signal (see section 4).

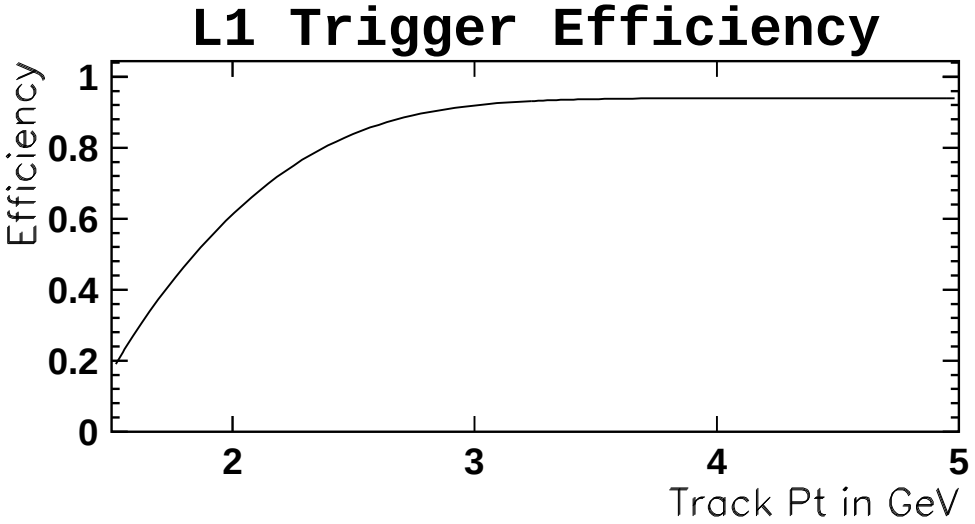

Figure 28: *L1 Trigger efficiency for muon stubs.*

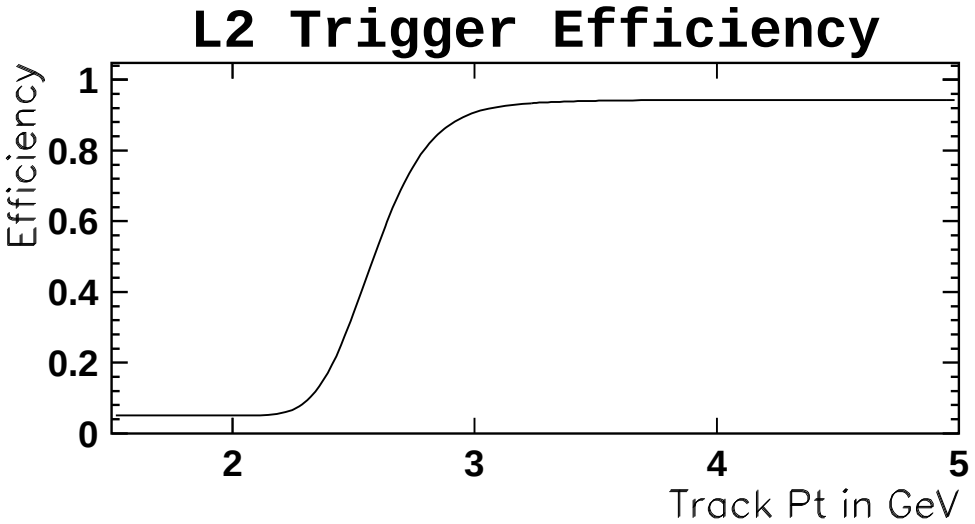

Figure 29: *L2 Trigger efficiency for muon stubs.*

Figure 31 compares the background subtracted J/ψ P_t-spectrum from data with two MC predictions. In one case the NDE b-quark spectrum was used, in the other case the power law with n=3.0. In both cases the J/ψ's are unpolarized, and for the fragmentation $\epsilon_b = 0.006$ was used. Both Monte Carlo distributions are softer in the first two P_t-bins which could be due to the fact that we have also used volunteers. That means it wasn't necessarily the two legs of the J/ψ which fired the trigger.

Table 5 compares the mean and R.M.S. of the J/ψ P_t-spectrum of Monte Carlo and data. The power law is softer while the NDE spectrum is harder than the data. This two spectra represent two extreme cases and the different results we obtain, when using this spectra to extract the lifetime from the data, were used in the estimation of the systematic error (see section 6).

	Mean GeV/c	RMS GeV/c
Data before BGR. subtraction	6.717	3.148
Data after BGR. subtraction	6.744	3.202
Background	6.709	3.118
Power Law (n = 3.0)	6.157	2.509
NDE	7.111	3.139

Table 5: *Comparison of mean value and RMS of the* J/ψ P_t*-spectrum of data and MC.*

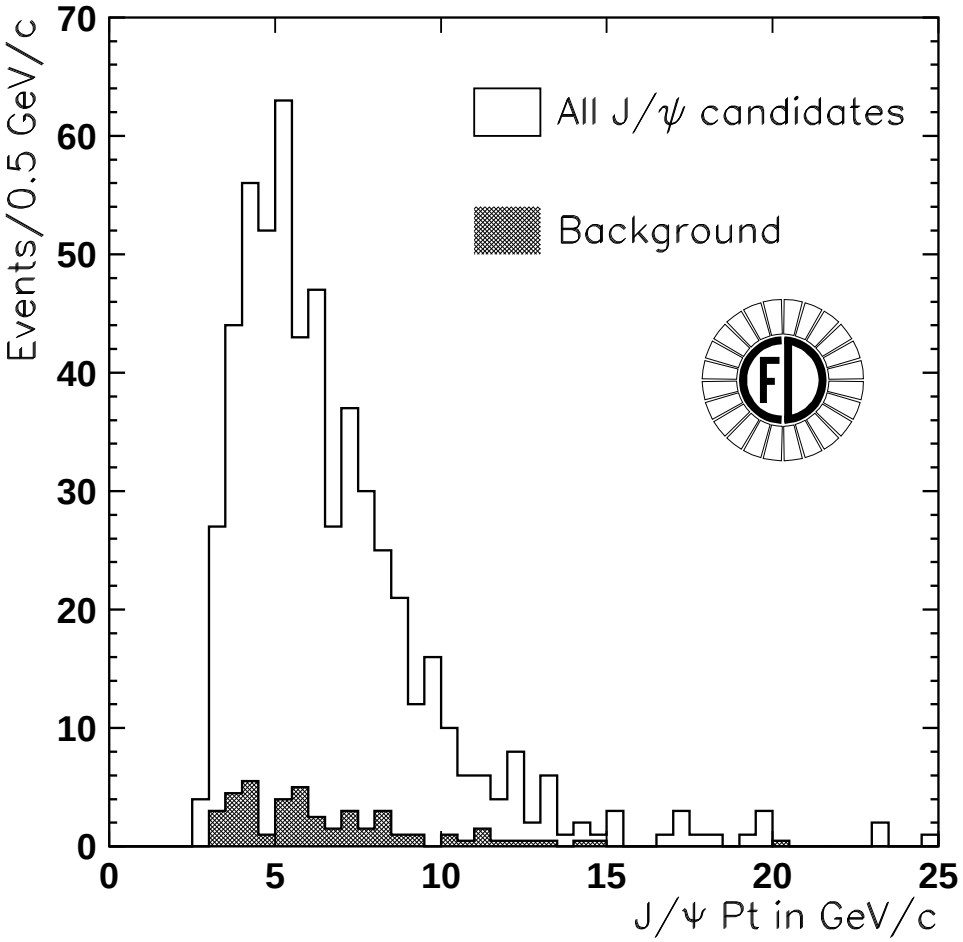

Figure 30: J/ψ P_t*-spectrum after all cuts* ($\lambda_{corr} > 200\ \mu m$)*. The shaded area shows the background as estimated by the sidebands.*

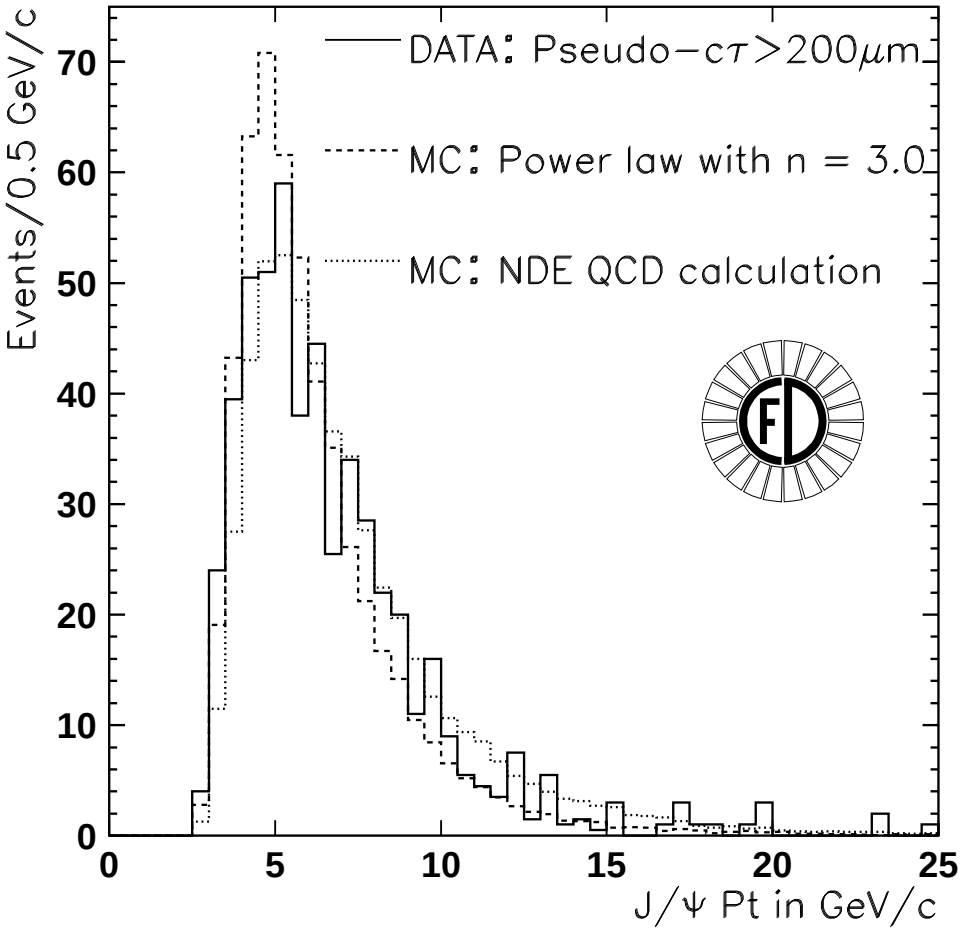

Figure 31: J/ψ P_t*-spectra for different models and data.*

3.3 The Correction Factor F_{corr}

The correction factor F_{corr} is finally obtained by averaging $(\beta\gamma)_t^B/(\beta\gamma)_t^\psi$ for different bins in P_t using MC events produced by BGENJMU. Figure 32 shows the correction factor as a function of P_t for 4 different parameterizations. The superimposed fit is of the following functional form:

$$F_{corr}(P_t^{\mathrm{J}/\psi}) = P1 \cdot exp(P2 \cdot P_t^{\mathrm{J}/\psi}) + P3$$

In all four cases the J/ψ was unpolarized and ϵ_b was set to 0.006. CL/AR stands for CLEO/ARGUS J/ψ-momentum spectrum in the B-meson rest-frame. POW29/NDE stands for power law with n= 2.9 and NDE NLO QCD prediction for the b-quark momentum spectrum. One observes that the correction factor is flat as a function of the transverse momentum of the J/ψ for $P_t^{\mathrm{J}/\psi} > 4$ GeV/c. The most part of the J/ψ selected by our trigger has a $P_t > 4$ GeV/c which is shown in Figure 30. Figure 33 shows the $(\beta\gamma)_t^B/(\beta\gamma)_t^\psi$- distributions for different P_t bins. The distributions are slightly asymmetric around the average.

To see if there is any bias to the lifetime by using the pseudo-$c\tau$ (or λ_{corr}) instead of the real $c\tau$ when extracting the lifetime from the data, both distributions were plotted for MC events. The input lifetime for the MC is 430 μm. The distributions are shown in Figure 34. The results of fitting exponentials with different fit ranges are summarized in Table 6. Within the statistical error the fits are in good agreement.

Fit range (cm)	real $c\tau$ (μm)	pseudo $c\tau$ (μm)
0. - 0.285	$429^{+2.9}_{-2.5}$	$427^{+2.4}_{-2.4}$
0.03 - 0.285	$427^{+3.5}_{-4.5}$	$434^{+4.4}_{-4.3}$

Table 6: *Comparison of $c\tau$ and pseudo-$c\tau$ distributions for MC events.*

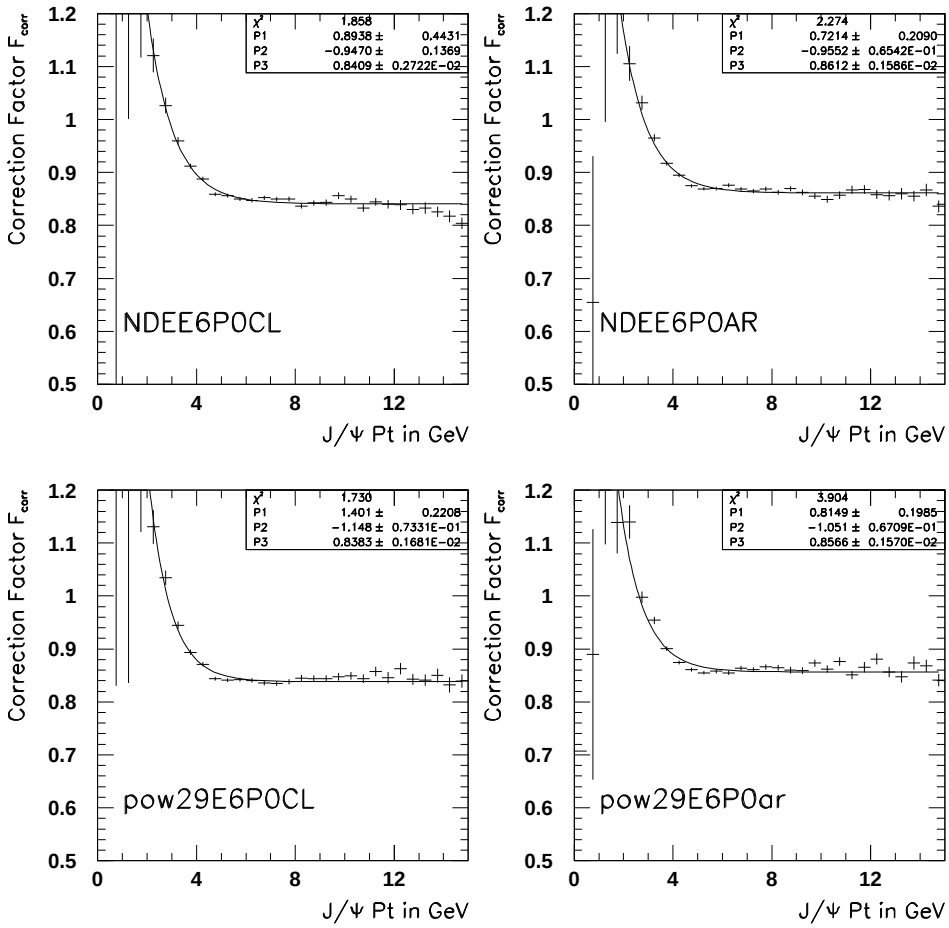

Figure 32: *F_{corr} for different parameterizations.*

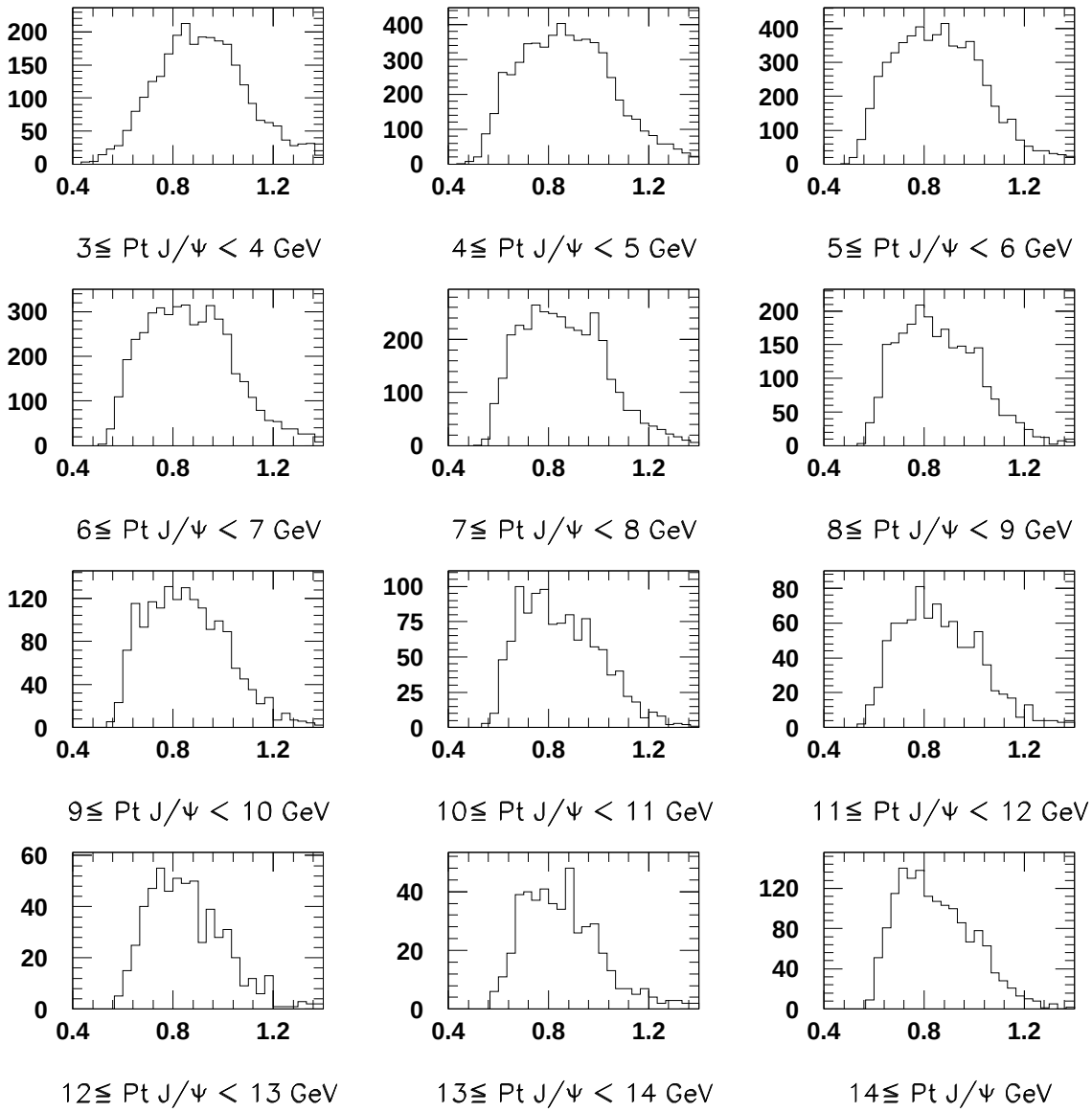

Figure 33: $(\beta\gamma)_t^B/(\beta\gamma)_t^\psi$- *distributions for different* P_t *bins.*

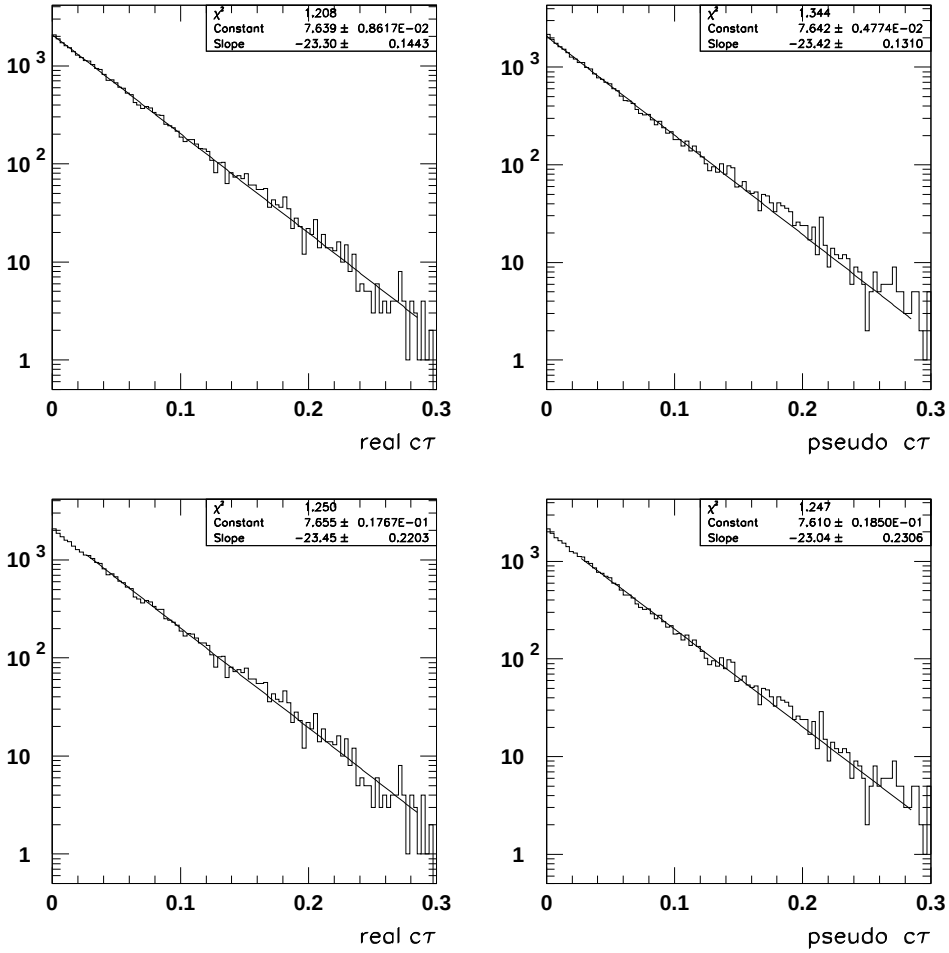

Figure 34: *Comparison of $c\tau$ and pseudo-$c\tau$ distributions for MC events. Superimposed is a fitted exponential curve.*

3.4 The Primary Interaction Vertex

The luminous region of CDF is quite long in z. The probability to interact as a function of z is approximately a gaussian function with a sigma of 30 cm. The beam is a straight line and can have some offset with respect to the z axis of the tracking detectors and is also not necessarily parallel to this axis. As will be shown below, the beamspot is circular and can be described with a gaussian with a sigma of 36 to 38 μm.

Different algorithms were tried to fit the beam position (see [54]). In the end the algorithm using the correlation between D and φ was the one which converged fastest and gave the most reliable result, even with low statistics. In the following this algorithm is described.

This algorithm is based on tracks, that means every selected track gives one point in the fit. For this algorithm no fitting of the primary vertex is necessary and it requires less data than the fit based on the fitted primary vertices (for a description of this alternative method see [54]).

To first order, neglecting the track curvature, the impact parameter D for tracks coming from the primary vertex can be parameterized in the following way:

$$D(\varphi_0, Z_0) = -x_0 \cdot \sin\varphi_0 - a_x \cdot \sin\varphi_0 \cdot Z_0 + y_0 \cdot \cos\varphi_0 + a_y \cdot \cos\varphi_0 \cdot Z_0 \quad (37)$$

where

x_0,y_0	:	position of the beam at z = 0
a_x, a_y	:	x and y slope of the beam

So the χ^2 to be minimized is:

$$\chi^2 = \sum_{i=1}^{N} \left(\frac{D_i - D(\varphi_0, Z_0)}{\sigma_i} \right)^2 \quad (38)$$

or with $\vec{x} = (x_0, y_0, a_x, a_y)$ and $\vec{g} = (\sin\varphi_0, -\cos\varphi_0, \sin\varphi_0 \cdot Z_0, -\cos\varphi_0 \cdot Z_0)$.

$$\chi^2 = \sum_{i=1}^{N} \left(\frac{D_i - \vec{x} \cdot \vec{g})}{\sigma_i} \right)^2 \quad (39)$$

where $\sigma_i^2 = \sigma_D^2 + 2 * \sigma_{Beam}^2$.

The solution for $\vec{x}$ is then:

$$\vec{x} = V \cdot \vec{sg} \tag{40}$$

Where the elements of the inverse of the 4 by 4 matrix V are defined in the following way:

$$V_{lm}^{-1} = \sum_{i=1}^{N} \frac{g_l \cdot g_m}{\sigma_i^2} \tag{41}$$

(l,m = 1,4)

and the components of the vector $\vec{sg}$ are:

$$sg_l = \sum_{i=1}^{N} \frac{g_l \cdot D_i}{\sigma_i^2} \tag{42}$$

(l=1,4)

Table 7 summarizes the requirements for the tracks used in the fit. In addition tracks crossing from one barrel to the other were rejected.

P_t of each track	:	>1.0 GeV/c
Distance from nominal beam position	:	<0.2 cm
Parameterization	:	3D
Nr. of hits in the SVX	:	4

Table 7: *Track selection cuts.*

The fitting was done iteratively. After every iteration the impact parameter cut with respect to the fitted beam position was tightened until 60% of the originally selected tracks survived. Plots number 1 and 2 in Figure 35 show the variation of the primary vertices with respect to the calculated beam position. The first plot is a two dimensional presentation of the x and y variation and shows the intensity profile of the beam. We see that the beam profile is gaussian and circular. Plot number 2 shows the x-projection of the first plot with a gaussian fit superimposed. The fitted gaussian is centered at 0 and the sigma (40 μm) is consistent with a sigma of the beam of about 36 μm convoluted with the error of the primary vertex fit. Plot number 3

shows the distribution of the primary vertex x versus z. The open triangles (circles) correspond to vertices measured in barrel 0 (1). The two straight lines are the result of a line fit just using the vertices found in one barrel.

To check the barrel-to-barrel alignment the fit was done for each barrel separately. Figure 36 shows the difference between the fitted x_0 and y_0 in the different modules of the SVX. We see that the difference between the barrels is very stable over the analyzed period. The mean value of the difference is about 5 μm in x and 4 μm in y. The right plot shows the difference divided by the convoluted error. If the errors are calculated correctly one would expect a gaussian distribution with a sigma of 1. This is the case within 10%.

One important question is if the beam is stable in time or if it is moving. It is expected that the beam position is fairly stable during a store. Since the fit was done on a run-by-run basis it is possible to compare the results of different runs for the same store. One observes that the beam moves on average only 5 microns in x and 11 microns in y from run to run. During a run the were less than 4 microns. So the beam is quite stable.

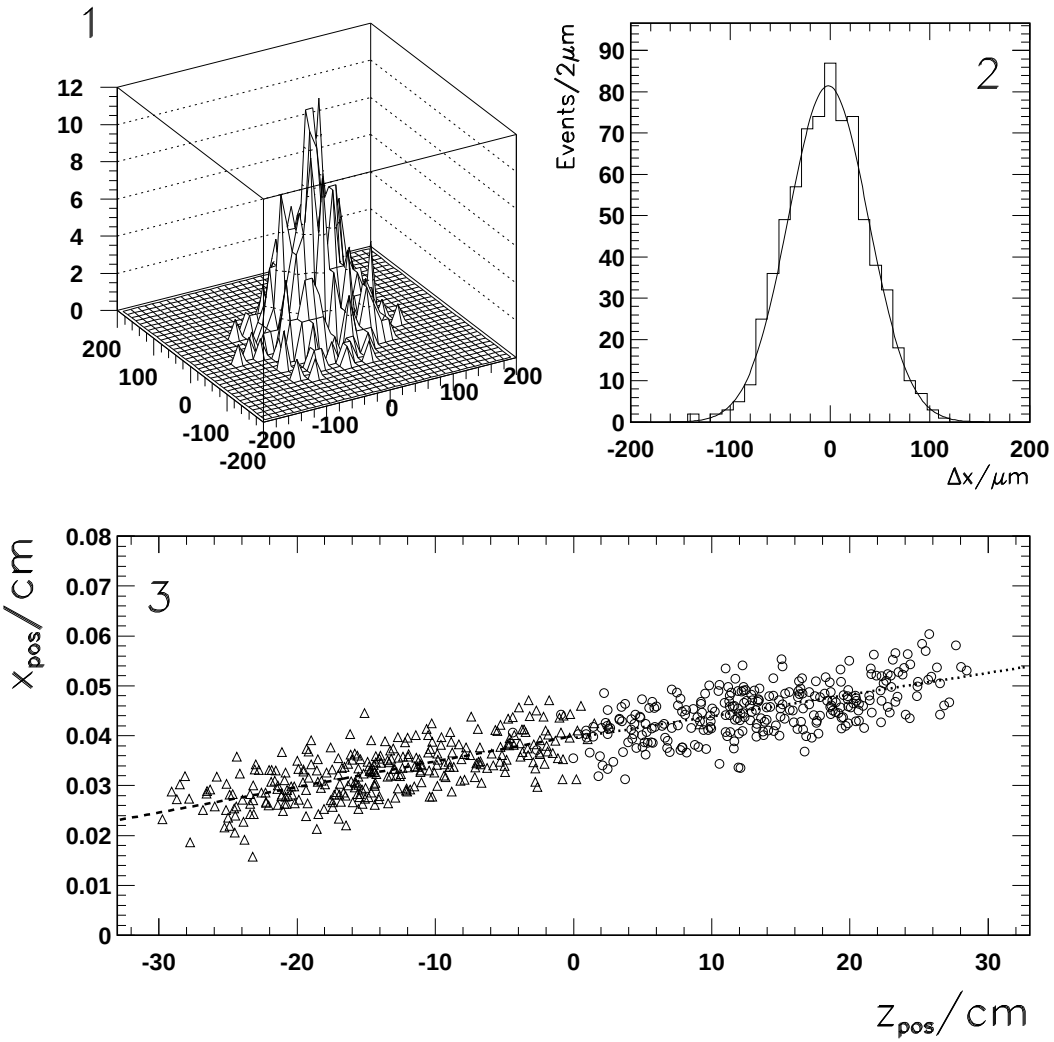

Figure 35: *Beam-profile (1 and 2) and z-distribution of the primary vertex(3).*

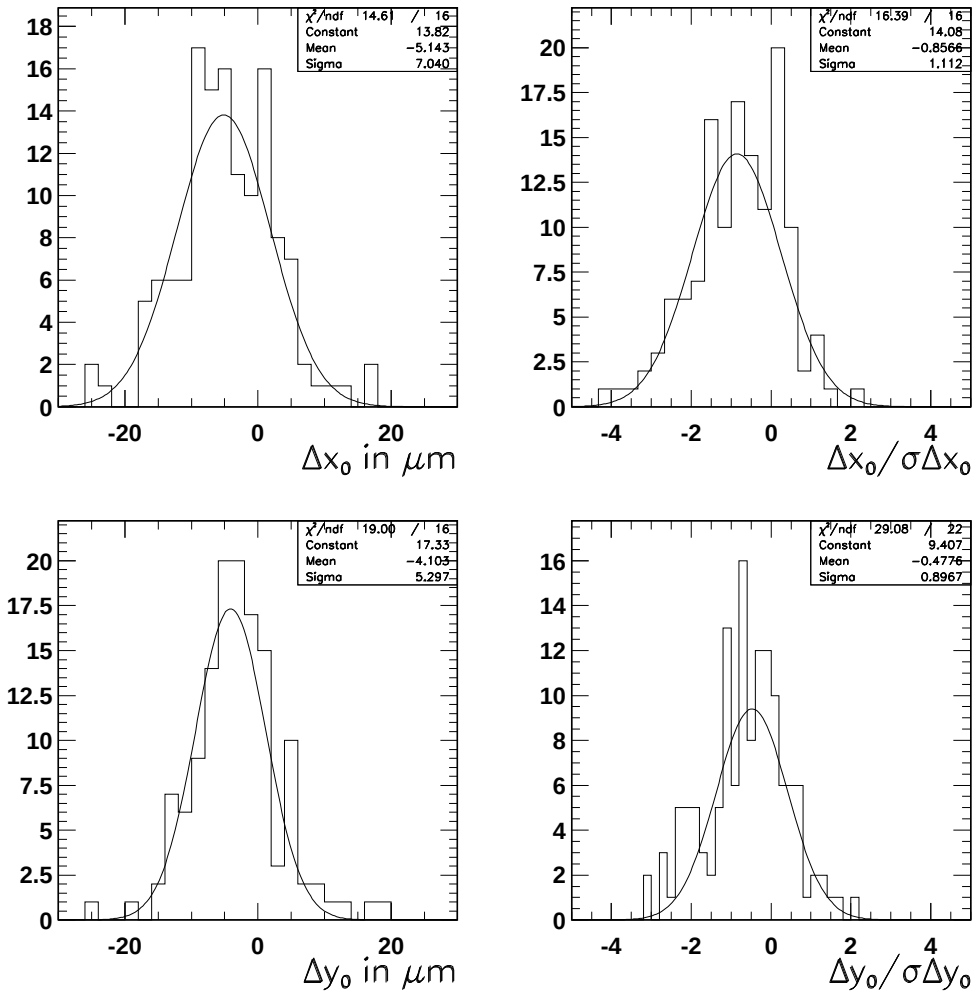

Figure 36: *Difference and normalized difference between the two SVX barrels in x_0 and y_0.*

3.5 The Secondary J/ψ Vertex

For the secondary vertex, a vertex-constrained fit using the two legs of the J/ψ was used. No pointing or mass constraints were applied to avoid any possible bias. Figure 37 shows the distribution of the calculated sigma in x and y as returned by the fit for the selected events.

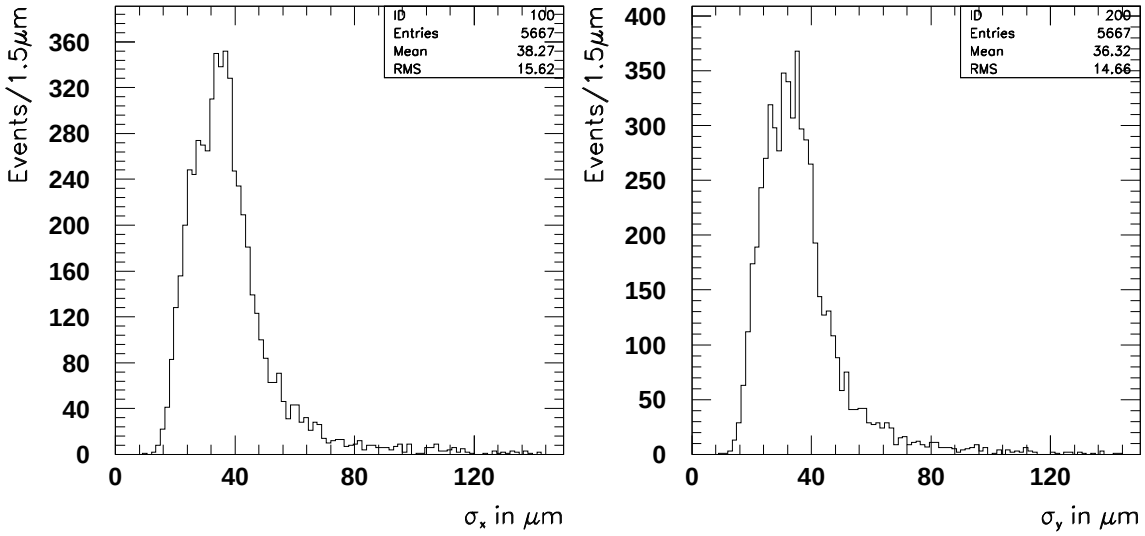

Figure 37: *Calculated error of secondary vertex fit for x and y.*

3.6 Fitting Techniques

The different fitting techniques as well as the background and signal parameterizations will be discussed in this section. Very similar methods to extract a lifetime from the data have been described in [55] and [56].

3.6.1 Background Parameterization

The shape of the background is obtained by parameterizing the pseudo $c\tau$ distribution of the side bands ($2.9 < M_\psi < 3.0$ *and* $3.2 < M_\psi < 3.3$). This distribution is shown in Figure 49. One observes that the background has clear non-gaussian tails. In addition, the distribution is clearly asymmetric, with a larger tail at positive lifetime. The presence of the non-zero lifetime component in the background sample is not surprising. One reason for the asymmetry is the presence of sequential semileptonic B decays in the dimuon sample.

The shape of the background distribution is parameterized as the sum of a central gaussian and left and right side exponentials of different slope.

$$g_{bkg}(\lambda_{corr}) = (1 - f_1 - f_2)\frac{e^{-\frac{\lambda_{corr}^2}{2\sigma^2}}}{\sqrt{2\pi}\sigma} + \frac{f_1}{\lambda_1}e^{-\frac{\lambda_{corr}}{\lambda_1}}; \quad for \;\; \lambda_{corr} \geq 0 \qquad (43)$$

$$g_{bkg}(\lambda_{corr}) = (1 - f_1 - f_2)\frac{e^{-\frac{\lambda_{corr}^2}{2\sigma^2}}}{\sqrt{2\pi}\sigma} + \frac{f_2}{\lambda_2}e^{\frac{\lambda_{corr}}{\lambda_2}}; \quad for \;\; \lambda_{corr} < 0$$

where the fit parameters are:

f_1	:	is the fraction of right side exponential
λ_1	:	is the slope of right side exponential
f_2	:	is the fraction of left side exponential
λ_2	:	is the slope of left side exponential
σ	:	is the width of the gaussian

3.6.2 Signal Distribution

The 'pseudo'-$c\tau$ distribution for the signal region, which is defined as $\pm$ 50 MeV/c^2 around the J/ψ-mass, consists of three components: a gaussian distribution for the prompt J/ψ's, the background as described in the previous section, and finally the J/ψ's from b-decay which are described by an exponential convoluted with a gaussian resolution function:

$$f(\lambda_{corr}) = f_{bkg} g_{bkg}(\lambda_{corr}) + (1 - f_{bkg}) \cdot [(1 - f_B) \cdot G + f_B \cdot G * E] \quad (44)$$

where:

f_{bkg}	:	is the background fraction
$g_{bkg}(\lambda_{corr})$	:	is the normalized background distribution
f_B	:	is the fraction of J/ψ from B decay
σ	:	is the error on λ_{corr}
$c\tau$	:	is the proper decay length of B mesons

The normalized G and E distributions have the following explicit form:

$$G(y) = \frac{1}{\sqrt{2\pi}\sigma} \cdot exp(-y^2/2\sigma^2) \quad (45)$$

$$E(x) = \frac{1}{c\tau} \cdot exp(-x/c\tau)\, for\, x > 0 \quad (46)$$

and the convolution is defined as:

$$G * E_{(\lambda_{corr})} = \frac{1}{\sqrt{2\pi}\sigma c\tau} \int_{-\infty}^{\lambda_{corr}} exp\left\{-(\lambda_{corr} - y)/c\tau\right\} exp\left\{-y^2/2\sigma^2\right\} dy \quad (47)$$

The exponent in this equation can be rewritten as:

$$-\frac{1}{2\sigma^2 c\tau}\left[2\sigma^2(\lambda_{corr} - y) + c\tau y^2\right]$$

$$= -\frac{1}{2\sigma^2 c\tau}\left[2\sigma^2\lambda_{corr} - 2\sigma^2 y + c\tau y^2 + \frac{\sigma^4}{c\tau} - \frac{\sigma^4}{c\tau}\right]$$

$$= -\frac{\lambda_{corr}}{c\tau} + \frac{\sigma^2}{2(c\tau)^2} - \frac{1}{2\sigma^2} \cdot \left(y - \frac{\sigma^2}{c\tau} \right)^2$$

which gives:

$$G * E_{(\lambda_{corr})} = \frac{1}{\sqrt{2\pi}\sigma c\tau} exp \left\{ \frac{\sigma^2}{2(c\tau)^2} - \frac{\lambda_{corr}}{c\tau} \right\} \cdot \int_{-\infty}^{\lambda_{corr}} exp \left\{ -\frac{1}{2} (\frac{y}{\sigma} - \frac{\sigma}{c\tau})^2 \right\} dy$$

Substituting $v = \frac{y}{\sigma} - \frac{\sigma}{c\tau}$ and $dy = \sigma dv$ results in:

$$G * E_{(\lambda_{corr})} = \frac{1}{\sqrt{2\pi}c\tau} exp \left\{ \frac{\sigma^2}{2(c\tau)^2} - \frac{\lambda_{corr}}{c\tau} \right\} \cdot \int_{-\infty}^{\frac{\lambda_{corr}}{\sigma} - \frac{\sigma}{c\tau}} exp \left\{ \frac{v^2}{2} \right\} dv$$

The function $freq$ in the CERN libraries [57] is defined as:

$$freq(x) = \frac{1}{\sqrt{2\pi}} \cdot \int_{-\infty}^{x} exp(-t^2/2) dt \tag{48}$$

Finally one gets the following expression for $G * E_{(\lambda_{corr})}$:

$$G * E_{(\lambda_{corr})} = \frac{1}{c\tau} \cdot exp \left\{ \frac{\sigma^2}{2(c\tau)^2} - \frac{\lambda_{corr}}{c\tau} \right\} \cdot \left[1 - freq(\frac{\sigma}{c\tau} - \frac{\lambda_{corr}}{\sigma}) \right]$$

This expression has then to be substituted in equation (44).

3.6.3 Fitting Procedures

We have fitted the J/ψ lifetime using three different procedures. Fitting procedure A, an unbinned likelihood fit, is the default and will be used to determine the final lifetime results. Fitting procedure B, a binned likelihood fit, provides a check of our method. Fitting procedure C is a binned likelihood fit like B with the difference that the fit is restricted to the range where the pseudo-$c\tau$ is larger than 400 μm. So the fit is only driven by the exponential part of the pseudo-$c\tau$ distribution. For general information about fitting techniques and methods see [58],[59],[60].

Procedure A is a standard maximum likelihood fit using $f(\lambda_{corr})$ as the probability distribution function. If N is the total number of J/ψ's, i the J/ψ index and $\lambda_{corr}^{(i)}$, $\sigma^{(i)}$ the values of the pseudo $c\tau$ and its calculated error for each J/ψ, the likelihood function is defined as:

$$L = \prod_{1}^{N} f(\lambda_{corr}^{(i)}, \sigma^{(i)}; f_B, c\tau) \tag{49}$$

Then one has to minimize the corresponding log-likelihood:

$$\mathcal{L} = -2log(L) \tag{50}$$

with respect to the parameters $c\tau$ and f_B.

It is important, in this type of fit, to have a good understanding of the errors, since they are an important component of the shape of probability distribution function. In section 4.2 it will be demonstrated that the errors are in fact well understood. The minimization of the log-likelihood function was performed with MINUIT [61].

In fitting procedure B, the probability distribution function is given by the Poisson distribution of the contents of each bin, where the average per bin is estimated using the model function $f(\lambda_{corr})$, with a common σ for all events. More precisely, one defines:

$$P(\mu_i, n_i) = \frac{e^{-\mu_i}\mu_i^{n_i}}{n_i!} \tag{51}$$

where:

i	:	is the bin index
n_i	:	is the content of the i^{th} bin
$\mu_i = A \cdot f(\lambda_{corr}^{(i)}; c\tau, f_B, \sigma)$	:	is the predicted average content of the i^{th} bin
A , $c\tau$, f_B, σ	:	are the fit parameters (A is an overall normalization constant)
$\lambda_{corr}^{(i)}$	:	is the value of the center or the i^{th} bin

The likelihood function is defined as:

$$L = \prod_{1}^{N_{bins}} P(\mu_i, n_i) \tag{52}$$

and the related log-likelihood function as defined in the previous case has to be minimized. The minimization was performed with MINUIT within the context of PAW [62], using the L (likelihood) option.

4 Data Selection

This section describes the data sample used in the analysis. The cuts applied to get a clean sample are listed. In addition, the method used to optimize the track quality cuts is described.

We begin with a dimuon sample obtained from Express PSIX_2P and PSIX_1P PADs. PAD is a condensed data format which is used within CDF. The data was selected by the central dimuon trigger which required two muon stubs found in the CMUO chambers at Level 1. At least one of the muons had to pass the CFT requirement at Level 2. These data were reconstructed with Version 6.01 of the offline package. The central tracking chamber was not fully calibrated at that time, meaning that the error of the track parameters as returned by the CTC-fit was underestimated. To take this into account and to make sure that the SVX χ^2 which is not completely decoupled from the CTC fit behaves properly we rescale the CTC covariance matrix by a factor of 2.5 using it in the SVX fit as described in section 2.8.2. How this factor of 2.5 was determined is described in [63]. At the moment of writing this thesis (April 1993) the data resided in the CDF disk labeled:

FNALKD$STRIP1:[BOTTOM10.PSIX_P]

(or 8mm tapes CC8294 and CC8302)

We limited our analysis to Runs 40100-43670, recorded before the shutdown in January 1993. The total integrated luminosity of this dataset is reported by LUMSUM to be 10.1 pb^{-1}.

We limited ourselves to muons recorded in the CMU or CMP detectors. The muon selection cuts used in this analysis (see [64]) are listed below. (i-iii) are P_t dependent muon matching cuts where the distance between the track in the muon chambers and the extrapolated CTC-track is calculated in the transverse plane (for CMU type muons also in the longitudinal plane). The difference was required to be less than 3 standard deviations from 0 where one standard deviation is the quadratic sum of multiple scattering and measurement errors.

i . MOXFTM $< 9 \rightarrow p_t$ dependent CMU x matching

ii . MOZFTM $< 9 \rightarrow p_t$ dependent CMU z matching

iii. MOXFTP $< 9 \rightarrow p_t$ dependent CMP x matching

v . MOCHAE > 0.5 GeV $\rightarrow$ associated hadronic energy

vi . at least one μ with $P_t > 2.5$ GeV/c

In addition, the following track/vertex selection cuts were applied:

i . SVXA: both muon legs reconstructed in the SVX

ii . TCUT: SVX $\chi^2 < 20$ for both μ's

iii. VCUT: χ^2 of the 2 μ vertex fit < 12

iv . ECUT: calculated error on the transverse decay length $\sigma_{L_{xy}} < 150$ μm

v . PCUT: beam position available in the data base

vi . RCUT: all SVX residuals less then 4 σ

vii. SCUT: no shared clusters with other tracks reconstructed in the SVX

viii. CCUT: no clusters with total charge > 400 ADC counts (which is about 4 times the amount deposited by a minimum ionizing particle)

The procedure used to determine these cuts is described in section 4.1. The effect of these cuts on the size of the dataset is summarized in Table 8. Figure 38 shows the invariant mass spectrum of the selected dimuon events after all cuts. There are 5667 events in the J/ψ mass region (defined to be a window of $\pm 50 MeV$ around the J/ψ mass):

$$3.047 < M_{\mu\mu} < 3.147 \ (GeV/c^2)$$

With this window, the background under the peak is 5.7%. We have studied the behavior of this background using dimuon events in the sidebands, defined to be the mass ranges:

$$2.9 < M_{\mu\mu} < 3.0 \ \ and \ \ 3.2 < M_{\mu\mu} < 3.3 \ (GeV/c^2)$$

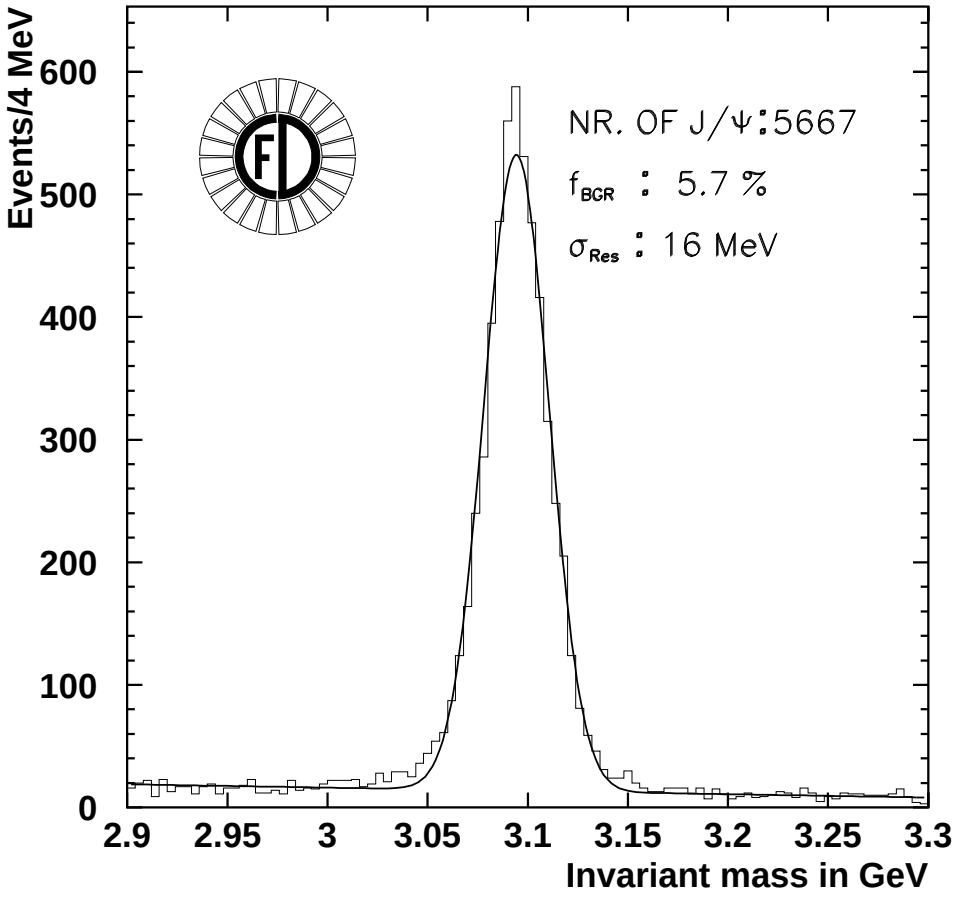

Figure 38: *Invariant mass distribution of oppositely charged dimuons.*

list of cuts (in all cases both muons were required to be reconstructed in the SVX (SVXA))	$N_{J/\psi}$	N_{bkg}	% bckg
MUCUT	11225	807	7.2
MUCUT/TCUT	10474	682	6.5
MUCUT/TCUT/VCUT	10449	671	6.4
MUCUT/TCUT/VCUT/ECUT	9945	632	6.4
MUCUT/TCUT/VCUT/ECUT/PCUT	9907	628	6.3
MUCUT/TCUT/VCUT/ECUT/PCUT/RCUT	6750	398	5.9
MUCUT/TCUT/VCUT/ECUT/PCUT/RCUT/SCUT	6208	352	5.7
MUCUT/TCUT/VCUT/ECUT/PCUT/RCUT/SCUT/CCUT	5667	323	5.7

Table 8: *Number of events in* J/ψ*-mass region after each cut.*

4.1 Optimizing the Track Quality Cuts

Since we have such a large sample of J/ψ events, our measurement will be dominated by systematic rather than statistical uncertainties. In order to reduce the size of the systematic error we have applied strict track quality cuts to remove non-gaussian tails from the resolution function. This section describes how the track quality cuts have been determined.

In optimizing our cuts, we have found it useful to study the distribution of the signed impact parameter of the two J/ψ legs. The 'signed' impact parameter (D_A^S) of the J/ψ leg A is defined as follows:

$$D_A^S = |D_A| \cdot \frac{D_A \cdot (-P_y^A P_x^\psi + P_x^A P_y^\psi)}{|D_A \cdot (-P_y^A P_x^\psi + P_x^A P_y^\psi)|} \tag{53}$$

Here D_A is the distance of closest approach of leg A to the primary vertex, $\vec{P^A}$ is the momentum of leg A and $\vec{P^\psi}$ is the momentum of the J/ψ. Thus the sign of D_A is positive for the 'likely' case where the J/ψ decay distance is in the direction of motion of the J/ψ. When plotting the signed impact parameter of one J/ψ leg (D_A^S) as a function of the signed impact parameter of the other (D_B^S), one expects the following:

- prompt J/ψ's concentrate at $D_A^S = D_B^S = 0$. One expects a 2 dimensional gaussian distribution.
- J/ψ from b-decay should be found in the quadrant where both signed impact parameters are positive. This expected behavior has been verified using Monte Carlo events.

Figure 39 shows the signed impact parameter of leg A plotted versus the impact parameter of leg B before the track quality cuts (RCUT, SCUT, CCUT) have been applied.

We notice that events with large negative impact parameter (and which contribute to the negative tails of the pseudo $c\tau$ distribution) are concentrated in a 'peculiar' configuration; they appear on the two axes of the coordinate system. This observation implies the following interpretation of these events: they come from the combination of one well-measured track, which most likely originates from the primary vertex and has an impact parameter close to 0, while the other track is badly measured and has an impact parameter which is 'artificially' different from 0.

We clearly cannot cut on this impact parameter distribution since such a cut could bias the lifetime distribution. We choose instead to use these tails to monitor the fraction of badly measured tracks in the sample. In other words the best set of track quality cuts is the set which gives the best signal-to-background ratio, where the background is defined as the number of events in the 'peculiar' region. The most efficient way to remove poorly measured tracks is to require that none of the residuals of the fit be larger than 4 standard deviations. The standard deviation of the residual distributions is 10 μm at layer 0 and 12 μm at layers 1,2 and 3. Figure 40 shows the residual distribution for three and four hit tracks before RCUT, SCUT and CCUT. A gaussian fit to the distribution is superimposed. One observes significant non-gaussian tails.

In addition, we have removed tracks sharing one or more clusters with another track reconstructed in the SVX, and have removed events where any cluster has more than 400 ADC counts. These requirements improve the signal to background ratio by more than a factor of 6. Additional quality cuts, such as removing clusters with more than 4 strips, excluding clusters which had dead strips or cutting harder on the χ^2 of the SVX fit, are far less efficient at removing background. Figure 41 shows the scatter plot of leg A versus leg B after quality cuts. One can see that most events on the coordinate axis have disappeared.

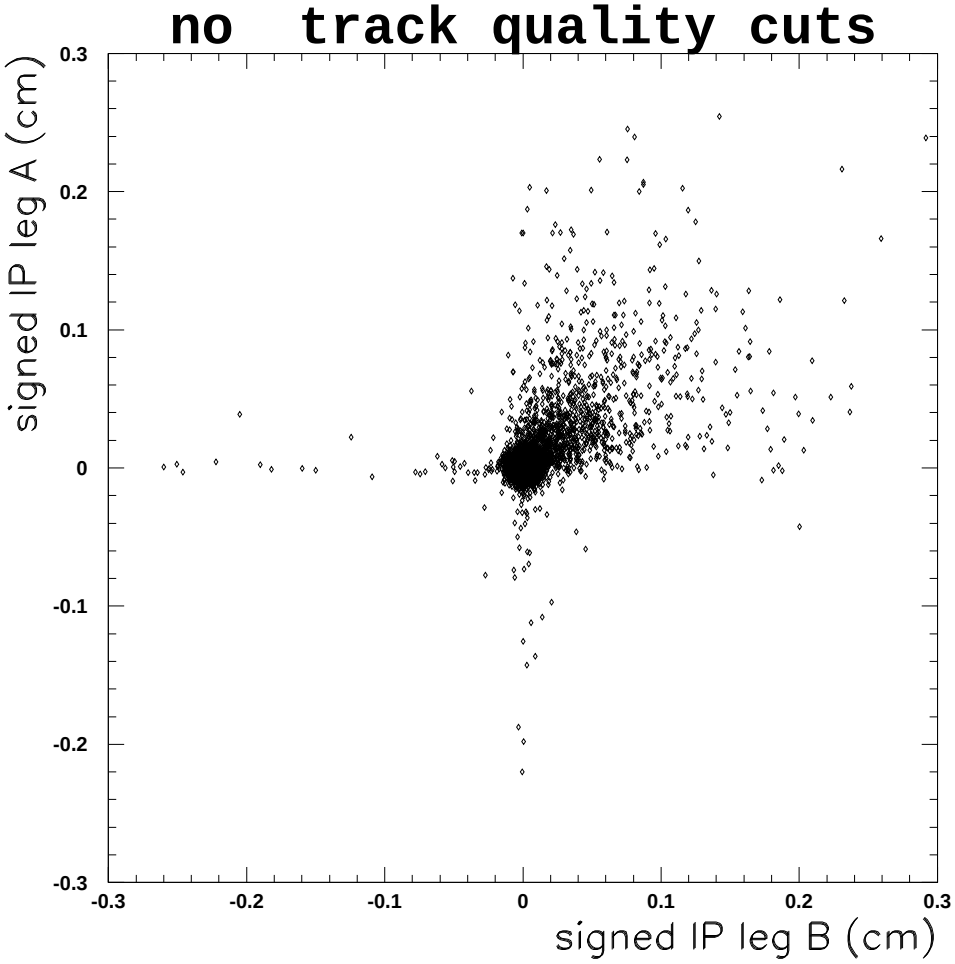

Figure 39: *Signed impact parameter of the two* J/ψ*-legs before track quality cuts.*

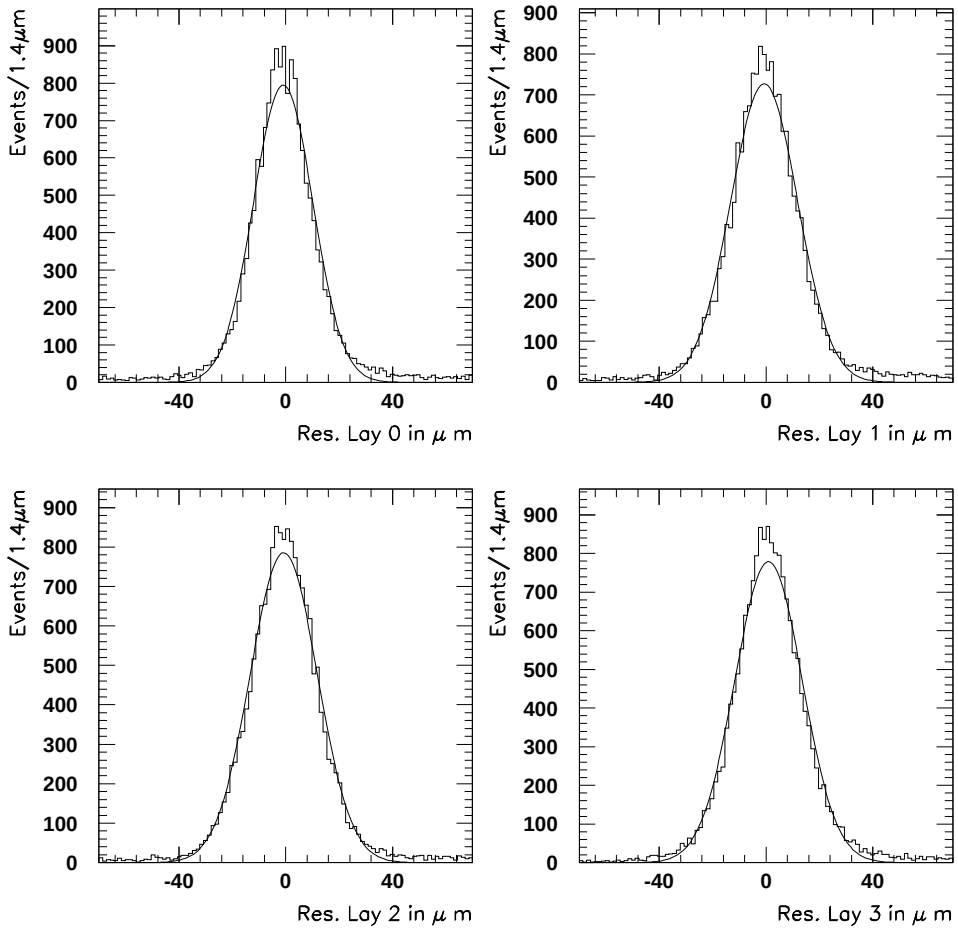

Figure 40: *Residual distributions of the two* J/ψ*-legs before track quality cuts for the four SVX layers.*

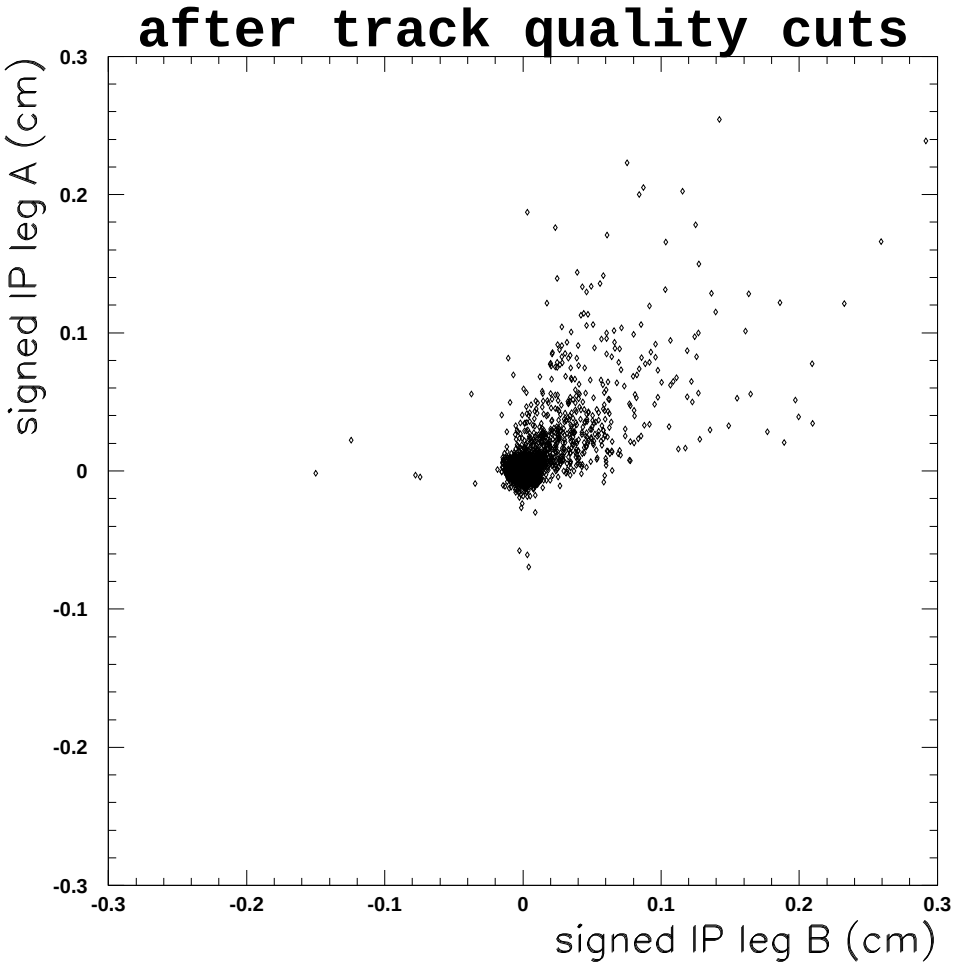

Figure 41: *Signed impact parameter of the two* J/ψ*-legs after track quality cuts.*

4.2 The L_{xy} Resolution

We have determined the L_{xy} resolution and verified that this resolution function is symmetric by studying a number of control samples.

The following direct measurements of the L_{xy} distribution have been made:

- L_{xy} distribution of prompt $\Upsilon(1s)$ events have been examined.
- The resolution of the prompt part of the J/ψ distribution has been measured.
- A sample of 'fake' J/ψ's has been constructed from oppositely charged tracks in events from jet triggers where the invariant mass of this two tracks falls accidentally into the J/ψ- mass region.

In addition, a number of indirect tests have been performed:

- The impact parameter distribution of electrons from $W \to e\nu$ events with respect to the fitted beamline, where the electrons have a $P_t > 21\ GeV/c$ was plotted. One observes that the IP distribution is centered at 0 with a σ of 38 μm which is consistent with the beamprofile. This analysis is described in [65].
- 'High P_t' muons from prompt $Z^0 \to \mu^+\mu^-$ decays, where the muons are basically back-to-back, provide another probe to check the alignment and the intrinsic resolution of the SVX detector. Here one uses the sum of the impact parameters of the two muons to measure the resolution function. A gaussian fit through this distribution gives a sigma of 23 μm from which one can derive an asymptotic resolution for high P_t tracks of $23/\sqrt{2} = 16\mu$m. The advantage of this measurement is that it measures the intrinsic resolution of the SVX directly and one is not dominated by the spread of the beam. The results of this analysis are described in [65].

Figure 42 shows the invariant mass distribution of oppositely charged muons in the Υ(1s) region. The plot is labeled 'loose cuts' because to preserve the limited statistics the track quality cuts (RCUT, SCUT, CCUT) were not

applied. Instead to increase the signal-to-background ratio it was required that at least one of the two muons was measured in the CMP.

For a correct unbinned likelihood fit it is important that the calculated error in L_{xy} be correct. To check this, one can divide the L_{xy} by its calculated error. In case of prompt decays one expects a gaussian distribution peaked at 0 with a sigma of 1. Figure 43 shows that this is the case for dimuon events within the invariant mass window between 9.3 and 9.6 GeV/c^2.

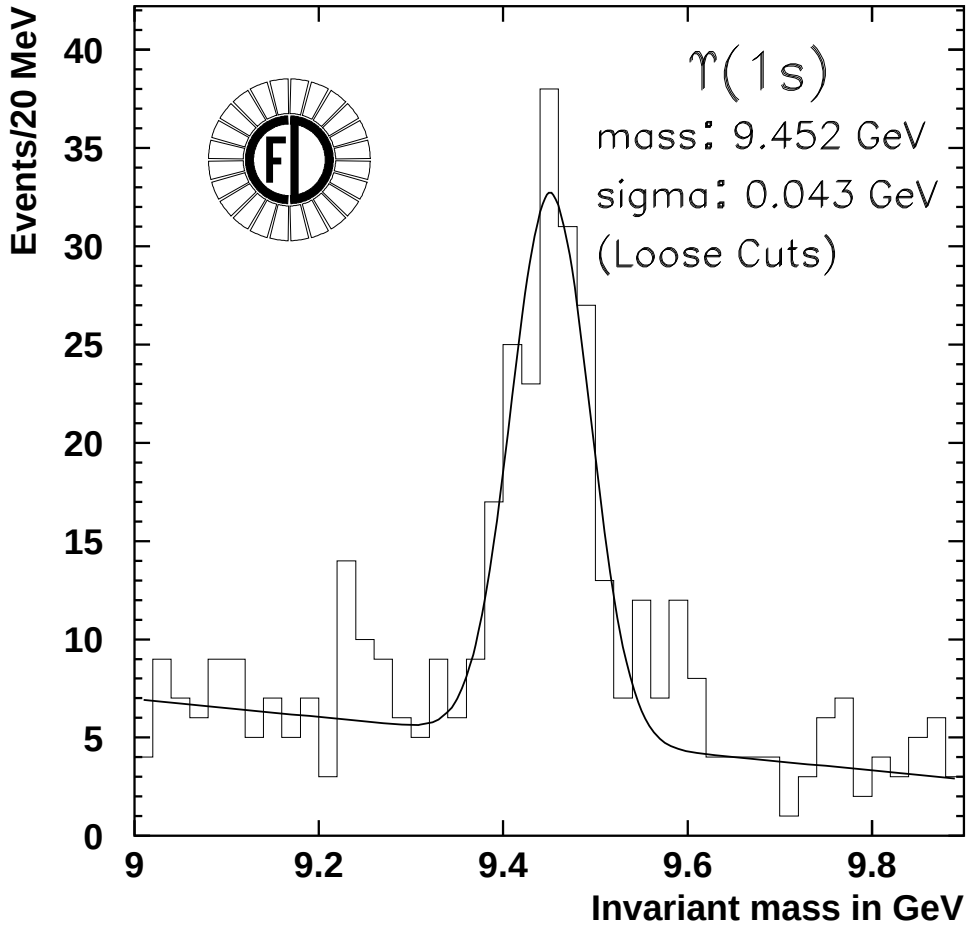

Figure 42: *Invariant mass distribution of oppositely charged dimuons in the* Υ*(1s) mass region.*

Figure 44 shows the $L_{xy}/\sigma_{L_{xy}}$ distribution for the selected J/ψ-events. A

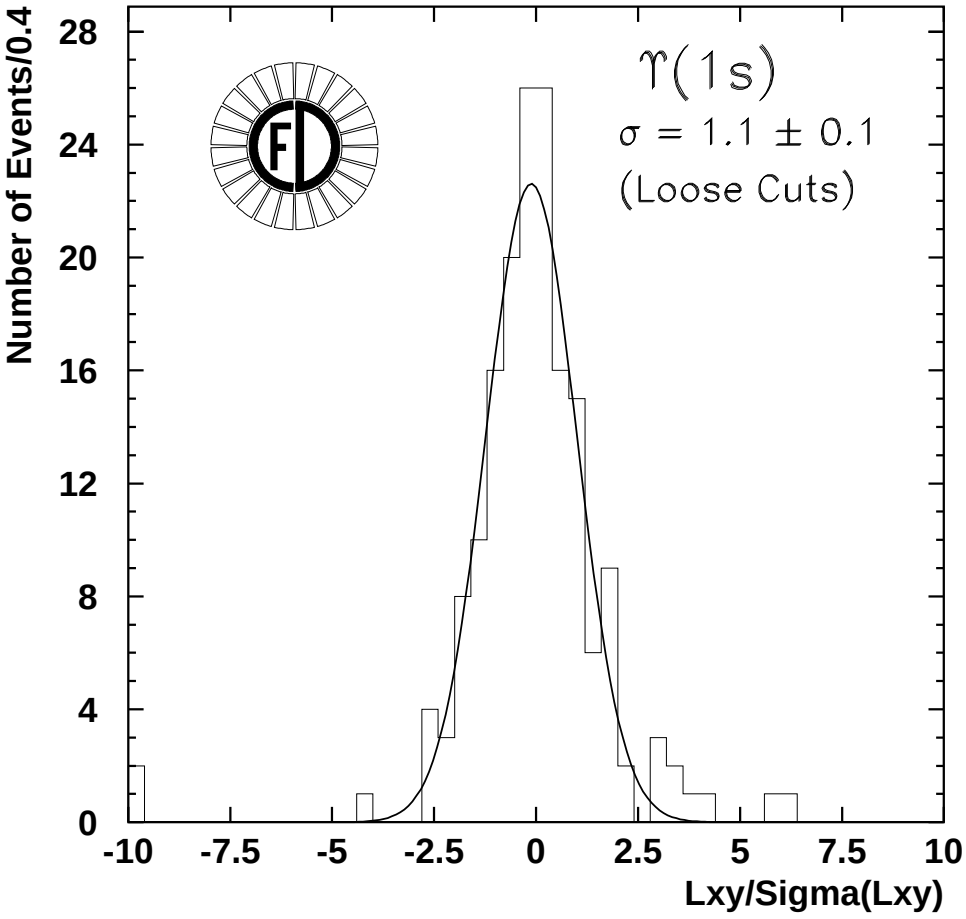

Figure 43: $L_{xy}/\sigma_{L_{xy}}$ *for dimuon events in the* Υ*(1s) mass region.*

gaussian fit through the prompt core of the distribution gives a sigma of 1.00 ± 0.01.

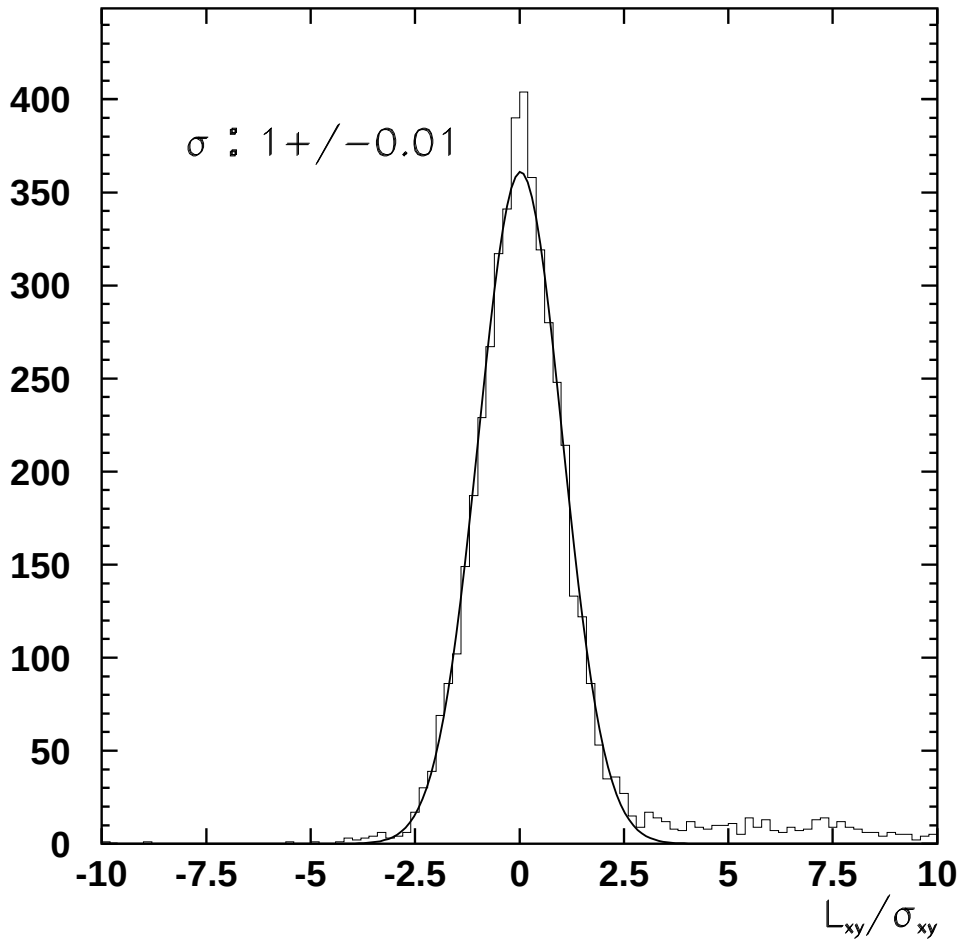

Figure 44: *$L_{xy}/\sigma_{L_{xy}}$ for dimuon events in the* J/ψ *mass region.*

The shape of the pseudo-$c\tau$ distribution for fake J/ψ's was studied using a sample extracted from QCD jet events. (The datasets used were the Version 6.01 J4Q1 ("Jet_20") and J3Q1 ("Jet_50") Pads.) First two track combinations with invariant mass within $\pm$300 MeV of the J/ψ mass were searched. In order to insure that these fake J/ψ's were in the same kinematic range as the true dimuon data, the effects of the muon trigger were modeled as follows: All tracks were required to have $|\eta| \leq 0.6$. One track was required

to have $P_t > 2.5$ GeV/c and the other track was required to have $P_t > 1.5$ GeV/c. The resulting fake J/ψ's were then required to pass the same selection criteria as the data. Figure 45 shows the pseudo $c\tau$-distribution of this fake sample. One observes that the distribution is symmetric around zero but has non-gaussian tails. The same function as for the J/ψ- sidebands was used to fit the distribution and the fit results are summarized in Table 9. The fit range was restricted to be within -0.1 to 0.1 cm. Long tails are expected to come from K^0_S decays but we haven't made any effort to remove K^0_S-candidates from the sample.

It is interesting that these non-gaussian tails on both sides have approximately the same slope as the left tail of the sideband pseudo $c\tau$ distribution (compare Table 9 with Table 10). There one would expect that part of the events are due to hadron fakes. In fact the non-gaussian tails on the left of the J/ψ pseudo $c\tau$-distribution shown in Figure 50 and 53 below are adequately described by the left tail of the sideband distribution. What these tails are due to and why they appear in the fakes but not in the background subtracted J/ψ-sample is not totally understood. One may blame this excess on the more difficult environment in Jet events which leads to more tracking errors than in J/ψ events.

Figure 46 shows the $L_{xy}/\sigma_{L_{xy}}$ for the fake J/ψ. Also for the fakes the sigma is approximately 1 and the distribution is centered at 0.

Parameter	Value	Error
σ : sigma of gaussian	37 μm	$\pm$ 0.6 μm
λ_1: slope of right side exponential	191 μm	$\pm$ 16 μm
f_1 : fraction of right side exponential	7%	$\pm$ 0.6%
λ_2: slope of left side exponential	181 μm	$\pm$ 18 μm
f_2 : fraction of left side exponential	4%	$\pm$ 0.5%

Table 9: *Result of fit through pseudo-$c\tau$ distribution of 'fake* J/ψ*'s' extracted from Jet events.*

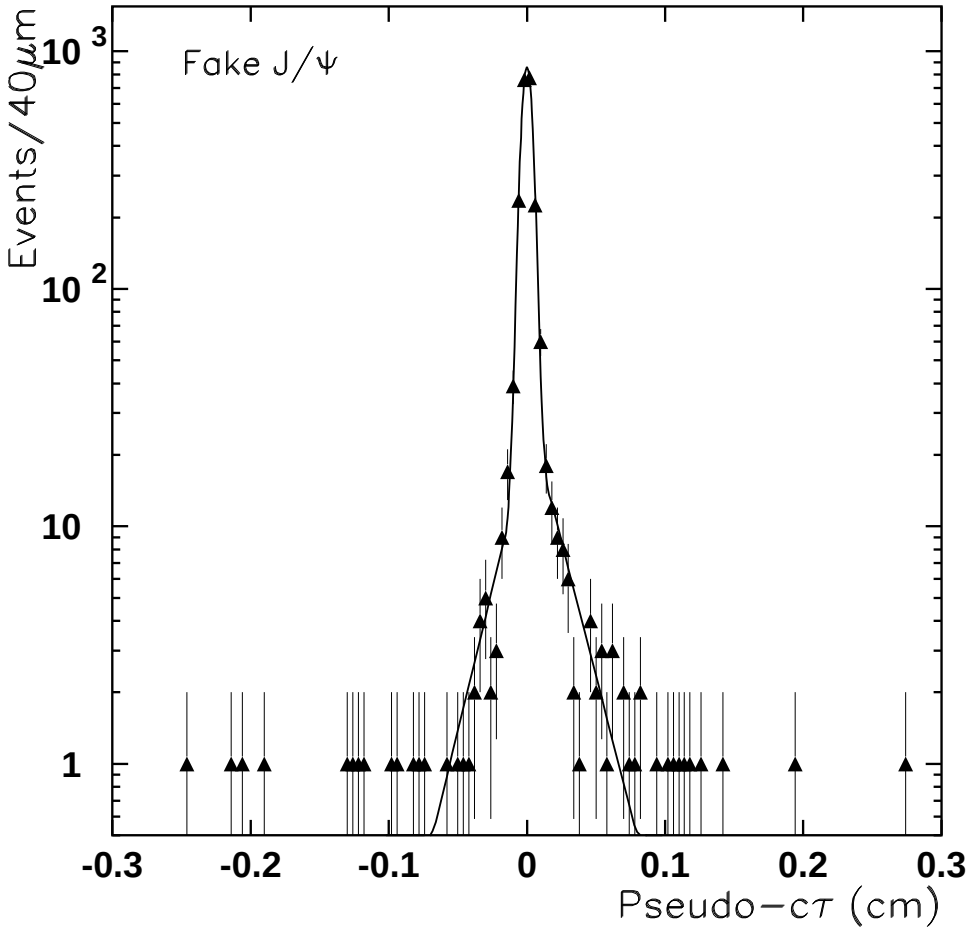

Figure 45: *Pseudo-$c\tau$ distribution of 'fake* J/ψ*'s' extracted from Jet events.*

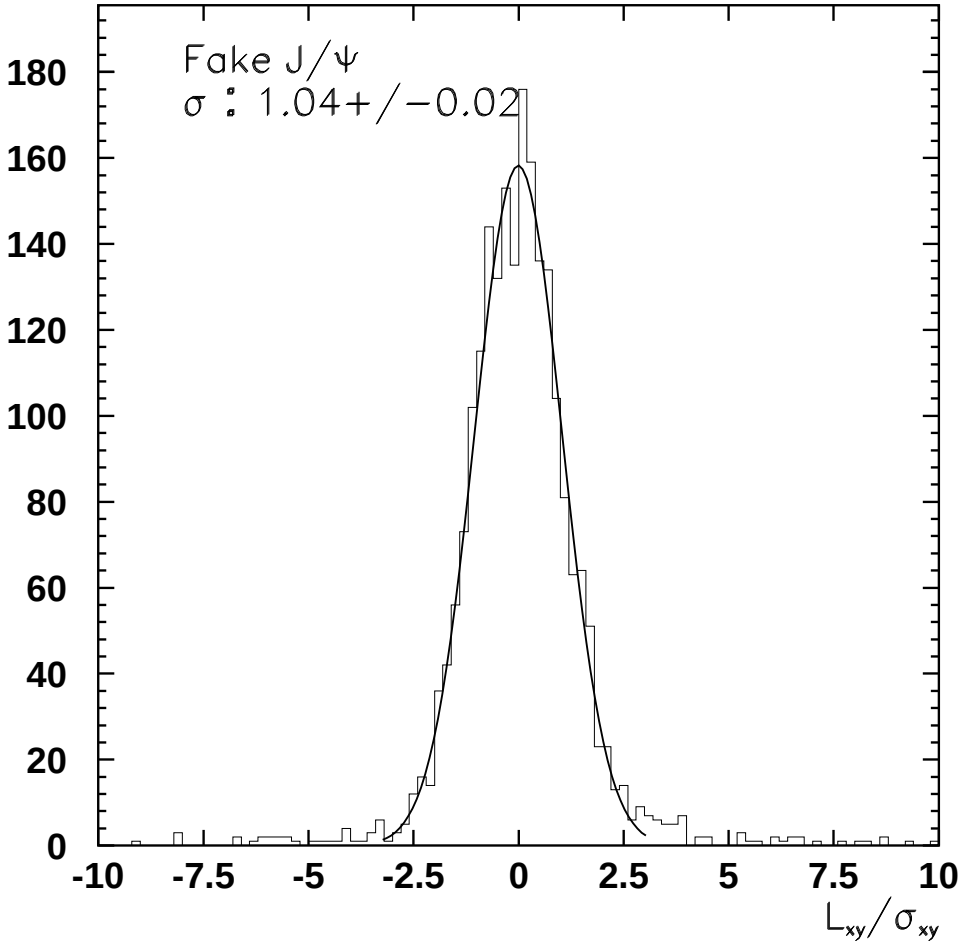

Figure 46: *$L_{xy}/\sigma_{L_{xy}}$-distribution of 'fake* J/ψ*'s'.*

Figure 47 shows the distribution of the calculated error in L_{xy}. An important precondition to allow a binned fit, where a constant error in pseudo-$c\tau$ is assumed, is that the errors don't vary too much. This is not our case, as one can see in Figure 47. Figure 48 demonstrates that there is no correlation between the error in L_{xy} and its magnitude.

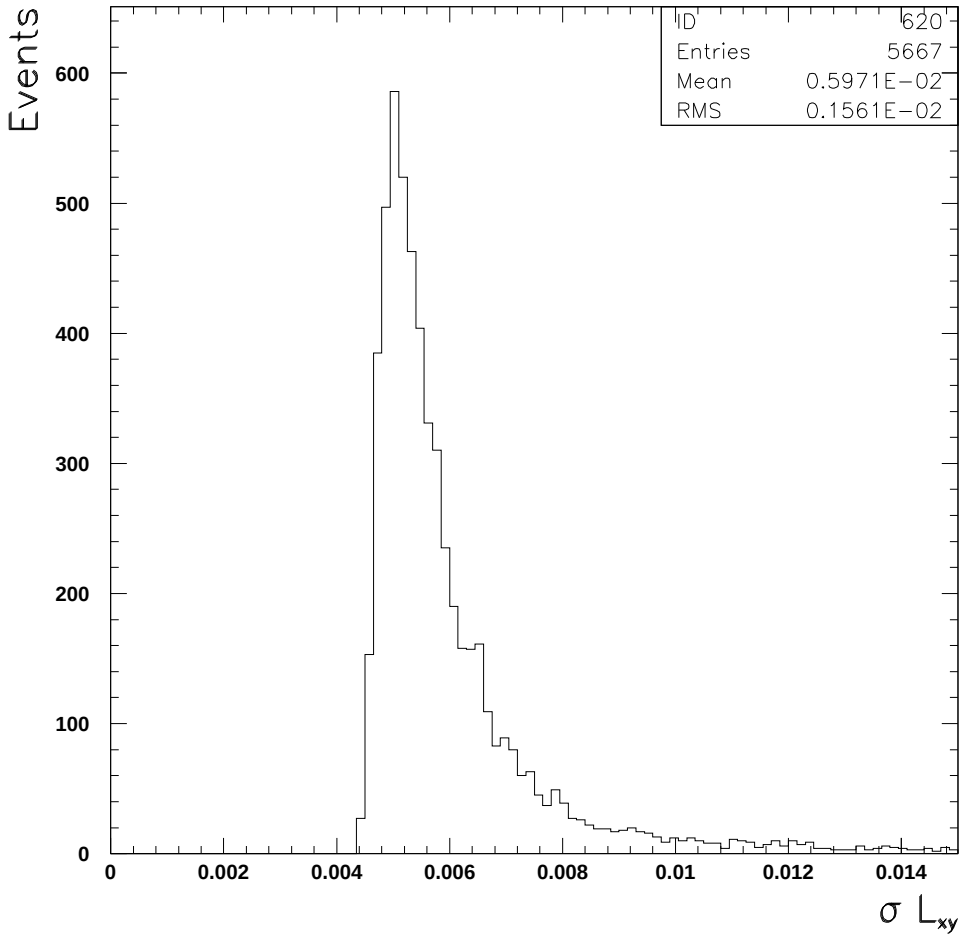

Figure 47: $\sigma_{L_{xy}}$*-distribution of* J/ψ*'s.*

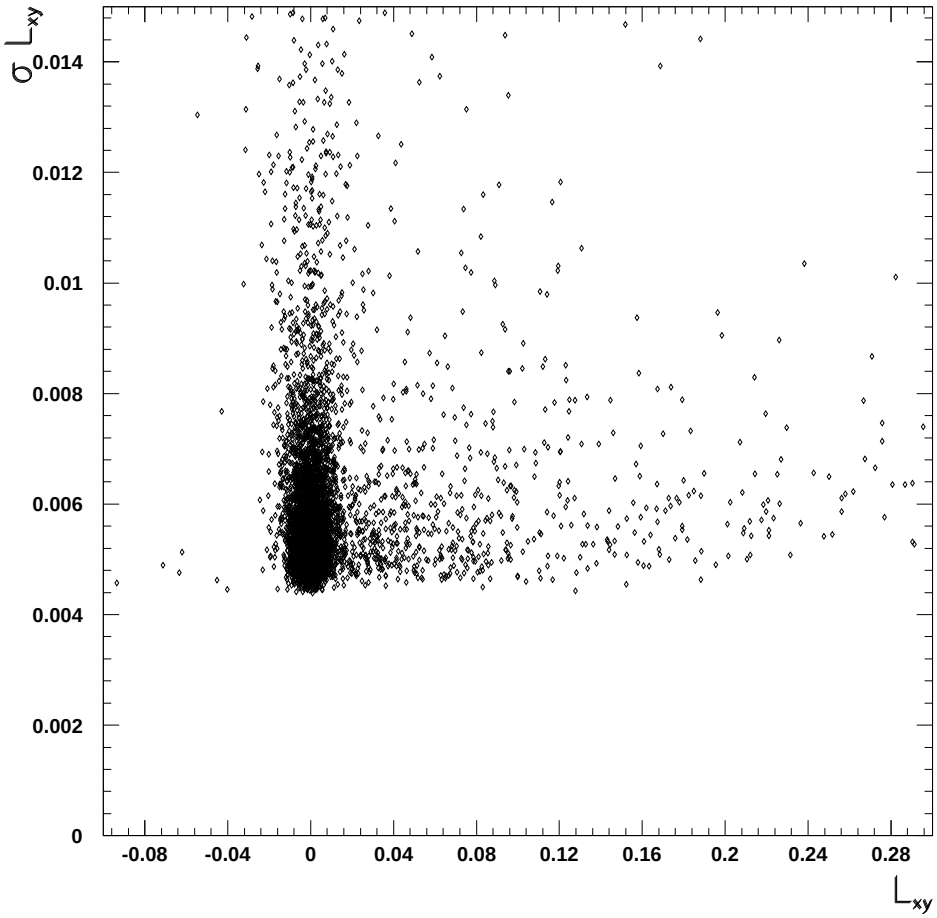

Figure 48: *L_{xy} versus $\sigma_{L_{xy}}$-Distribution of* J/ψ*'s.*

Finally one can draw the following conclusions:

- The resolution function is symmetric and centered at 0. There is no bias on the lifetime measurement due to an asymmetric shape of the resolution function.
- Various plots of the type $L_{xy}/\sigma_{L_{xy}}$ show that the error on the transverse decay length is computed adequately, which is an important precondition for using this error in an unbinned likelihood fit.

5 Results

In this section the results of the different fits through signal and background distributions are presented. Figure 49 shows the pseudo-$c\tau$ distribution for the sidebands with the fit as described in section 3.6.1 superimposed. Table 10 summarizes the result of the fit. As expected the distribution is asymmetric since some of the events are due to sequential b-decays. The shape of the left side is very similar to what is observed for the fake J/ψ's (see Table 9).

Parameter	Value	Error
σ : sigma of gaussian	49 μm	$\pm$ 2 μm
λ_1: slope of right side exponential	386 μm	$\pm$ 26 μm
f_1 : fraction of right side exponential	24%	$\pm$ 1.6%
λ_2: slope of left side exponential	209 μm	$\pm$ 25 μm
f_2 : fraction of left side exponential	11%	$\pm$ 1%

Table 10: *Parameters of fit to sideband events.*

Figures 50 and 53 show the pseudo-$c\tau$ distribution for the signal region with the fits superimposed. The dark shaded area shows the contribution from background where the shape has been derived from the sidebands, and the magnitude has been derived by normalizing the sidebands to the same area in invariant mass as used for the signal. The light shaded region shows the contribution one gets when adding the exponential distribution from b-decay convoluted with a gaussian resolution function to the background. What's left is the unshaded region which shows the contribution from prompt J/ψ. Figure 52 shows the result of a fit through the exponential tail for pseudo-$c\tau > 400\mu$m. Table 11 compares the results of the three different fit types. We see that the results of the different fits are in good agreement. Note the fit parameter f_B is not an unbiased measurement of the b-fraction in our sample. The strict track selection cuts applied to the sample favor isolated events and so decrease the fraction of J/ψ from b-decay in our sample.

Figures 51 and 54 show the difference: (fitvalue at center of the bin - number of entries)/error. The calculated χ^2 per degree of freedom is 0.9 for the binned fit.

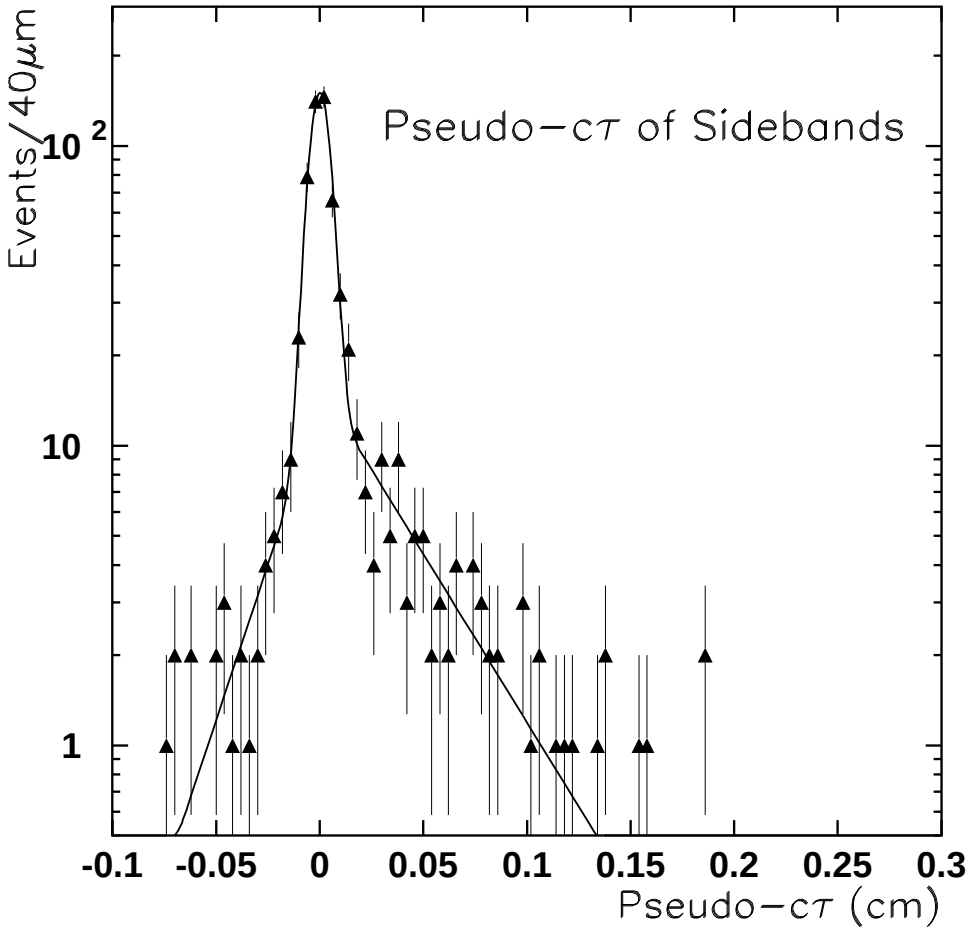

Figure 49: *Pseudo-$c\tau$ distribution of sidebands.*

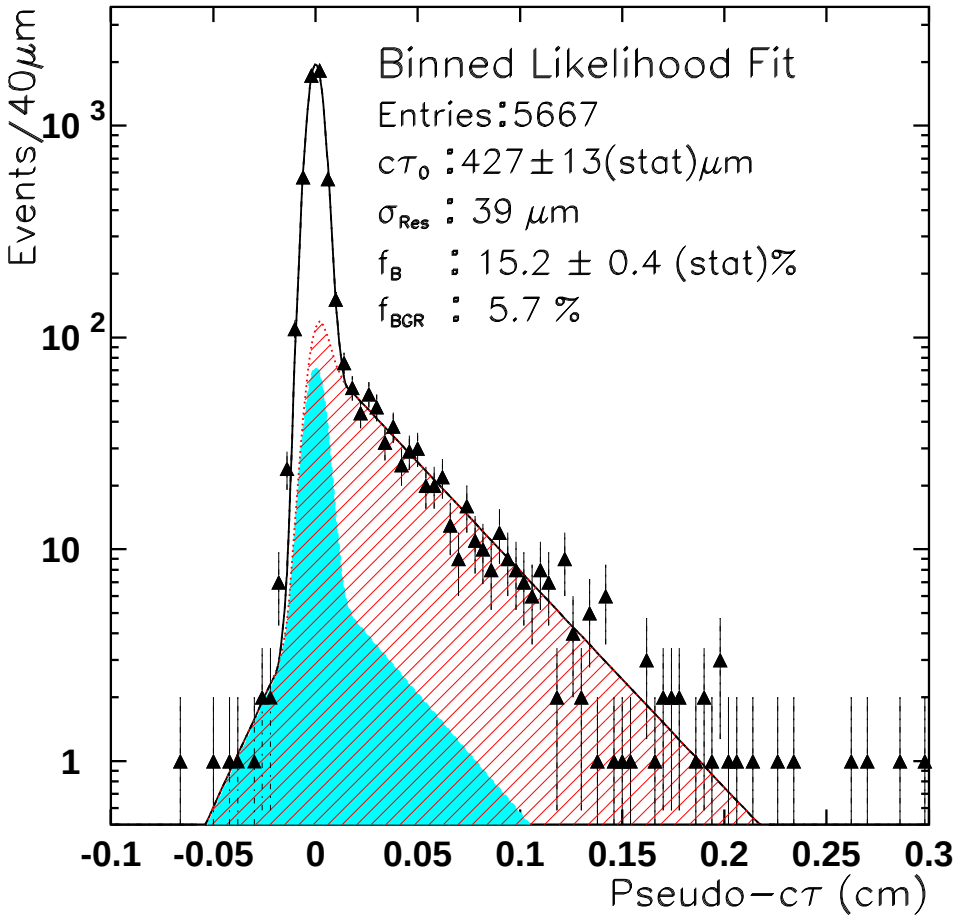

Figure 50: *Pseudo-$c\tau$ distribution of signal region with binned likelihood fit superimposed.*

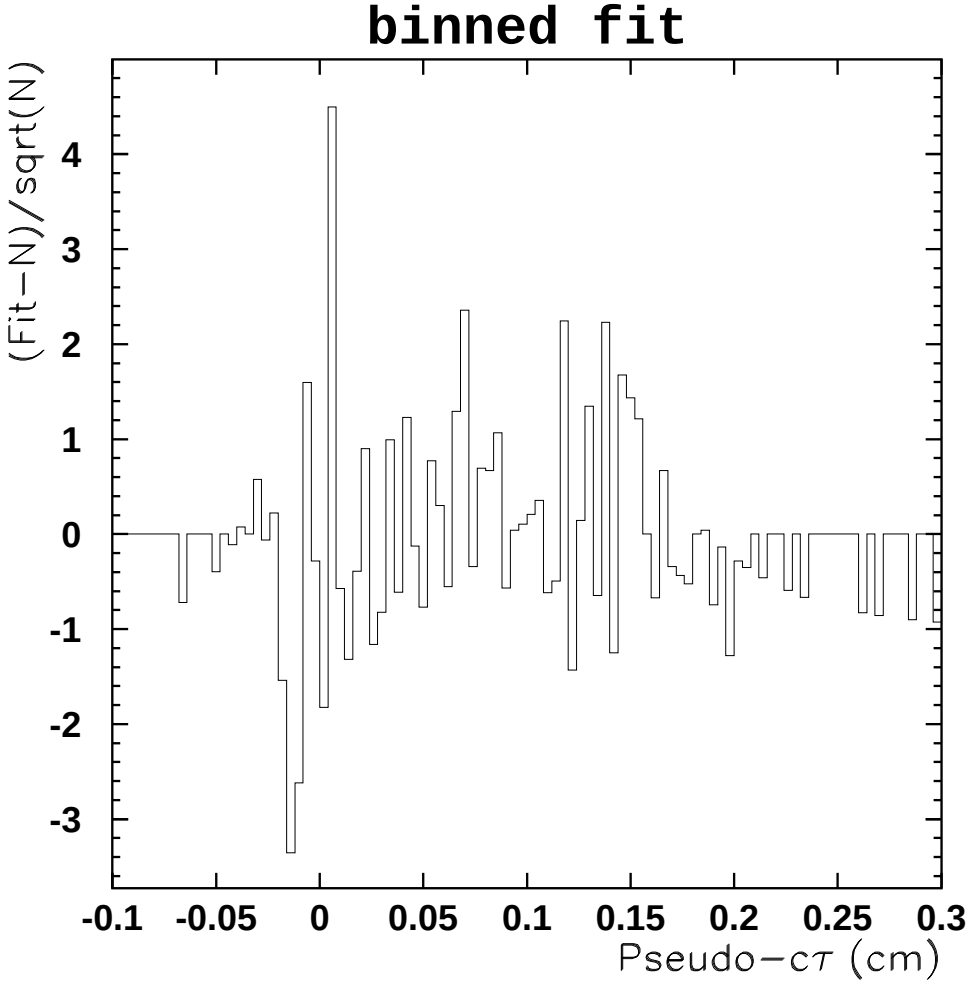

Figure 51: *Difference between the fit and the data divided by the error for the binned fit.*

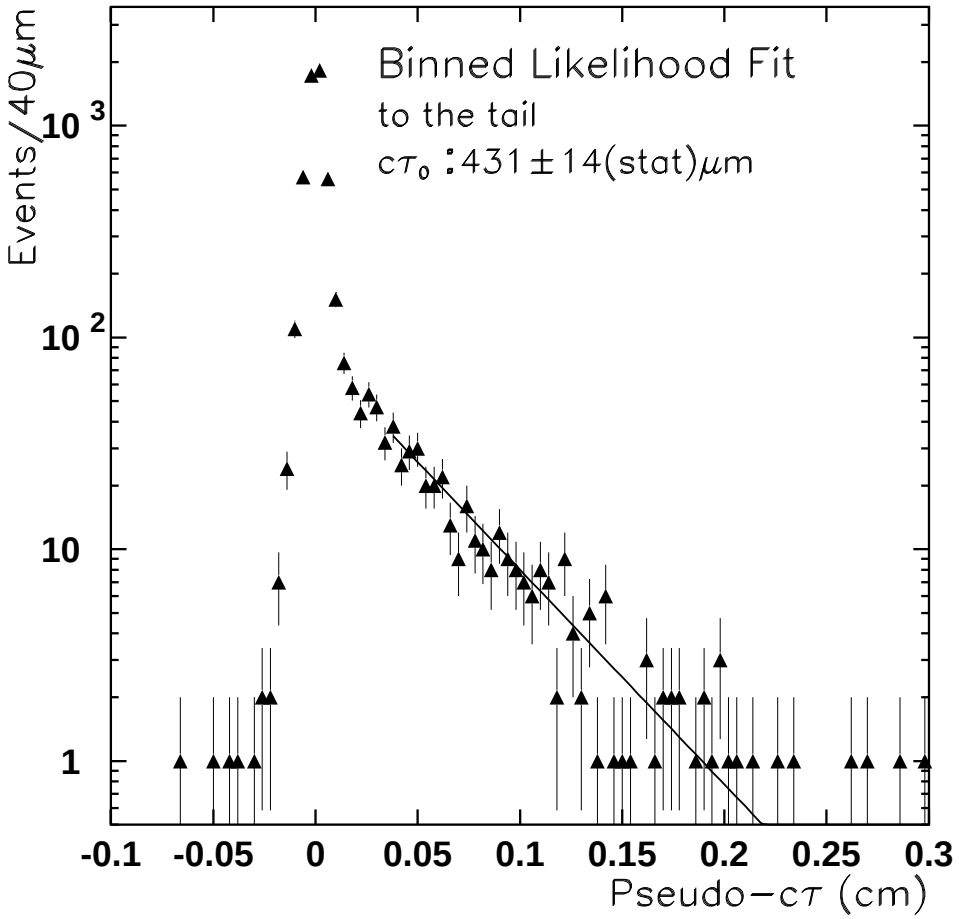

Figure 52: *Pseudo-$c\tau$ distribution of signal region with binned likelihood fit to the tail superimposed.*

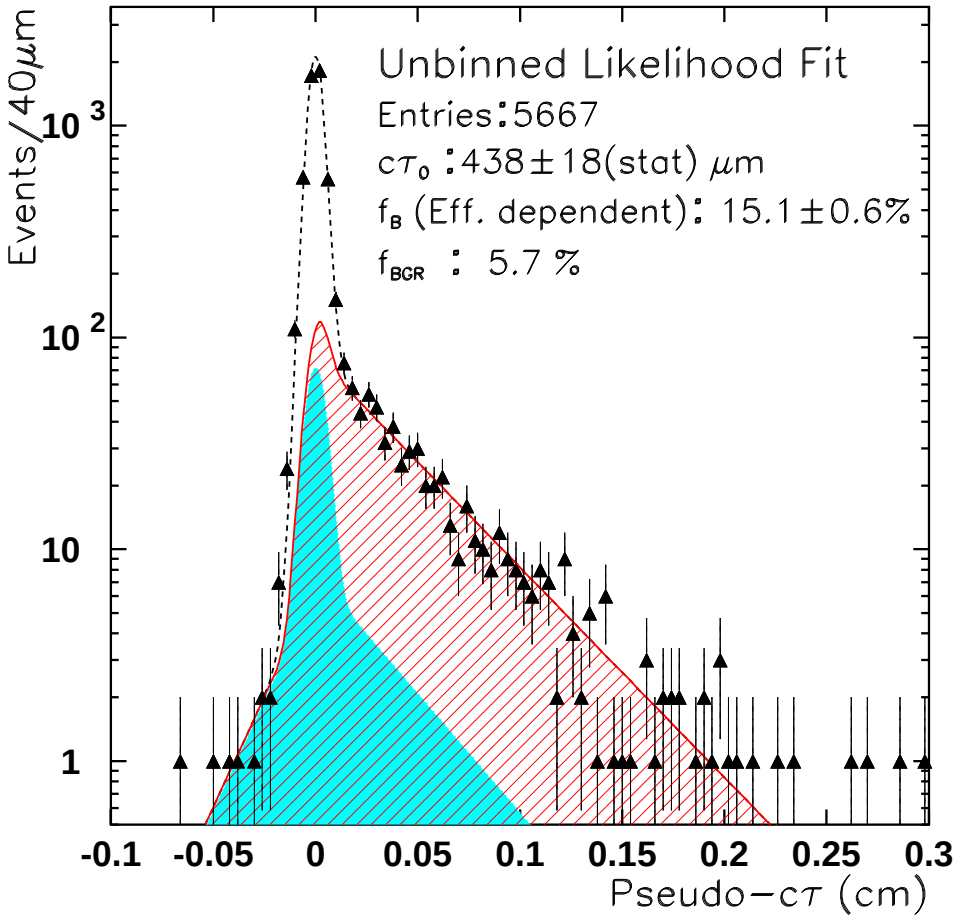

Figure 53: *Pseudo-$c\tau$ distribution of signal region with unbinned likelihood fit superimposed.*

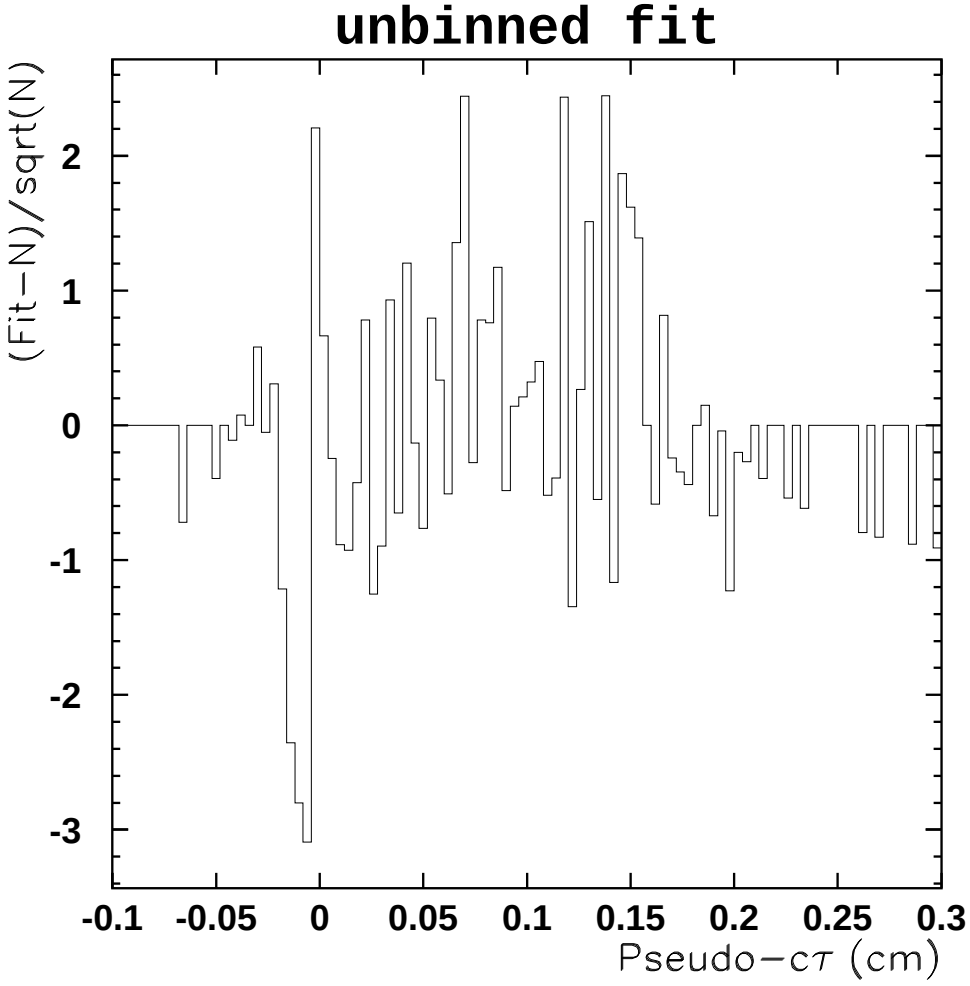

Figure 54: *Difference between the fit and the data divided by the error for the unbinned fit.*

Fittype	$c\tau_0$ in μm	f_B in %	σ_{res} in μm
A: Unbinned Likelihood	438 ± 18	15.1 ± 0.6	-
B: Binned Likelihood	427 ± 13	15.2 ± 0.4	39
C: Binned Likelihood (tail)	431 ± 14	-	-

Table 11: *Comparison of results obtained with the three different fit types.*

5.1 Stability of the Result

In this section we examine the stability of the result when the cuts on the J/ψ-momentum or the fit range are varied. Figure 55 and Table 12 summarize the results of the binned Likelihood fit for different J/ψ P_t-thresholds. The first point on the left in the plot is the result when no off-line P_t cut is applied to the J/ψ. The checks performed in this chapter were performed using a previous set for F_{corr} so that the lifetime results are a little bit higher than the values we find in the previous section. We note that f_B increases as the P_t threshold is raised. This behavior is expected since the direct J/ψ-momentum spectrum falls steeper than the spectrum of J/ψ from b-decay.

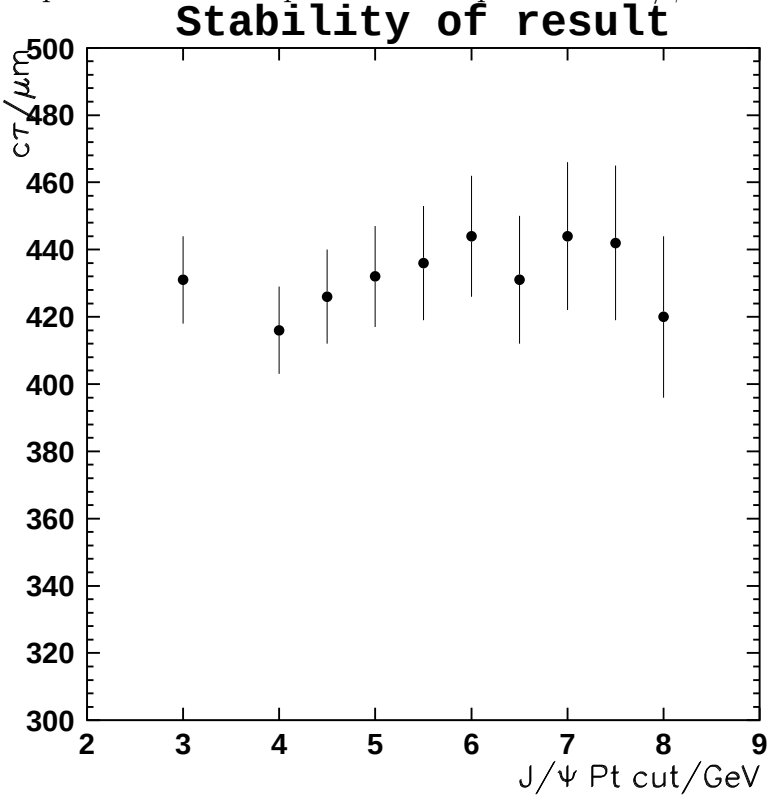

Figure 55: *$c\tau_0$ as a function of the P_t-cut on the J/ψ (errors are statistical only).*

Table 13 shows how the result of the binned likelihood fit varies when the

P_t Threshold in GeV/c	$c\tau_0$ in μm	f_B in %	Nr. of Events
no	431 ± 13	15.1	5667
4.0	416 ± 13	16.1	4743
4.5	426 ± 14	16.95	3984
5.0	432 ± 15	17.9	3292
5.5	436 ± 17	18.7	2674
6.0	444 ± 18	20.2	2123
6.5	431 ± 19	21.7	1857
7.0	444 ± 22	23.4	1307
7.5	442 ± 23	24.3	1053
8.0	420 ± 24	25.5	839

Table 12: *Result of binned likelihood fit for different P_t- thresholds.*

endpoint of the fit is changed. [2]

end of fit range in cm	$c\tau_0$ in μm
0.3	431 ± 13
0.28	429 ± 13
0.26	420 ± 13
0.24	424 ± 13
0.22	427 ± 13
0.20	420 ± 14

Table 13: *Results of binned likelihood fit for different end points.*

[2]Note this is not exactly the right thing to do since by restricting the fit range the fit function is not correctly normalized anymore.

6 Systematic Errors

In this chapter all known sources of systematic errors are described and their magnitude is estimated.

6.1 Production and Decay Kinematics

As already explained to obtain the correction factor F_{corr} one depends on Monte Carlo simulation. The different parameters and models entering this procedure were described in section 3.2.

To explore the systematics due to model dependence the following parameters were varied:

- Two different b-quark momentum spectra were used in comparison: a power law and the theoretical prediction by NDE.
- The Peterson fragmentation parameter ϵ was varied between: $\epsilon = 0.006 \pm 0.002$.
- For the J/ψ momentum spectrum the latest experimental spectra by ARGUS and CLEO were used as a comparison.
- The latest ARGUS and CLEO results were used to set the limits for the J/ψ polarization.

Overall these studies resulted in a systematic uncertainty due to model dependence of 3 %. The largest contributions come from the uncertainties on the b-quark momentum spectrum, the J/ψ momentum spectrum in the B rest frame and on the J/ψ-polarization. Varying of the fragmentation parameter within reasonable limits gives only a variation of $c\tau$ of less than 0.4%. The systematic uncertainty associated with modeling the decay of b-baryons and higher mass b-mesons has been studied using Monte Carlo calculations and gives only a small contribution to the systematic error (0.15%).

6.2 Uncertainty in $c\tau$ Resolution

In an unbinned fit the error is an important component of the shape of the probability function. It is therefore necessary to understand the errors. To

explore the systematics due to uncertainties in the error scale a scale factor R for the pseudo-$c\tau$ error has been introduced as an additional fit parameter for the unbinned fit. The result of the fit is a scale factor of 0.95. The value for $c\tau$ changes by 1.6% from 445 to 438 μm. Therefore an error of 1.6 % is assigned for the uncertainty of the error scale.

6.3 Trigger Bias

As previously described at least one muon has to pass the CFT trigger on Level 2. If the CFT trigger efficiency varies with the magnitude of the track impact parameter, the λ_{corr} distribution would be deformed and the measured lifetime would be different.

We used the same sample as described in section 4 to estimate the trigger bias. To select the events it was required that both muons be found in the CMU chambers on Level 1. The dimuon invariant mass had to be in the range between 2.9 and 3.3 GeV/c^2 and the muons had to be separated either by one 5^0 wide muon tower or one muon had to be in the forward while the other was in the backward part of the CDF detector. One of the muons had to pass the L2 CFT trigger, for the second one the transverse momentum was required to be larger than 3 GeV/c to be far enough from the trigger turn-on.

The L2 CFT trigger efficiency is then defined as the number of events for which the CFT flag is set divided by the total number of selected events.

Figure 56 shows the trigger efficiency as a function of the muon track impact parameter. The impact parameter is calculated with respect to the fitted beam position.
To evaluate the effect on our analysis the 'Toy' Monte Carlo was modified to include this effect. After applying the measured efficiency curve to the μ which passed the CFT-Trigger, the true B meson cτ was plotted and then an exponential was fitted to this 'deformed' distribution. The slope of the efficiency corrected distribution is 1.4% lower than the original. We decide to assign an error of 1.4 % for the uncertainty of the trigger bias.

6.4 Background Parameterization

To estimate the systematics due to the background parameterization we varied the slope of the left and right side exponential by one sigma and studied

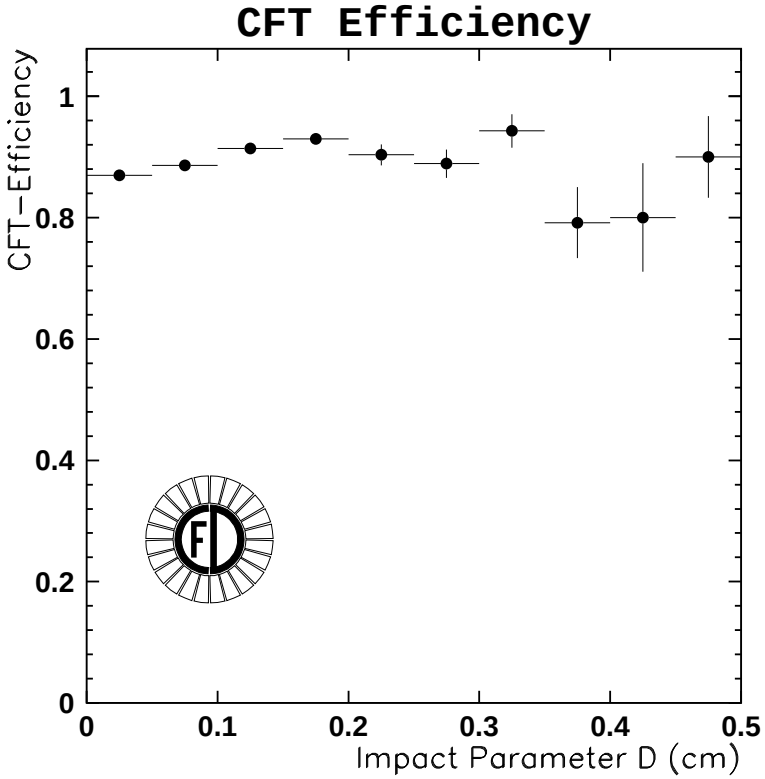

Figure 56: *CFT efficiency as a function of the impact parameter with respect to the fitted beam position.*

the effect on the lifetime. From this study the systematic error due to the background parameterization was estimated to be 0.5%.

6.5 Residual Misalignment

We also studied the effect of possible residual misalignments in the SVX. Here different methods have been used.

- We tried to evaluate the residual misalignment from the wedge-by-wedge average of the impact parameter distribution with respect to the fitted beam position as observed with W electrons. Then the lifetime analysis was repeated offsetting the impact parameter of each of the two μ's by the measured wedge dependent offset. The maximum variation observed on the lifetime value, with respect to the standard data sample is 2%.

- The analysis was repeated just using the alignment constants obtained from the optical survey (see [65]) prior to any alignment using tracks. In this case variations up to 5% were observed. But since a significant increase of the central gaussian part was also observed it was clear that this was an overestimate of the effect.

- Another method was to use the full detector simulation to estimate the effect. Here the detector was 'artificially' misaligned within the boundaries of our knowledge about the detector alignment. In this case the lifetime varied by about 1%.

Finally the systematic error due to misalignments was estimated to be 2%.

6.6 Stability of the Beam

As described in 3.4 the beam is very stable during a run. We assign a systematic error of 1% due to any beam instability.

6.7 Total systematic error

Table 14 now summarizes all known sources of systematic uncertainties.

Description	Contribution in %
Production and decay kinematic	3 %
Uncertainty in $c\tau$ resolution (unbinned Fit only)	1.6 %
Trigger bias	1.4 %
Background parameterization	0.5 %
Residual misalignment	2.0 %
Beam stability	1.0 %
Total systematic error for Binned L. FIT	4.0 %
Total systematic error for Unbinned L. FIT	4.3 %

Table 14: *Systematic errors.*

7 Final Result and Comparison with Other Experiments

In this chapter we present the final result and compare it to results from experiments at LEP. The LEP experiments dominate the world average at the moment. They have an considerable statistical advantage over earlier experiments at e^+e^- machines (see [28] and [29]). In addition three of the four LEP experiments (ALEPH, OPAL and DELPHI) used high precision silicon vertex detectors in their measurements like CDF.

We finally obtain the following result for the inclusive b-lifetime using the unbinned fit as the default (see also [66]):

$$\tau_B \;=\; 1.46 \;\pm\; 0.06\;(stat.) \;\pm\; 0.06\;(syst.)\;ps$$

This is in good agreement with recent LEP results (from [30],[67] and [27]) as can be seen in Figure 57 and Table 15. The first three measurements in Table 15 use the vertex of the J/ψ to extract the lifetime from the data. The rest of the measurements use a fit to the signed impact parameter distribution of leptons from b-decay to obtain the b-lifetime. A description of this method can be found in [31] and references therin.

However, we note that the LEP average does not need to coincide perfectly with our measurement since our b-lifetime is the average over all b-hadrons produced in $p\overline{p}$ - collisions at $\sqrt{s} = 1.8\;TeV$ weighted by the product of their branching ratio into J/ψ and their production cross section.

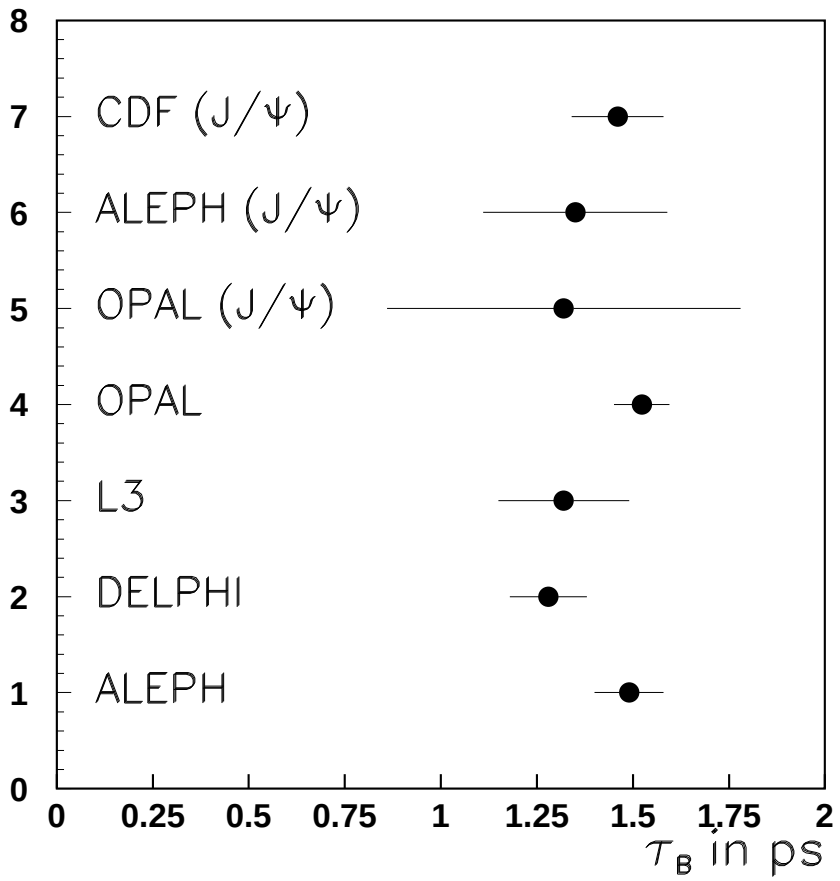

Figure 57: *Comparison of recent inclusive lifetime measurements.*

Experiment	τ_b in ps
CDF (J/ψ)	$1.46 \pm 0.06\,(stat.) \pm 0.06\,(syst.)$
ALEPH (J/ψ)	$1.35 \pm 0.19\,(stat.) \pm 0.05\,(syst.)$
OPAL (J/ψ)	$1.32\ {}^{+0.31}_{-0.25}\,(stat.) \pm 0.15\,(syst.)$
OPAL	$1.523 \pm 0.034\,(stat.) \pm 0.038\,(syst.)$
L3	$1.32 \pm 0.08\,(stat.) \pm 0.09\,(syst.)$
DELPHI	$1.28 \pm 0.1\,(stat. + syst.)$
ALEPH	$1.49 \pm 0.03\,(stat.) \pm 0.06\,(syst.)$

Table 15: *Comparison of recent inclusive lifetime measurements.*

8 Determination of the CKM Matrix Element $|V_{cb}|$

As described in section 1.7 knowing the lifetime and semileptonic branching ratio of b-hadrons allows to determine the element $|V_{cb}|$ of the CKM matrix using formula (14). Here we combine the semileptonic branching ratio as measured by the LEP experiments and the measurement of $|V_{ub}|/|V_{cb}|$ from ARGUS and CLEO with our lifetime measurement to get an estimate of V_{cb}. This assumes that the spectator model is valid and that the semileptonic width of b-hadrons produced in Z^0-decays is the same as for b-hadrons produced in $p\bar{p}$-collisions where the admixture of different b-hadrons can vary from that at LEP. Table 16 summarizes the various numerical values and their uncertainties which have been used in this estimate. Figure 58 shows the curve we obtain using formula 14 in the V_{cb} versus V_{ub} plane. The solid line corresponds the central values while the dashed lines show the one standard deviation errors. The systematic error due to theoretical uncertainties is very likely underestimated! The LEP experiments for example used an larger error on the b-quark mass to take theoretical uncertainties into account. They also used a different method to calculate the error by using the fact that the mass difference $m_b - m_c$ is well measured. The solid straight line corresponds to the ARGUS and CLEO measurement of $|V_{ub}|/|V_{cb}|$=0.15. The dashed straight lines correspond to the estimated error on this measurement. The two solid curves intersect at:

$$|V_{cb}| = 0.042 \pm 0.004$$

This is in good agreement with the LEP average of:

$$|V_{cb}| = 0.043 \pm 0.005 \text{ [33]}$$

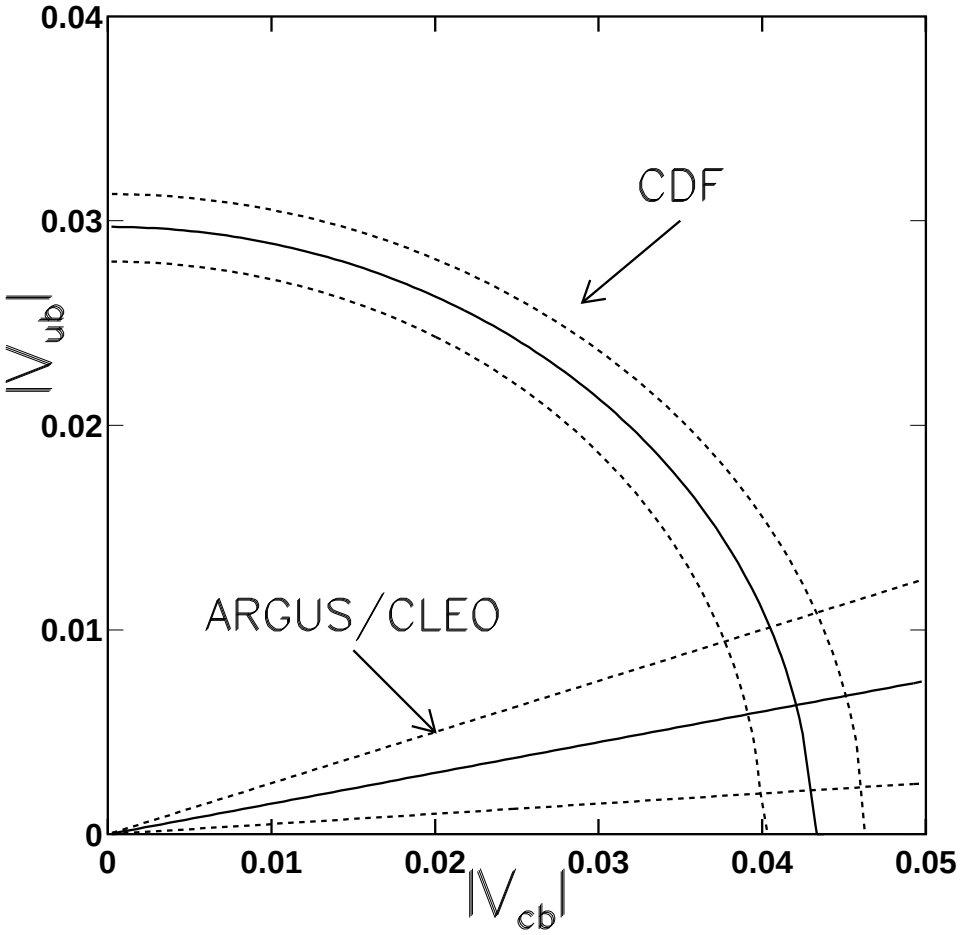

Figure 58: *Determination of* V_{cb}.

	Value	Reference
BR_{sl}	0.112 ± 0.006	[33]
τ_b	$1.46 \pm 0.085 ps$	this measurement
m_u	$0.2 \pm 0.2\ GeV/c^2$	
m_c	$1.65 \pm 0.08\ GeV/c^2$	
m_b	$4.95 \pm 0.07\ GeV/c^2$	[38]
$\alpha_s(m_b^2)$	0.20 ± 0.03	[33]
$\|V_{ub}\|/\|Vcb\|$	0.15 ± 0.1	[37]

Table 16: *Numerical values used to determine V_{cb}.*

List of Figures

List of Tables

References

[1] C.N. Yang and R.L. Mills, Phys. Rev. 96 (1954) 191;
M. Gell-Mann, *Acta Physica Austriaca, Suppl.* IX (1072) 733;
H. Fritzsch and M. Gell-Mann, XVI International Conference High Energy Physics, Batavia, Vol. II p.135 (1972);
H. Fritzsch, M. Gell-Mann and H. Leutwyler, Phys. Lett. B 47 (1973) 365.

[2] S.L. Glashow, Nucl. Phys. 22 (1961) 579;
S. Weinberg, Phys. Rev. Lett. 19 (1967) 1264;
A. Salam, "Elementary Particle Theory", Proc. 8th Nobel Symposium Aspenäsgården, publ. Almquist and Wiksell, Stockholm, (1968) 367.

[3] Particle Data Group

Phys. Rev. D Vol. 45 (1992)

[4] M. Kobayashi and K. Maskawa, Progr. Theor. Phys. 49 (1973) 652.

[5] N. Cabibbo

; Phys. Rev. Lett. 10 (1963) page 531

[6] L. Wolfenstein, Phys.Rev. Lett. 51 1945, (1983).

[7] A. Ali, DESY 92-152, to be published in Proceedings of XXVIth International Conference on High Energy Physics, Dallas.

[8] J. L. Rosner

The Cabibbo-Kobbayashi-Maskawa Matrix ; in *B Decays*, World Scientific 1992 page 312

[9] CDF Collaboration, F. Abe et al. ; Phys. Rev. Lett. 69 (1992) page 3704

[10] Glover, Martin, Stirling

J/ψ *Production at large transverse momentum at hadron colliders* ; Z. Physik 38C (1988) page 473

Glover, Halzen, Martin

Physics from J/ψ*- Tags in* $p\overline{p}$ *Collisions* ; Phys. Lett. B (1987), VOL. 185 NR. 3,4 page 441

[11] CDF Collaboration, F. Abe et al.

Observation of the Decay $B_s^0 \to \mathrm{J}/\psi\phi$ *in* $p\bar{p}$ *Collisions at* $\sqrt{s}$ *= 1.8 TeV* ; FERMILAB-PUB-93/141-E submitted to Phys. Rev. Lett. June 2, 1993.

[12] CDF Collaboration, F. Abe et al. ;FERMILAB-PUB-93/091-E submitted to Phys. Rev. Lett.

[13] CDF Collaboration, F. Abe et al. ;FERMILAB-PUB-93/106-E submitted to Phys. Rev. Lett.

[14] CDF Collaboration, F. Abe et al. ; Phys. Rev. Lett. 68 (1992) page 3403

[15] CDF Collaboration, F. Abe et al. ;FERMILAB-PUB-93/145-E submitted to Phys. Rev. Lett.

[16] P. Nason, S. Dawson, R.K. Ellis

The One Particle Inclusive Differential Cross Section for Heavy Quark Production in Hadronic Collisions ; Nuclear Physics B327 (1989) page 49-92

[17] M. L. Mangano et al. ; Nuclear Physics B373 (1992) page 295

[18] A. Martin, R. Roberts and J. Stirling

New Information on the Parton Distributions ; RAL-92-021, DTP/92/16 (1992)

[19] M. L. Mangano

On the B and J/ψ *Cross section Measurements at UA1 and CDF* ; IFUP-TH 2/93 (1993) ; CDF internal note 1970 (1993)

[20] E. L. Berger et al. ; Argonne preprint, ANL-HEP-CP-92-79

[21] C. Peterson et al., Phys. Rev. D 27 (1983) 105.

[22] J. Chrin, Z. Phys. C 36 (1987) 163.

[23] R. Rückl, Habilitationsschrift, Universität München, 1984

[24] H. Schröder

Physics of the B Mesons ; DESY 88-101 (1988)

[25] H. Fritzsch

How to Discover the B Mesons ; Physics Letters 86B (1979) page 343-346

[26] ARGUS Collaboration, H. Albrecht et al.

; Phys. Rev. Lett. 162B (1985) page 395

ARGUS Collaboration, H. Albrecht et al.

; Phys. Rev. Lett. 199B (1987) page 451

CLEO Collaboration, M. S. Alam et al. ; Phys. Rev. D 34 (1986) page 3279

[27] Aleph Collaboration

Measurements of Mean Lifetime and Branching Fractions of b Hadrons decaying to J/ψ ; Physics Letters B 295 (1992) page 396-408

[28] MARK-II Collaboration, A. Lockyer et al., Phys. Rev. Lett 51 (1983) 1316;
MAC Collaboration, W. Ash et al., Phys. Rev Lett. 58 (1987) 640;
HRS Collaboration, J.M. Brown et al., Phys. Lett. B 195 (1987) 301;
DELCO Collaboration, D.E. Klem et al., Phys. Rev D 37 (1988) 41;
MARK-II Collaboration, R.A. Ong et al., Phys. Rev. Lett. 62 (1989) 1236.

[29] TASSO Collaboration, W. Decamp et al., Z. Phys. C 44 (1989) 1;
JADE Collaboration, J. Hagemann et al., Z. Phys. C 48 (1990) 401.

[30] DELPHI Collaboration, P. Abreu et al., Z. Phys. C 53 (1992) 567;
L3 Collaboration, B. Adeva et. al. Phys. Lett B 270 (1992) 111;
OPAL Collaboration, P.D. Acton et al., Phys. Lett. B 274 (1992) 513;
ALEPH Collaboration, D. Buskulic et al., Phys. Lett. B. 295 (1992) 174.
OPAL Collaboration, P.D. Acton et al., CERN PPE/93-92
submitted to Zeitschrift für Physik C

[31] W.B. Atwood and J. A. Jaros

B Lifetimes ; in *B Decays*, World Scientific 1992 page 261

[32] H. Wenzel for the CDF Collaboration

b-Lifetime Measurements at CDF ; FERMILAB-CONF-93/159-E, to be published in the Proceedings of the XXVIIIth Recontres de Moriond, QCD and high energy session, Les Arcs,Savoie, France March 20-24, 1993

[33] Samuel C.C. Ting

New Results from LEP Experiments ; Proceedings of The Fermilab Meeting DPF 92, Nov. 10-14 1992 page 53

[34] CLEO Collaboration, R. Fulton et al. ; Physics Rev. D43 (1991) page 651
ARGUS Collaboration, H. Albrecht et al. ; Physics Letters B 232 (1989) page 554

[35] O. Schneider

Private communication and talk presented at the Int. Symp. on Heavy Flavour Physics (Montreal, Canada) 6-10, July 1993

[36] Sheldon Stone

Semileptonic B Decays - Experimental ; in *B Decays*, World Scientific 1992 page 210

[37] CLEO Collaboration ; Phys. Rev. Lett. 56 (1986) page 800

ARGUS Collaboration, H. Albrecht et al. ; Physics Letters B 255 (1991) page 297

David G. Cassel

b Physics ; Proceedings of The Fermilab Meeting DPF 92, Nov. 10-14 1992 page 213

[38] ARGUS Collaboration, H. Albrecht et al., Phys. Lett. B249(1990) page 359
CLEO Collaboration, Proc. 1985 Int. Sym. on Lepton and Photon Interactions at High Energies (KYOTO 1986). page 406

[39] C. S. Kim and A. D. Martin

; Physics Letters B Vol. 225 (1989) page 186

[40] G. Altarelli et al., Nucl. Phys. B208(1982) 365

[41] CDF Collaboration, F. Abe et al.,

The CDF Detector: An Overview ; NIM A271 (1988) page 387-403

[42] F. Bedeschi et al. *Design and Construction of the CDF Central Tracking Chamber* ; NIM A268 (1988) page 50-74

[43] G. Foster, J. Freeman, C. Newman-Holmes and J. Patrick

The Fast Hardware Track-Finder for the CDF Central Tracking Chamber ; NIM A269 (1988) page 93-100

[44] G.Ascoli et al.

CDF Central Muon Detector ; NIM A268 (1988) page 33-44

[45] D. Amidei et al.

A Two Level Fastbus Based Trigger System for CDF ; NIM A269 (1988) page 51-62

[46] G. Ascoli et al.

CDF Central Muon Level-1 Electronics ; NIM A269 (1988) page 63-67

[47] D. Amidei et al.,

The CDF SVX: A Silicon Vertex Detector for a Hadron Collider ;NIM A289 (1990) page 388-399

[48] P.B. Billoir et al.

Track Element Merging Strategy and Vertex Fitting in Complex Modular Detectors

; NIM A241 (1985), page 115-131

P. Billoir

Track Recognition Coupled to Geometrical Fit ; DELPHI internal note 84-18 Prog 5 (1984)

[49] F. Bedeschi

An Inexpensive Method For Global Track Fitting and Track Segment Matching ; CDF internal note 371 (1985)

H. Wenzel

Tracking in the SVX ; CDF internal note 1790 (1992)

[50] Andreas Hölscher

Exklusive hadronische Zerfälle von B-Mesonen ; DESY F15-90-06 October 1990

[51] CLEO Collaboration

; Phys. Rev. Lett. 56 (1986) page 800

W. Chen, Ph.D. thesis Purdue University, May 1990.

[52] H. Schröder

New Results on Beauty Physics from ARGUS ; Les Rencontres de Physique de la Val. d'Aoste March 3-9, 1991

R. Mundt (ARGUS) private communication

Steven Ball

Hadronic B Meson Decay Testing Factorization and HQET ; Proceedings of The Fermilab Meeting DPF 92, Nov. 10-14 1992 page 533

[53] Fritz DeJongh and Randal Hans

Level 1 and Level 2 Low P_t Central Muon Trigger Efficiencies for Run 1A ; CDF internal note 1999 (1993)

[54] Hans Wenzel

Fitting the beam position with the SVX ; CDF internal note 1924 (1993)

[55] D. Amidei et al.

Measurement of the τ-lifetime Physical Review D, Vol. 37 (1988) page 1750

[56] L. Gladney et al.

Measurement of the D^0 and D^+ lifetimes ; Physical Review D, Vol. 34, Nr. 9 (1986)

[57] CERN Program Library

CERN Program Library short write up ; CERN (1989)

[58] M.G. Kendall and A. Stuart

The Advanced Theory of Statistics ; Charles Griffin, London, 1977 - 1979

[59] S. Brandt

Datenanalyse ; BI Wissenschaftsverlag, ISBN3-411-01591-8

[60] W.T. Eadie, D. Drijard, F.E.James, M. Roos, B. Sadoulet

Statistical Methods in Experimental Physics ; NORTH-HOLLAND PUBLISHING COMPANY

[61] CERN Application Software Group

MINUIT Function Minimization and Error Analysis, ; CERN, D506 (1992)

[62] CERN Application Software Group

PAW Physics Analysis Workstation ; CERN, Q121 (1992)

[63] F. Bedeschi et al.

Evaluation of the resolution of CTC and SVX ; CDF internal note 1939 (1993)

[64] Carol E. Anway-Wiese

Offline Muon Matching Cuts ; CDF internal note 1986 (1993)

[65] F. Bedeschi, L. Galtieri, N. Produit, O. Schneider, M. Shapiro, J. Skarha, R. Snider, H. Wenzel, W. Yao

Status report on SVX Alignment ; CDF internal note 1948 (1993)

[66] CDF Collaboration, F. Abe et al.

Measurement of the Average Lifetime of B-hadrons produced in $p\bar{p}$ Collisions at $\sqrt{s}$ = 1.8 TeV ; FERMILAB-PUB-93/158-E submitted to Phys. Rev. Lett. June 22, 1993.

[67] OPAL Collaboration, G. Alexander et al. ; Physics Letters B 266 (1991) page 485

Curriculum [redacted]

Hans-Joachim Wenzel

[redacted] [redacted]

Schulischer Werdegang:	
1968 - 1972	Grundschule in Oberhausen
1972 - 1979	Karl Broermann Realschule Abschluss: mittlere Reife
1979 - 1982	Freiherr v. Stein Gymnasium Abschluss: Abitur
1.7.1982 - 30.9.1983	Grundwehrdienst
Studium:	
Oktober 1983	Beginn des Physik Studiums an der RWTH Aachen Schwerpunkt: Elementarteilchenphysik Nebenfach: Lasertechnik
Juni 1989	Beendigung der Diplomarbeit: "Testergebnisse zur Ortsmessung und Teilchenidentifikation der radialen Driftkammern für den H1-Detektor."
November 1989	Abschluss: Diplomphysiker
Feb. 1990 - Sommer 1993	Doktorarbeit: "Measurement of the Inclusive B-Lifetime Using J/ψ's at the CDF–Experiment."
Feb. 1990 - Juni 1991	Arbeit in der CDF SVX Gruppe in Pisa/Fermilab (Prof. Bellettini)
Juli 1991 - November 1993	Fermilab Gastwissenschafter
Dezember 1993	Post Doctoral Fellow: Lawrence Berkeley Laboratory